University of Kentucky
UKnowledge

University of Kentucky Master's Theses | Graduate School

2003

STUDY OF THE "POOR MAN'S NAVIER-STOKES" EQUATION TURBULENCE MODEL

Stewart Andrew Bible
University of Kentucky, sabible@hotmail.com

Right click to open a feedback form in a new tab to let us know how this document benefits you.

Recommended Citation

Bible, Stewart Andrew, "STUDY OF THE "POOR MAN'S NAVIER-STOKES" EQUATION TURBULENCE MODEL" (2003). *University of Kentucky Master's Theses*. 310.
https://uknowledge.uky.edu/gradschool_theses/310

This Thesis is brought to you for free and open access by the Graduate School at UKnowledge. It has been accepted for inclusion in University of Kentucky Master's Theses by an authorized administrator of UKnowledge. For more information, please contact UKnowledge@lsv.uky.edu.

ABSTRACT OF THESIS

STUDY OF THE "POOR MAN'S NAVIER-STOKES" EQUATION TURBULENCE MODEL

The work presented here is part of an ongoing effort to develop a highly accurate and numerically efficient turbulence simulation technique. The paper consists of four main parts, *viz.*, the general discussion of the procedure known as Additive Turbulent Decomposition, the derivation of the "synthetic velocity" subgrid-scale model of the high wavenumber turbulent fluctuations necessary for its implementation, the numerical investigation of this model and *a priori* tests of said model's physical validity. Through these investigations we have demonstrated that this procedure, coupled with the use of the "Poor Man's Navier-Stokes" equation subgrid-scale model, has the potential to be a faster, more accurate replacement of currently popular turbulence simulation techniques since:
1. The procedure is consistent with the direct solution of the Navier-Stokes equations if the subgrid-scale model is valid, *i.e.*, the equations to be solved are never filtered, only solutions.
2. Model parameter values are "set" by their relationships to N.–S. physics found from their derivation from the N.–S. equation and can be calculated "on the fly" with the use of a local high-pass filtering of grid-scale results.
3. Preliminary studies of the PMNS equation model herein have shown it to be a computationally inexpensive and *a priori* valid model in its ability to reproduce high wavenumber fluctuations seen in an experimental turbulent flow.

KEYWORDS: Fluid Dynamics, Turbulence, Additive Turbulent Decomposition, Poor Man's Navier-Stokes Equation, Large Eddy Simulation, Discrete Dynamical Systems

MULTIMEDIA ENHANCEMENTS USED: AVI (.avi)

Stewart Andrew Bible
July 30, 2003

Copyright©Stewart A. Bible 2003

STUDY OF THE "POOR MAN'S NAVIER-STOKES" EQUATION TURBULENCE MODEL

By

Stewart Andrew Bible

James McDonough
Director of Thesis

George Huang
Director of Graduate Studies

July 30, 2003

RULES FOR THE USE OF THESES

Unpublished theses submitted for the Master's degree and deposited in the University of Kentucky Library are as a rule open for inspection, but are to be used only with due regard to the rights of the authors. Bibliographical references may be noted, but quotations or summaries of parts may be published only with the permission of the author, and with the usual scholarly acknowledgements.

Extensive copying or publication of the thesis in whole or in part also requires the consent of the Dean of the Graduate School of the University of Kentucky.

THESIS

Stewart Andrew Bible

The Graduate School

University of Kentucky

2003

STUDY OF THE "POOR MAN'S NAVIER STOKES" EQUATION TURBULENCE MODEL

THESIS

A thesis submitted in partial fulfillment of the requirements for the degree of Master of Science in the College of Engineering at the University of Kentucky

By

Stewart Andrew Bible

Lexington, Kentucky

Director: Dr. J. M. McDonough, Professor of Mechanical Engineering

Lexington, Kentucky

2003

TABLE OF CONTENTS

LIST OF FIGURES

LIST OF FILES

Thesis.pdf (40.38 Mb)
2dic1.avi (1.3 Mb)
2dic2.avi (1.3 Mb)
2dic3.avi (1.2 Mb)
2dbvsb.avi (0.7 Mb)
2dgvsg.avi (0.6 Mb)
2dgvsg2a.avi (2.0 Mb)
2dgvsg2b.avi (1.8 Mb)
3dgvsg.avi (3.4 Mb)
3dbvsbvsb1.avi (3.3 Mb)
3dbvsbvsb2.avi (5.3 Mb)
3dbvsbvsb3.avi (3.4 Mb)
3dall1.avi (1.2 Mb)
3dall2.avi (2.2 Mb)

I. INTRODUCTION

This thesis is mainly concerned with the phenomenon of *turbulence* commonly encountered in the study of *fluid dynamics*. The following is a short synopsis of the contents of this paper along with a brief overview of fluid dynamics and turbulence.

1.1 BRIEF SYNOPSIS OF THE THESIS

For a strong understanding of the arguments and points of interest of the present paper it is necessary for the reader to be familiar with a variety of subtopics, and throughout we provide the necessary references for one exploring the rigorous study of turbulence. In addition, though, we think that the present paper should be approachable for all readers with a scientific background. As such in Chapter II we present concise overviews of some previous work on turbulence along with the current state-of-the-art in turbulence research (limited to what we believe enhances the presentation of our research). Included will be discussions on numerical procedures in turbulence, including RANS, DNS and LES, on the application of nonlinear dynamical systems theory to turbulence, on the so-called "synthetic velocity" subgrid-scale models for turbulence simulations and on the Additive Turbulent Decomposition procedure for which the "Poor-Man's Navier–Stokes" (PMNS) equation was first proposed.

Once a solid framework for the study is laid we proceed with presenting specific discussions of the SGS model investigated here, that of the PMNS equation. We begin, in Chapter III, with a detailed derivation of the 3-D PMNS equation from the 3-D incompressible N.–S. equation. Special attention is paid to this derivation with respect to what Navier-Stokes physics might be retained by the PMNS equation and the discussion focuses on generic relations between PMNS parameters and the true physical variables. To familiarize the reader with the general behaviors common among nonlinear systems such as the discrete dynamical system (DDS) studied here, and the methods which we have implemented in its study, Chapter IV is dedicated to the study of the analogous 2-D PMNS equations. Included are findings concerning the effects of the four bifurcation parameters and two initial conditions on the asymptotic behavior of the solutions as determined by implementation of tools such as

bifurcation diagrams, time series, power spectra, phase-portraits, regime maps, and basins of attraction diagrams, among others. Where appropriate the effects of the variations of these parameters are interpreted and discussed in the context of real fluid flow physics, given the previously mentioned derived relations between physics and PMNS parameters. In Chapter V we move on to the study of the more relevant 3-D PMNS equation. Again we use numerical procedures and the tools previously mentioned to investigate the behavior of the solutions of these equations and elucidate the complicated behaviors seen with meaningful discussions.

Finally in Chapter VI we present results from a sort of *a priori* test in the form of a qualitative curve fitting of PMNS equation time series (and thus bifurcation parameter values) to that of experimentally measured turbulence. This has required the definition of new quantitative parameters useful in characterizing the similarity of erratic time series and the use of a genetic algorithm to efficiently find the optimal model coefficient values needed to minimize a least-squares functional involving these characterization parameters. We conclude in Chapter VII with a summary of our findings and conclusions concerning the outcomes of the various studies presented.

1.2 INTRODUCTION TO FLUID DYNAMICS

As defined by Wilcox [1] a fluid is "a substance that cannot be in static equilibrium under the action of oblique stresses." This attribute leads to a so-called fluid flow, where fluid parcels undergo rotations, distortions, and displacements. Relating the *kinematic* variables associated with such motions to one another [1] one encounters what is known as the *strain-rate tensor* (see Aris [2] for an introduction to tensor mathematics);

$$[\boldsymbol{S}] = \begin{bmatrix} \frac{\partial u}{\partial x} & \frac{1}{2}\left(\frac{\partial v}{\partial x} + \frac{\partial u}{\partial y}\right) & \frac{1}{2}\left(\frac{\partial w}{\partial x} + \frac{\partial u}{\partial z}\right) \\ \frac{1}{2}\left(\frac{\partial u}{\partial y} + \frac{\partial v}{\partial x}\right) & \frac{\partial v}{\partial y} & \frac{1}{2}\left(\frac{\partial w}{\partial y} + \frac{\partial v}{\partial z}\right) \\ \frac{1}{2}\left(\frac{\partial u}{\partial z} + \frac{\partial w}{\partial x}\right) & \frac{1}{2}\left(\frac{\partial v}{\partial z} + \frac{\partial w}{\partial y}\right) & \frac{\partial w}{\partial z} \end{bmatrix}, \tag{1}$$

where (u, v, w) are components of the velocity vector $\boldsymbol{u}$ associated with an individual parcel. The ability of a fluid to resist any oblique stresses applied to it is given in terms of a frictional, or *viscous* force, and is due to intermolecular collisions. The resulting *stress tensor* was first

related to other dynamic variables through the law of conservation of momentum by L. Navier and the resulting equation is, therefore, known as Navier's equation:

$$\rho\frac{d\boldsymbol{u}}{dt} = -\nabla\boldsymbol{p} + \rho\boldsymbol{f} + \nabla\cdot[\boldsymbol{\tau}]. \tag{2}$$

Here $\boldsymbol{p}$ is the pressure force (the force everywhere normal to the fluid surface due to the collisions of molecules), $\boldsymbol{f}$ is an external force and $\boldsymbol{\tau}$ is the stress tensor due to friction. Later G. Stokes postulated three basic premises upon which the stress tensor can be related to the strain rate and fluid properties as

$$[\boldsymbol{\tau}] = 2\mu[\boldsymbol{S}] + \zeta\nabla\cdot\boldsymbol{u}[\boldsymbol{\delta}], \tag{3}$$

where μ is the molecular viscosity of the fluid and ζ the second viscosity (for further details concerning Stokes' postulate consult the text by Panton [3]). These two equations are considered the fundamental equations of fluid dynamics and, combined, are known as the *Navier-Stokes* (N.–S.) equation(s):

$$\rho\frac{d\boldsymbol{u}}{dt} = -\nabla\boldsymbol{p} + \rho\boldsymbol{f} + \nabla\cdot(2\mu[\boldsymbol{S}] + \zeta\nabla\cdot\boldsymbol{u}[\boldsymbol{\delta}]). \tag{4}$$

We note though that the N.–S. equation alone does not conserve mass so we must require additionally that the *continuity* equation,

$$\frac{\partial\rho}{\partial t} + \nabla\cdot(\rho\boldsymbol{u}) = 0, \tag{5}$$

be satisfied.

Furthermore, it is most often convenient to simplify the N.–S. equation by assuming incompressibility (infinite propagation of pressure) of the fluid; $\nabla\cdot\boldsymbol{u} = 0$, and so we arrive at the incompressible N.–S. equation:

$$\rho\frac{d\boldsymbol{u}}{dt} = -\nabla\boldsymbol{p} + \rho\boldsymbol{f} + \mu\nabla^2\boldsymbol{u}. \tag{6}$$

We should note that herein we will only be concerned with the case in which viscosity is

constant, $\mu = C$.

In component form the N.–S. equations are

$$\rho\left(\frac{\partial u}{\partial t} + u\frac{\partial u}{\partial x} + v\frac{\partial u}{\partial y} + w\frac{\partial u}{\partial z}\right) = -\frac{\partial p}{\partial x} + \rho f_x + \mu\left(\frac{\partial^2 u}{\partial x^2} + \frac{\partial^2 u}{\partial y^2} + \frac{\partial^2 u}{\partial z^2}\right) \tag{7}$$

$$\rho\left(\frac{\partial v}{\partial t} + u\frac{\partial v}{\partial x} + v\frac{\partial v}{\partial y} + w\frac{\partial v}{\partial z}\right) = -\frac{\partial p}{\partial y} + \rho f_y + \mu\left(\frac{\partial^2 v}{\partial x^2} + \frac{\partial^2 v}{\partial y^2} + \frac{\partial^2 v}{\partial z^2}\right) \tag{8}$$

$$\rho\left(\frac{\partial w}{\partial t} + u\frac{\partial w}{\partial x} + v\frac{\partial w}{\partial y} + w\frac{\partial w}{\partial z}\right) = -\frac{\partial p}{\partial z} + \rho f_z + \mu\left(\frac{\partial^2 w}{\partial x^2} + \frac{\partial^2 w}{\partial y^2} + \frac{\partial^2 w}{\partial z^2}\right) \tag{9}$$

Given any flow configuration with unchanging geometry there is a nondimensional parameter that determines the qualitative behavior of the fluid motion. This parameter, the Reynolds number, is given by

$$Re_L = \frac{\rho\, UL}{\mu}. \tag{10}$$

The Reynolds number provides a measure of the effects of the kinematic viscosity (μ/ρ), flow speed (U), and characteristic length (L) of a flow. Many variations of the Reynolds number (e.g. Taylor micro-scale, integral-scale) can be used with appropriate definitions of the length, time and velocity scales. From the N.–S. equation we can discern that physically the Reynolds number provides an indication of the ratio of the effects due to nonlinear interactions ($d\boldsymbol{u}/dt$) to those due to diffusion ($\nabla^2\boldsymbol{u}$). As the value of the Reynolds number increases flows typically progress from a steady state to a time-dependent one (possibly a periodic flow as is seen in the famous Karman vortex street seen for flow past a cylinder at moderate Reynolds number). Eventually, with further increase in the Reynolds number, the flow becomes erratic and this state of motion is commonly referred to as turbulence.

1.3 INTRODUCTION TO TURBULENCE

For those individuals who have not been initiated into the field of turbulence study, it is most often the case that this spectacularly complex phenomenon goes largely unnoticed, despite frequent encounters in our daily lives (the most well referenced being flow from a faucet). Turbulent fluid motion, though, did not escape the oberservation of Leonardo da

Vinci (1452-1519) whose sketches (see, *e.g.*, Richter [4]) of *chaotic* whirlpools (Figure 1) are believed by most to be the first attempt at describing turbulence.

Figure 1: Whirlpool sketch by Renaissance engineer Leonardo da Vinci [4].

In fact, da Vinci, as noted by Frisch [5], used the phrase "la turbolenza" to describe this tumultuous state of motion. This description could be based on the Latin root words, *turba*, meaning disturbance, or *turbo*, meaning a whirl. On the otherhand, Rouse and Ince [6] have attributed Lord Kelvin (1824-1907) for the popularization of the term 'turbulence' in describing the state of flow that is the focus of this paper. Despite such famous beginnings turbulence remains elusively difficult to concisely define and for an anecdotal review of the many attempts at such a definition one can see the excellent book by Tsinober [7]. Common "definitions" most often include the well accepted attributes of turbulence: Turbulent flows have a very large number of degrees of freedom, they are highly rotational and, most likely, three dimensional, they display enhanced levels of diffusivity, mixing, and dissipation, *etc.*. Above all, turbulence should be considered a continuum process as the smallest scales of turbulence are orders of magnitude greater than molecular length scales, *viz.*, the mean free path (see, *e.g.*, [3]).

After da Vinci's early description of turbulence such famous scientists as Leonard Euler (1707-1783), Hermann von Helmholtz (1821-1894), Lord Kelvin, Lord Rayleigh (1842-1919) and Joseph Boussinesq (1842-1929) [8] studied the problem. As noted by Lumley [9] the groundbreaking studies of and Osborne Reynolds (1842-1912) [10] began what has been called the modern study of turbulence. One can only say that nominal progress has been

made in the past 100 years in formulating a comprehensive 'theory of turbulence'. Much of the work in the 20^{th} century can be divided into two broad encompassing categories (as described by Libby [11]), *viz.*, semi-empirical studies aimed at providing information of direct engineering interest, *e.g.* pressure gradients, lift/drag coefficients, etc., and the study of universal/statistical theories of idealized turbulence. Some of the major contributions in these areas have come from von Karman [12], Taylor [13], Kolmogorov [14, 15, 16], Obukhov [17], Prandtl [18], Kraichnan [20, 21], Landau and Lifschitz [19], Batchelor [22], Saffman [23], Monin and Yaglom [24], Tennekes and Lumley [25], and Ruelle and Takens [26] among many others too numerous to cite. Here we will only be addressing the latter with no effort spent on semi-empirical issues.

In addition, due to advances in computer power over the last 50 years another branch of the study of turbulence has arisen; that of computer simulations of turbulence. To date it is most appropriate to list such simulations as a method to study the universal behavior of idealized turbulence, and often serves as a complement to experimental studies, as opposed to a semi-empirical tool.

II. PREVIOUS WORK

Throughout the 20^{th} century many scientists have been drawn to the field of turbulence research and have approached the problem from many different angles with varying degrees of success. Here we will briefly present some of the most effective/popular of these approaches including methods used in the numerical simulation of turbulence. Even today many interesting approaches and ideas concerning turbulence are being formulated and a few of the most recent and promising of these will also be discussed.

2.1 TURBULENCE

As we have mentioned previously it remains that relatively little is known quantitatively (and some might argue qualitatively) about the universality of turbulence. The most notable exception to this is the *two-thirds* (or minus five-thirds) *law* of Kolmogorov-Obukhov which has shown to hold true in many experimental investigations. Working under the assumption of homogeneous (composed of similar parts; uniform [27]), isotropic (having properties that are the same regardless of the direction of measurement [28]) turbulence at high Reynolds numbers with finite mean dissipation rate per unit mass, it was found [14, 15, 16] that in an *inertial subrange*, *i.e.*, a range of wavenumbers where results are independent of viscosity (scales sufficiently below the energy input scale and above the scale where viscosity dominates), the second-order structure function should be proportional to the product of the dissipation and length scale raised to some power, *viz.*,

$$\mathbb{S}_n(\ell) = \langle (\Delta \boldsymbol{u}(\boldsymbol{\ell}))^2 \rangle = (\varepsilon \ell)^{n/3}. \tag{11}$$

Here $\Delta \boldsymbol{u}$ is the velocity difference at points separated by distance ℓ and ε is the mean dissipation rate per unit mass. When $n = 2$ we have the classical Kolmogorov scaling and it follows that the energy spectrum (distribution of energy in Fourier space) scales as the wavenumber to the $-5/3$ power [17],

$$E(k) = C_k \varepsilon^{2/3} k^{-5/3}, \tag{12}$$

where k is the wavenumber corresponding to $1/\ell$, and C_k is a supposed universal constant. These relations can also be arrived at using less rigorous (than Kolmogorov-Obukhov's statistical derivation) dimensional arguments (see, *e.g.*, [19]). It is important to keep in mind that these "laws" are a direct consequence of the assumptions of homogeneity, isotropy, and scale invariance (all wavenumbers act invariably with respect to the energy transfer) within the inertial range. In turn these assumptions can be attributed to the return of all spatial and temporal symmetries as the Reynolds number is increased along with the idea, first proposed in the famous poem by Richardson [29], that large scales pass energy onto smaller scales which in turn pass the energy to smaller scales until it is dissipated by viscosity. Though, as Tsinober accutely notes [7], this energy transfer takes place in spectral space, not physical space as the poem would suggest. It is also of interest to note, as Frisch has [5], that *chaotic dynamical systems*, which we discuss in later sections, have similarly been shown to have symmetry increasing bifurcations as parameter values are increased. Furthermore it should be pointed out that the assumption of scale invariance has been shown to be incorrect for turbulence with a high degree of intermittency, i.e. flows that exhibit large times/spaces that exhibit well ordered flow fields interrupted by times/spaces for which the flow fields are chaotic (turbulent bursts/spots), a result which inspired Kolmogorov and Obukhov to make further revisions of their already well-accepted theory [30, 31].

2.2 NUMERICAL PROCEDURES IN TURBULENCE

The last quarter of the 20^{th} century saw not only the birth of the personal computer but also major advances in computer size and speed which were necessary to enable scientists to solve complex mathematical problems numerically. Numerical methods that were formulated years earlier by pioneering numerical analysts could now be implemented to solve ordinary and partial differential equations in a matter of minutes or hours. Turbulence, though, refused to yield to the efforts of numerical analysts due to its significant complexity. Researchers then turned to the most well-known and earliest numerical (in a sense) treatment of the N.–S. equations, that of the Reynolds' averaging procedure, resulting in the Reynolds' Averaged Navier-Stokes (RANS) equations. In time, computer resources grew to such an extent as to allow for the solving of the full N.–S. equation, though at Reynolds numbers that are only a

small fraction of those seen in real world applications. This type of procedure has come to be known as Direct Numerical Simulation (DNS). As the limitations of both methods have been realized, by most, to be impassable, efforts have turned to a compromise between the two methods known as Large-Eddy Simulation (LES). In the following three sections we will breifly discuss these methods in turn.

2.2.1 Reynolds' Averaged Navier–Stokes Equation

Traditionally it has been thought that turbulence fluctuations can only be described, and thus modeled, in a statistical fashion. The first attempt to present such an idea formally is due to O. Reynolds [10] and is known as the Reynolds' averaging procedure. The main idea of Reynolds' averaging is to split the temporally varying vector field solution to the N.–S. equation into two parts, one steady and one fluctuating. This is accomplished by taking the integral in time of the full velocity field

$$\overline{\boldsymbol{u}(x,y,z)} = \lim_{T\to\infty} \frac{1}{T} \int_0^T \boldsymbol{u}(x,y,z,t)dt, \tag{13}$$

and allowing the fluctuating velocity to be

$$\boldsymbol{u}'(\boldsymbol{x},\, t) = \boldsymbol{u}(\boldsymbol{x},\, t) - \overline{\boldsymbol{u}(\boldsymbol{x})}.$$

We note, though, that Reynolds originally proposed averaging in space, a procedure more akin to LES than today's RANS procedures. We now write the N.–S. equation in a simplified form and take the average, as above, of this equation

$$\overline{\frac{\partial u_i}{\partial t}} + \overline{\frac{\partial (u_i u_j)}{\partial x_j}} = \overline{\frac{\partial p}{\partial x_i}} + \frac{1}{Re}\overline{\frac{\partial^2 u_i}{\partial x_j^2}}.$$

Utilizing the fact that time averaging commutes with differentiation we find

$$\frac{\partial \overline{u}_i \overline{u}_j}{\partial x_j} + \frac{\partial \overline{u_i' u_j'}}{\partial x_j} = -\frac{\partial \overline{p}}{\partial x_i} + \frac{1}{Re}\frac{\partial^2 \overline{u_i}}{\partial x_j^2}. \tag{14}$$

Most often the term, $\overline{u_i' u_j'}$, is called the Reynolds stress and must, necessarily, be modeled

in some fashion because of the unknown nature of the fluctuating velocities.

We will not go into detail on proposed models of the Reynolds stress but instead refer the reader to the monograph by Wilcox [32] in which there are listed four major categories of Reynolds stress models; algebraic models, one-equation models, two-equation models and second-order closure models. Some of the most popular models are the mixing length models of Prandtl [33] and Cebeci and Smith [34], the one-equation model of Spalart and Allmaras [35, 36], the $k - \varepsilon$ two-equation models (see, *e.g.*, Wilcox [37]) and the second-order closure model of Launder *et al.* [38].

The increasing complexity seen in the evolution of these models raises doubts concerning the feasibility of such a method. Indeed RANS has proven to be only marginally successful for some cases. Not surprisingly it has been shown by McDonough [39] that the erros associated with RANS equation closure models do not decrease with decreasing grid spacings. This is due to the fact that the RANS equation is not *consistent* with the N.–S. equation unless the exact values of the Reynolds stresses are used (which, of course, would require a DNS) and the associated error is $\mathcal{O}(1)$. The recent introduction of unsteady averaged equations (URANS) (see *e.g.*, [32]) has renewed interest in the study of such averaging procedures.

2.2.2 Direct Numerical Simulation

The solutions of the Navier-Stokes equations at moderately high Reynolds numbers are known to possess a large number of degrees of freedom and, in fact, the number of active degrees of freedom grows as $Re^{9/4}$ (see [19]). These active degrees of freedom translate to a large number of scales which are turbulently interacting. This leads to the major difficulty of DNS, *viz.*, the number of grid points needed to accurately resolve turbulence also grows exponentially ($N \propto \exp^{Re}$) with increasing Reynolds' number.

Early work in DNS was performed at the National Center for Atmospheric Research (*e.g.* Fox and Lilly [40]), and for a complete history of DNS see the excellent review by Moin and Mahesh [41]. Examples of the types of flows that have been studied using DNS include forced and decaying isotropic turbulence (see, *e.g.*, Siggia[42] and Huang and Leonard [43]), channel flow (*e.g.*, Kim *et al.* [44]), boundary layer flows (*e.g.*, Moin *et al.* [45]), backward facing step flow (*e.g.*, Le and Moin [46]), and compressible turbulence (*e.g.*, Lee *et al.* [47]

and Samtaney *et al.* [48]), among others. The Reynolds numbers of these simulations are all in the range $50 \sim 5000$, much less than Reynolds numbers of most flows in nature and industry, yet large enough to reproduce the inertial range and be a successful theoretical tool. For a review on these works and other references see the paper by Siggia [49].

2.2.3 Large-eddy Simulation

Despite the large amount of effort that has been put into formulating Reynolds stress models over the past few decades, overall success in reproducing flow physics using the RANS equations has been limited. These failures should be expected since it is easily seen that the RANS equations are only equivalent to the Navier-Stokes equations if $t \to \infty$, which can never be the case in computer simulations. Also DNS has its own limitations that were mentioned previously. These arguments are the motivation behind the recent development of large-eddy simulation methods. For extensive reviews of LES see, *e.g.*, Lesieur and Métais [50], Rogallo and Moin [51], or Lesieur [52].

LES is most often presented as propounded by Deardorf [53] and Leonard [54], both of whom used an averaging over grid cell volumes. More recently the LES filtering operator has been specifically defined (see, *e.g.*, Chollet and Lesieur [55]) as

$$\widetilde{f}(\boldsymbol{x}) = \int f(\boldsymbol{x}')G(\boldsymbol{x}, \boldsymbol{x}'; \Delta)d\boldsymbol{x}', \tag{15}$$

where G is the filter kernel that operates on the N.–S. equation. For some commonly used types of filters see the article by Piomelli [56]. Complications arise when filtering the N.–S. equation due to the fact that filtered fluctuations are not equal to zero, as are averaged fluctuations in the case of the RANS equations. The most common form of the LES equations is

$$\frac{\partial u_i}{\partial t} + \frac{\partial \widetilde{u}_i \widetilde{u}_j}{\partial x_j} = -\frac{\partial \widetilde{p}}{\partial x_i} + \frac{1}{Re}\frac{\partial^2 \widetilde{u}_i}{\partial x_j^2} + \mathcal{M}_i, \tag{16}$$

where

$$\mathcal{M}_i = -\frac{\partial \tau_{ij}}{\partial x_j} + \mathcal{C}_i,$$

$$\tau_{ij} = \widetilde{u_i u_j} - \widetilde{u}_i \widetilde{u}_j,$$

and $\mathcal{C}_i$ is a term due to the error of approximating the filtering operator as one that commutes with differentiation. The term τ_{ij} is referred to as the subgrid-scale stress (SGS), and most often an *eddy viscosity* model for this stress is formulated so that a mock drain of energy from the large scales will occur:

$$\tau_{ij} - \frac{\delta ij}{3}\tau_{kk} = -2\nu_T \mathcal{S}_{ij}.$$

The most well known of these models is the famous Smagorinsky [57] model

$$\nu_T = C\Delta^2 |\boldsymbol{S}| \mathcal{S}_{ij},$$

where $\mathcal{S}_{ij}$ is the strain-rate tensor. Due to the similarities between the modeled terms in LES and RANS formulations often there occurs model overlap, but the most popular LES models to date are the dynamic models first proposed by Germano *et al.* [58] and scale similarity models (see Meneveau and Katz [59]).

2.3 CURRENT TRENDS

One of the most important aims of science is that of prediction. Knowing the outcome of certain events in advance prepares one to respond appropriately. Still, science lacks even a precise division between what is predictable and deterministic and what is random and unpredictable. First we can consider a complex phenomena that is unpredictable due to the sheer size of the problem, *e.g.*, one that contains an intractably enormous range of active degrees of freedom, many interacting sytems, etc., but is (probably) deterministic. Short term weather prediction on global scales and simulating the interactions of individual molecules in a volume of gas fall into this category. Secondly we can classify some systems as truly random and stochastic. Excluding philosophical arguments we can conclude that much of human behavior falls into this category. One could even argue that trends in turbulence modeling, more often art than science, could be so classified. Obscuring the obvious separation of these two classes is the (re)discovery of Lorenz [60] of deterministic systems that are long term unpredictable due to the repelling nature of nearby trajectories.

That is, the finite precision associated with the measurement of the initial conditions of such a physical system imply that one can only state the probability that a trajectory will be at a certain point in phase space after some time, even though the equations corresponding to the system are completely deterministic. This has led to the description of a third class of unpredictable systems that have come to be known as *chaotic dynamical systems* and are characterized by *sensitivity to initial conditions* (SIC) as seen in the Lorenz equations [60].

Though in fact nonlinear dynamical systems were studied as early as the 19^{th} century by Poincaré [61], the (re)discovery of the dynamics associated with this class of equations was one of the most exciting mathematical findings of the 20^{th} century. For a complete review of the conceptual history of the study of nonlinear dynamical equations see the article by Aubin and Dalmedico [62]. This discovery was met with great anticipation by the scientific community and has led many researchers, rightfully so, to draw parallels between such mathematics and physical systems that were previously beyond description. Here we will give special attention to the relationship between turbulence and chaotic phenomena. Also, we need to consider the value that chaotic dynamics can have in prediction of turbulent flow fields. To this end we will discuss the growing field of turbulence models known as synthetic velocity models and a novel turbulence simulation technique proposed to utilize synthetic velocities known as Additive Turbulent Decomposition (ATD).

2.3.1 Chaos and Turbulence

If we consider that hydrodynamic turbulence as seen in nature is a solution to the N.–S. and continuity equations, as opposed to singularities of those equations as proposed by Leray [63], we can then apply the mathematical treatments of dynamical systems theory to the evolving velocity fields. The evolution equation can be generalized as

$$\frac{d\boldsymbol{x}(t)}{dt} = F(\boldsymbol{x}(t)),$$

where $\boldsymbol{x}(t)$ is some velocity field at time t and F is the forcing function due to the N.–S. and continuity equations. One can easily imagine a viscous fluid progressing through a collection of states, from steady state to progressively more complicated flow patterns, as the forcing

becomes larger due to the variation in some physical variable, *e.g.* pressure, heat flux, etc.. Originally, it was proposed by Landau and Lifschitz [19] that this progression to turbulence occurs through an infinite succession of *Hopf bifurcations* due to instabilities that cause the flow field to become a function of an additional, incommensurate frequency;

$$\boldsymbol{x}(t) = f(\omega_1 t, \omega_2 t, \omega_3 t, \ \ldots, \omega_n t),$$

where incommensurate means that the ratio of any of the frequencies (ω_is) cannot be expressed as a ratio of whole numbers. This type of behavior, known as quasiperiodicity and associated with flow on a torus, is fundamentally different than the dynamics seen by Lorenz since, as noted by Yorke and Yorke [64], any nearby trajectories will not separate but instead remain arbitrarily close to one another as time progresses.

As an alternative to this description Ruelle and Takens, expanding on the ideas of modern mathematicians, most notably S. Smale [65], concerning chaotic dynamics proposed that turbulence could be explained by the onset of a *strange attractor* (which will be defined in the sequel). This new progression from steady-state to turbulence was then called a *scenario*, and the original Ruelle-Takens-Newhouse (RTN) scenario was first described in 1971 [26, 66]. The RTN scenario borrows from the Landau proposition by considering Hopf bifurcations but additionally states that after successive Hopf bifurcations, beginning from a steady state, then it is *likely* that the sytem will possess an Axiom A strange attractor (see [65]), *i.e.*, any quasiperiodic trajectory more than two incommensurate frequencies needs only be perturbed (possibly carefully) by ϵ to become attracted to a strange attractor. In addition the modern mathematical theory of turbulence also incorporates the Feigenbaum (see, *e.g.*, [67, 68]) scenario through a series of *pitchfork* (period doubling) bifurcations and the Pomeau-Manneville scenario through intermittency [69]. The pioneering efforts of Gollub and Swinney [70] and Gollub and Benson [71] bridged the gap between theory and reality and demonstrated the RTN transition to turbulence by experiments in fluid convection. For further reading on dynamical systems see the texts by Alligood *et al.* [72] and Ruelle [73] and for more on "roads to turbulence" see the review articles by Eckmann [74] and Eckmann and Ruelle [75].

Progress in utilization of the above theories to turbulence has been slow. We are of the belief that this is due to the attempts by many to oversimplify turbulence by analogy with lower dimensional nonlinear systems that have been shown to be chaotic. Tsinober [7] makes this point in the following quotation: "Methods of dynamical systems theory, after an initial period of euphoria and even claims that the problem of turbulence was solved, have proved to be ineffective/irrelevant for the theory of fully developed turbulence....it is quite plausible that any fluid flow which is adequately represented by a low dimensional system is not turbulent – a kind of definition of 'non-turbulence'." This oversimplification is of the same general class as those that commonly occur in modeling of unknown terms in LES and RANS simulations, *viz.*, *ad hoc* theories/models deemed necessary due to the "incomprehensible" nature of fully developed turbulence. Therefore the lack of significant progress in the application of dynamical systems theory to turbulence might be expected and should not be a discouragement to those that are of the opinion that the full potential of chaotic dynamics has yet to be realized in the study of turbulence. Here we take the position of McDonough and coworkers (e.g. [76, 77]) that a subspace of fully developed turbulence, the so-called small-scales, may be effectively described by lower dimensional dynamical systems without belying the inherent complexity of fully developed turbulence.

2.3.2 Synthetic Velocity Models

Of course, all things being equal, we would prefer to simulate all scales of turbulence with only minimal costs (computational resources). Unfortunately, as we have previously mentioned, today's computers are not of sufficient size and speed to accomplish this task for even moderate Reynolds numbers, and the prospects for the future are cautiously pessimistic. Barring a revolution in computer architecture (quantum CPU) there is little hope that DNS will be available for "industrial" sized applications within my lifetime. Most commonly RANS and LES have been proposed as alternatives to DNS. As we have mentioned both of these have been shown to be insufficient in many aspects when utilizing traditional SGS models. Therefore it is necessary that new procedures continue to be developed.

Of recent interest has been the introduction of "synthetic velocity" models into the literature. For more on the methodology behind these models the reader is referred to the

recent review article by Domaradski and Adams [78] and the book by Sagaut [79]. There now exist several possible formulations of this type exemplified by the works of Domaradzki and co-workers (*e.g.* [80]), Kerstein and co-workers (*e.g.* [81]), Menon [82], and Scotti and Meneveau [83]. The feature common to all these approaches is direct modeling of fluctuating velocities (flow physics) rather than Reynolds stresses (flow statistics), although details of the modeling itself, and the way in which the synthetic velocities are employed, differs quite significantly from any one of the cited approaches to the next. Domaradzki and Saiki [80] and Scotti and Meneveau [83] use the synthetic velocity, however constructed, to calculate Reynolds stress (actually, large-eddy simulation subgrid-scale stresses) while the remainder of the investigators use the synthetic velocities more directly. The works of all the above mentioned investigators who do not employ Reynolds stresses use random behavior at some stage of construction and application of synthetic velocities. This can only be viewed as a detractor of these models.

2.3.3 Additive Turbulent Decomposition

Here we repeat the formulations of an attempt to remedy the before mentioned flaws of RANS and LES with a novel turbulence simulation procedure that, as will be seen, lends itself naturally to the use of the growing field of sythetic velocity models. This procedure involves a decomposition of the N.–S. equation into separate equations for the large and small scales by a projection method. This method is similar to the Galerkin methods that have been proposed by Temam and coworkers (see, *e.g.*, [84]) and has been shown by Brown *et al.* [85] to have error and convergence estimates similar to those for the first order Galerkin method in the two-dimensional case.

As we have mentioned previously, the idea of decomposing the N.–S. *solutions* into large- and small-scale components is well documented (see *e.g.* [76, 77]). In the recent work of Yang and McDonough [86], Hylin and McDonough [87, 88] and McDonough and Wang [89] the procedure of projecting the N.–S. equation into these subspaces of solutions and subsequent solution of the revised equations using highly efficient computational methods has come to be known as Additive Turbulent Decomposition (ATD). Here we will derive the ATD equations as propounded by Hylin and McDonough [88].

We begin with the incompressible N.–S. equation along with the incompressibility requirement;

$$\frac{\partial \boldsymbol{U}}{\partial t} + \boldsymbol{U} \cdot \nabla \boldsymbol{U} = -\nabla P + \nu \Delta \boldsymbol{U},$$

$$\nabla \cdot \boldsymbol{U} = 0.$$

We can then, following the procedure often done in mathematical analysis of the N.–S. equations (see, *e.g.*, Constantin and Foias [90]), project these equations into the divergence-free Sobolev subspace of solutions and apply appropriate scaling by a characteristic length and velocity;

$$\frac{\partial \boldsymbol{u}}{\partial t} + \boldsymbol{u} \cdot \nabla \boldsymbol{u} = \frac{1}{Re} \Delta \boldsymbol{u}. \tag{17}$$

Following the formalism of ATD given by Hylin and McDonough [88] these equations can be separated into small-scale and large-scale equations via the projection operators that separate the small and large wavelength components of the solution;

$$\boldsymbol{u_L} = \sum_{1}^{\boldsymbol{k} \leq \boldsymbol{k}_c} a_{\boldsymbol{k}}(t) \varphi_{\boldsymbol{k}}(\boldsymbol{x}) = \mathbb{P}_L(\boldsymbol{u}), \tag{18a}$$

$$\boldsymbol{u_S} = \sum_{\boldsymbol{k} > \boldsymbol{k}_c}^{\infty} a_{\boldsymbol{k}}(t) \varphi_{\boldsymbol{k}}(\boldsymbol{x}) = \mathbb{P}_S(\boldsymbol{u}). \tag{18b}$$

The N.–S. equation projected into the subspace of low wavenumber solutions is then

$$\frac{\partial \boldsymbol{u_L}}{\partial t} + \mathbb{P}_L[\nabla \cdot (\boldsymbol{u_L u_L}) + \nabla \cdot (\boldsymbol{u_L u_S}) + \nabla \cdot (\boldsymbol{u_S u_L}) + \nabla \cdot (\boldsymbol{u_S u_S})] = -\mathbb{P}_L \frac{1}{Re} \Delta (\boldsymbol{u_L} + \boldsymbol{u_S}), \tag{19}$$

with an analogous equation following for the evolution of the high wavenumber components, $\boldsymbol{u_S}$. This procedure allows for the direct use of synthetic velocities as models of the small-scale velocity, $\boldsymbol{u_S}$. We also see that substitution of the synthetic velocities has the effect to increase the resolution of the simulation since we have directly added back previously unresolved scales to those that are being resolved by the grid-scale calculations. In contrast usual RANS and LES procedures do not gain resolution as the implementation of SGS models in those cases only incurs using SGS results to calculate the next large-scale time step. In addition there is little room for misinterperation of the results since this type of procedure

makes use of a one-to-one mapping from physics to model results, whereas the Reynolds stresses and LES eddy viscosities essentially incorporate an infinity-to-one mapping from physics to model results as they are statistical models.

We must now consider finding a suitable model for the small-scale velocity wavevectors, $\boldsymbol{u_S}$, so that Eqn. (19) can be solved numerically. It has been our contention that since it is known that deterministically chaotic solutions to the Navier–Stokes equation exist (see [26]), and moreover, analysis of laboratory measurements of turbulent flow have shown deterministic behavior (see [71]), it is reasonable to employ this knowledge in models of turbulence. This was the rationale underlying the previously employed models of McDonough *et al.* [91, 92], and Hylin [93]. In those studies chaotic maps such as the logistic map, the "absolute value" logistic map, the tent map and linear combinations of these were used in the construction of the modeled small-scale velocities. In all of the above studies the small-scale velocity field is represented by:

$$\boldsymbol{q}^* = \boldsymbol{A}\boldsymbol{\zeta}\boldsymbol{M}, \tag{20}$$

where $\boldsymbol{q}^* = \boldsymbol{u_S}$ or can be viewed as the small-scale portion of the usual LES decomposition of dependent variables

$$\boldsymbol{Q}(\boldsymbol{x},t) = \boldsymbol{q}(\boldsymbol{x},t) + \boldsymbol{q}^*(\boldsymbol{x},t), \qquad \boldsymbol{x} \in \mathbb{R}^d, \quad d = 2,3, \tag{21}$$

where $\boldsymbol{q}(\boldsymbol{x},t)$ denotes the large- or resolved-scale part. In Eqn. (20) $\boldsymbol{A}$ is an amplitude factor derived from the Kolmogorov 2^{nd} similarity hypothesis (see, *e.g.,* [5]); $\boldsymbol{\zeta}$ is an anisotropy correction that has previously been computed via the *scale-similarity* hypothesis employed in dynamic SGS models [58], and $\boldsymbol{M}$ is the "stochastic variable" that introduces the turbulent-like fluctuations. We note that currently no anisotropy correction is being used as it has been dropped with a recent revision of the formulations.

However, in [92] it was found that using the above types of dynamical systems, *e.g.*, logistic maps, tent maps, etc., did not provide correct predictions of passive scalar fluctuations, leading McDonough and Huang [94] to seek "first principles" derivation of the fluctuating factor in (1) in the context of a reduced-kinetics model of H_2–O_2 combustion in a turbulent flow behind a splitter plate. Chapter IV will be dedicated to a derivation of a similar fluctu-

ating factor from the 3-D incompressible N.–S. equation that has come to be known as the "Poor Man's Navier-Stokes" (PMNS) equation and will be discussed in the sequel.

III. THE "POOR MAN'S NAVIER-STOKES" EQUATION

In the following sections we will derive the 3-D PMNS equation from the 3-D N.–S. equation in detail as this is the first formal presentation of this material. Next we will discuss the relations that are implied by this derivation between physics and PMNS bifurcation parameters. This is appropriate since we aim at finding *global* relationships between the two to be used in future simulations of general problems.

3.1 DERIVATION OF THE 3-D PMNS EQUATION

In this section we provide details of the derivation of the 3-D PMNS equation for the u-component velocity while the v- and w-component velocity derivations follow similarly. We start by making the substitution of a Fourier representation of the component velocities into the full 3-D, incompressible N.–S. equation (Eqn. 17), and we find that for the x-momentum portion we have

$$\sum_{-\infty}^{\infty}(a_{\boldsymbol{k}}(t)\varphi_{\boldsymbol{k}}(\boldsymbol{x}))_t + \sum_{-\infty}^{\infty} a_{\boldsymbol{k}}(t)\varphi_{\boldsymbol{k}}(\boldsymbol{x}) \sum_{-\infty}^{\infty}(a_{\boldsymbol{k}}(t)\varphi_{\boldsymbol{k}}(\boldsymbol{x}))_x + \sum_{-\infty}^{\infty} b_{\boldsymbol{k}}(t)\varphi_{\boldsymbol{k}}(\boldsymbol{x}) \sum_{-\infty}^{\infty}(a_{\boldsymbol{k}}(t)\varphi_{\boldsymbol{k}}(\boldsymbol{x}))_y +$$

$$\sum_{-\infty}^{\infty} c_{\boldsymbol{k}}(t)\varphi_{\boldsymbol{k}}(\boldsymbol{x}) \sum_{-\infty}^{\infty}(a_{\boldsymbol{k}}(t)\varphi_{\boldsymbol{k}}(\boldsymbol{x}))_z = \frac{1}{Re}\Delta \sum_{-\infty}^{\infty} a_{\boldsymbol{k}}(t)\varphi_{\boldsymbol{k}}(\boldsymbol{x}) \tag{22}$$

where

$$u = \sum^{\infty} a_{\boldsymbol{k}}(t)\varphi_{\boldsymbol{k}}(\boldsymbol{x}), \tag{23a}$$

$$v = \sum^{\infty} b_{\boldsymbol{k}}(t)\varphi_{\boldsymbol{k}}(\boldsymbol{x}), \tag{23b}$$

$$w = \sum^{\infty} c_{\boldsymbol{k}}(t)\varphi_{\boldsymbol{k}}(\boldsymbol{x}). \tag{23c}$$

If we now assume that the basis functions, $\varphi_{\boldsymbol{k}}(\boldsymbol{x})$, *act like* (with respect to differentiation) complex exponentials we can make the generalization that

$$\frac{d^2}{d\boldsymbol{x}^2}\varphi_{\boldsymbol{k}}(\boldsymbol{x}) = -(|\boldsymbol{k}|^2)\varphi_{\boldsymbol{k}}(\boldsymbol{x}). \tag{24}$$

and the revised x-momentum portion of the N.–S. equation becomes

$$\sum_{-\infty}^{\infty} \dot{a}_{\boldsymbol{k}}(t)\varphi_{\boldsymbol{k}}(\boldsymbol{x}) + \sum_{-\infty}^{\infty} a_{\boldsymbol{k}}(t)\varphi_{\boldsymbol{k}}(\boldsymbol{x}) \sum_{-\infty}^{\infty} m_1 a_{\boldsymbol{k}}(t)\varphi_{\boldsymbol{k}}(\boldsymbol{x}) + \sum_{-\infty}^{\infty} b_{\boldsymbol{k}}(t)\varphi_{\boldsymbol{k}}(\boldsymbol{x}) \sum_{-\infty}^{\infty} m_2 a_{\boldsymbol{k}}(t)\varphi_{\boldsymbol{k}}(\boldsymbol{x}) +$$

$$\sum_{-\infty}^{\infty} c_{\boldsymbol{k}}(t)\varphi_{\boldsymbol{k}}(\boldsymbol{x}) \sum_{-\infty}^{\infty} m_3 a_{\boldsymbol{k}}(t)\varphi_{\boldsymbol{k}}(\boldsymbol{x}) = \frac{-1}{Re} \sum_{-\infty}^{\infty} (|\boldsymbol{k}|^2) a_{\boldsymbol{k}}(t)\varphi_{\boldsymbol{k}}(\boldsymbol{x}). \tag{25}$$

If we now assume that the basis functions are orthonormal we can apply the well known Galerkin procedure to get an infinite set of equations corresponding to all wavenumbers

$$\dot{a}_k + \sum_{l,m} \left(m_1 a_l a_m \mathbb{A}^{(1)}_{klm} + m_2 b_l a_m \mathbb{A}^{(2)}_{klm} + m_3 c_l a_m \mathbb{A}^{(3)}_{klm} \right) = \frac{-1}{Re} |\boldsymbol{k}|^2 a_k, \quad (\forall \quad k). \tag{26}$$

Any number of models corresponding to particular truncations of the above equations, or those similar, are commonly known as "shell models" (see Bohr *et al.* [95]), the most popular of which is the Gledzer-Ohkitani-Yamada (GOY) turbulence model [96, 97]. Here we deviate from these treatments considerably and choose to retain only a single fixed wavevector from Eqn. (26). Since we are attempting to model only the high wavenumber solution components the choice to retain only one wave vector from this set of equations seems reasonable. In addition, linear combinations of the resulting equation might be used to model multiple wavenumber fluctuations, and this will be discussed in Chapter VI. The new equations for the Fourier coefficients of the u-, v-, and w-component velocities containing only one mode are

$$\dot{a} + m_1^{(1)} a^2 \mathbb{A}_1^{(1)} + m_2^{(1)} ab \mathbb{A}_2^{(1)} + m_3^{(1)} ac \mathbb{A}_3^{(1)} = \frac{-|\boldsymbol{k}|^2}{Re} a,$$

$$\dot{b} + m_1^{(2)} ab \mathbb{A}_1^{(2)} + m_2^{(2)} b^2 \mathbb{A}_2^{(2)} + m_3^{(1)} bc \mathbb{A}_3^{(3)} = \frac{-|\boldsymbol{k}|^2}{Re} b,$$

$$\dot{c} + m_1^{(3)} ac \mathbb{A}_1^{(3)} + m_2^{(3)} bc \mathbb{A}_2^{(3)} + m_3^{(1)} c^2 \mathbb{A}_3^{(3)} = \frac{-|\boldsymbol{k}|^2}{Re} c.$$

Working with only the x-momentum equation we apply a forward Euler discretization to find that

$$a^{n+1} = a^n - \tau \left[\frac{|\boldsymbol{k}|^2}{Re} a^n + \tilde{\mathbb{A}}_1 (a^n)^2 + \tilde{\mathbb{A}}_2 a^n b^n + \tilde{\mathbb{A}}_3 a^n c^n \right].$$

Rearranging we find

$$a^{n+1} = \tau\tilde{\mathbb{A}}_1 a^n \left(\frac{1 - \tau|\boldsymbol{k}|^2/Re}{\tau\tilde{\mathbb{A}}_1} - a^n \right) - \tau(\tilde{\mathbb{A}}_2 a^n b^n + \tilde{\mathbb{A}}_3 a^n c^n).$$

Making the algebraic substitutions

$$1 - \frac{\tau|\boldsymbol{k}|^2}{Re} = \tau\tilde{\mathbb{A}}_1 = \beta_1,$$

$$\gamma_{1,2} = \tau\tilde{\mathbb{A}}_2,$$

$$\gamma_{1,3} = \tau\tilde{\mathbb{A}}_3,$$

and grouping this new equation with its analogs in the y- and z-momentum equations we arrive at the 3-D discrete dynamical system (DDS) that we call the 3-D "Poor Man's Navier-Stokes" equation, shown here:

$$a^{n+1} = a^n\beta_1(1 - a^n) - \gamma_{1,2}a^n b^n - \gamma_{1,3}a^n c^n, \tag{27a}$$

$$b^{n+1} = b^n\beta_2(1 - b^n) - \gamma_{2,1}a^n b^n - \gamma_{2,3}b^n c^n, \tag{27b}$$

$$c^{n+1} = c^n\beta_3(1 - c^n) - \gamma_{3,1}a^n c^n - \gamma_{3,2}b^n c^n. \tag{27c}$$

In this system of equations, (n) represents a map iteration counter which can be related to a formal numerical time step index; a, b and c are Fourier coefficients as in Eqns. (23), but with wavevector notation suppressed. The βs and γs are *bifurcation* parameters whose connection to physics will be discussed in the following subsection. Note that Eqns. (27) are not the only DDS that can be arrived at by employing this procedure but are instead only the one-of-many which corresponds to the specific algebraic simplifications we have performed.

4.2 RELATING BIFURCATION PARAMETERS TO PHYSICS

Recall that in the previous section we showed that

$$\beta_1 \sim \left(1 - \frac{1}{Re}\tau|\boldsymbol{k}|^2\right).$$

Noting the flexibility of that derivation with respect to the unknown Galerkin triple products the inclusion of an $\mathcal{O}(1)$ normalization constant is reasonable and is consistent with the treatment of the logistic map by May [98] performed so that the mapping was of the unit interval onto itself. The following is then the form of the βs that is currently in use in the turbulence model:

$$\beta_i = C\left(1 - \frac{1}{Re_i}\tau|\boldsymbol{k}|^2\right). \tag{28}$$

In the previous definition Re_i is the "directional" Taylor microscale Reynolds number (which we will show to be closely approximated by the directional cell Reynolds number); τ is the small-scale time step arising in a forward Euler discretization of the Galerkin representation of the N.–S. equation, $\boldsymbol{k}$ is the wavevector that we are attempting to model, and C is an $\mathcal{O}(1)$ normalization constant that will hopefully be found from analysis of experimental or DNS data. In Eqn. (28) we see the dependence of βs on a wavenumber-time step product as well as with Re. If we assume that $\tau|\boldsymbol{k}|^2 < Re$ then we can show that $\beta \to C$ as $Re \to \infty$. We will see that, with sufficiently large choice of $|C|$, this implies that Eqns. (27) exhibit increasingly chaotic behavior (modulo certain windows of periodicity), just as N.–S. solutions do as $Re \to \infty$.

To begin we first recognize that we will, hopefully, be resolving with the grid-scale calculations wavenumber fluctuations that are approximately half-way through the inertial subrange, though it is quite possible that we would resolve less than this if calculating at high Reynolds numbers. If this is so we can associate the information from the high-pass filtering of the grid-scale results with the Taylor microscale. Thus, assuming some overlap in the resolved scales and scales to be modeled, we can assume that the appropriate nondimensional time step would be the reciprocal of the norm of the strain rate tensor, $||\boldsymbol{S}||^{-1} = \tau_t$, of the high wavenumber content (high-pass filtered) of our resolved-scale calculation nondimensionalized by the resolved-scale time step size, Δt:

$$\tau = \frac{||\boldsymbol{S}||^{-1}}{\Delta t}.$$

Next we consider the wave vector $\boldsymbol{k}$. To obtain a wavevector we need to make the common assumption that the Taylor microscale Reynolds number is approximately the square root

of the integral scale Reynolds number:

$$Re_\lambda = Re_\ell^{1/2} = \left(\frac{u'_{rms} l}{\nu}\right)^{1/2}. \tag{29}$$

In the above equation $u'_{rms} = \langle (u(\boldsymbol{x},t) - \langle u \rangle(t))^2 \rangle^{1/2}$ is the root mean square velocity fluctuations, and ℓ is a length scale typically viewed as the reciprocal of the wavenumber k at which the energy spectrum $E(k)$ achieves its maximum and often approximated as $\ell = 0.2L$, where L is the length scale of the domain. In two dimensions these quantities will be averaged over the local 9-point stencil, and in three dimensions over the local 27-point stencil in space–not in time. From the definition of the Taylor microscale Reynolds number ($Re_\lambda = u'_{rms}\lambda/\nu$) we then find that

$$\lambda = \left(\frac{\nu}{\langle u'^2 \rangle^{1/2}}\right)^{1/2} \ell^{1/2}. \tag{30}$$

This lengthscale can then be used to approximate the wavevector(s) as

$$k_i = \frac{1}{\lambda_i}.$$

Considering the γs we recall that

$$\gamma_{1,2} = \tau m_2^{(1)} \mathbb{A}_2^{(1)}. \tag{31}$$

In the above the factor $m_2^{(1)}$ has been separated from, and arises as part of, the Galerkin representation of $\partial u/\partial y$ when constructing Galerkin inner products (with $\boldsymbol{\varphi_k}$) with Eqn. (26);

$$\begin{aligned} v u_y &= \left(\sum_{\ell_1,\ell_2} b_{\ell_1,\ell_2} \varphi_{\boldsymbol{\ell}}\right)\left(\sum_{m_1,m_2} m_2 a_{m_1,m_2} \varphi_{\boldsymbol{m}}\right) \\ &= \sum_{\ell_1,\ell_2,m_1,m_2} m_2 a_{m_1,m_2} b_{\ell_1,\ell_2} \varphi_{\boldsymbol{\ell}} \varphi_{\boldsymbol{m}}\,, \end{aligned}$$

with the subscript y indicating partial differentiation. In the same fashion the other coefficients in the definitions of the γ can be associated with various elements of the strain-rate

tensor, and this suggests that we should set

$$\gamma_{i,j} \sim \tau \frac{\partial u_i}{\partial x_j},\ i,j = 1,2,3\ i \neq j.$$

By a similar argument as that which we used in the case of the βs we include an $\mathcal{O}(1)$ normalization constant in practice:

$$\gamma_{i,j} = C\big(\tau \frac{\partial u_i}{\partial x_j}\big),\ i,j = 1,2,3\ i \neq j. \tag{32}$$

This equation is straightforward to calculate but needs to be considered more deeply. Foremost, the derivatives in the above relationship are to approximate small-scale derivatives and are calculated using high-pass filtered grid-scale results (possibly using discrete operator interpolation to enhance wavenumber content (see Yang *et al.* and Xu *et al.* [99, 100]), and thus the derivatives should be taken with respect to the Taylor microscale length as opposed to the normal grid spacing.

Next we show semi-quantitatively that the appropriate choice for the Reynolds number of Eqn. (28) is the cell Reynolds number Re_h. We start by making the approximation

$$|u'| = |u - \langle u \rangle| \sim h \left| \frac{\partial u}{\partial x} \right|. \tag{33}$$

Then we can write

$$\langle u'^2 \rangle^{1/2} \sim h \left| \frac{\partial u}{\partial x} \right|. \tag{34}$$

It follows that the Taylor microscale Reynolds number is of the same order as the cell Reynolds number if h is approximately the size of λ. In general, we expect $h > \lambda$ to hold, but especially when nonuniform gridding is used the factor relating these two quantities will be $\mathcal{O}(1)$ in regions of intense turbulence where the model must be most accurate. Thus, choosing $Re = Re_h$ in the formulas for the βs is justified.

Turning our attention to the amplitude factors we recall that they are given as [101]

$$A_i^2 \cong \sum_{n=1}^{\infty} E_i^*(\boldsymbol{k}_n^{loc}). \tag{35}$$

To begin it is then necessary to find the energy components of the high-passed information to calculate the amplitude factors. These energies are formulated per unit wavenumber so that in the end we should rescale these by multiplication by the square root of the grid cell area. We first recall that it is possible to relate energy to the second-order structure function as

$$kE(k) = \mathbb{S}_2(k), \tag{36}$$

and from Kolmogorov theory we can argue that the second-order structure function can be related to scaling constants as

$$\mathbb{S}_2(l) \equiv \langle (u(\boldsymbol{x} + \boldsymbol{l}) - u(\boldsymbol{x}))^2 \rangle = C_2 \langle \epsilon \rangle^{\beta} l^{\beta}, \tag{37}$$

where $\beta = 2/3$ is the classic Kolmogorov exponent, C_2 is the Kolmogorov constant, and ϵ is the energy dissipation per unit mass. Therefore we find

$$E(k) = C_2 \langle \epsilon \rangle^{\beta} k^{-(\beta+1)}. \tag{38}$$

Depending on the gridding used, multiple (N_l) structure functions can be found corresponding to local vectors $\boldsymbol{l}$ for the grid-point stencil. With this in mind we introduce a least squares procedure to find the local scaling exponents and constants, and thus enable the determination of the energy values. Consider

$$Q(C_2, \beta) = \sum_{n=1}^{N_l} \left[S_2(l_n) - C_2 \langle \epsilon \rangle^{\beta} l_n^{\beta} \right]^2$$

where this value is to be minimized in accord with the above arguments. Thus we should allow $\frac{\partial Q}{\partial C_2} = 0$ and $\frac{\partial Q}{\partial \beta} = 0$. Through considerable algebra it can be shown that this problem reduces to finding $A_n = \log S_2(l_n)$ and $B_n = \log(\langle \epsilon \rangle l_n)$. Then $C_2 = 10^{C_2^*}$ where

$$C_2^* = \frac{\left(\sum A_n\right)\left(\sum B_n^2\right) - \left(\sum A_n B_n\right)\left(\sum B_n\right)}{N_l \left(\sum B_n^2\right) - \left(\sum B_n\right)^2},$$

and

$$\beta = \frac{N_l\left(\sum A_n B_n\right) - \left(\sum A_n\right)\left(\sum B_n\right)}{\left(\sum B_n\right)^2}.$$

Here A_ns are simply the log of the structure functions and B_ns are the logarithm of dissipation times the length over which the structure function corresponding to n was calculated as stated before.

The dissipation is normally calculated by multiplying the kinematic viscosity by the strain rate with averages taken over the stencil of nearest (spatial) neighbors. We now have the proper number of equations to calculate the localized energy values needed for calculation of the amplitude factor the SGS model.

IV. STUDY OF THE 2-D PMNS EQUATION

In an analogous derivation to that presented in the previous section McDonough and Huang have shown [102] that the 2-D PMNS equations are given by the following *discrete dynamical system* (DDS):

$$a^{(n+1)} = a^{(n)}\beta_u\left(1 - a^{(n)}\right) - \gamma_u a^{(n)} b^{(n)}, \tag{39a}$$

$$b^{(n+1)} = b^{(n)}\beta_v\left(1 - b^{(n)}\right) - \gamma_v a^{(n)} b^{(n)}. \tag{39b}$$

These equations are much simpler to study than the full 3-D PMNS equations since the number of independent parameters (initial conditions plus bifurcation parameters) is reduced from 12 to 6. Here we will study these equations in detail.

To study the PMNS it is necessary that we develop accurate and efficient tools since, as you will see, there is an almost overwhelming amount of information to be gathered. Here we introduce the tools that we have found to be most useful and then use these to study the 2-D PMNS equation. This simplified version of the 3-D equation will be studied so that the reader may become familiar with the terms and concepts that will later be used to study the 3-D PMNS equation and develop a basic understanding of the behavior of similar systems.

Most of the calculations reported here were performed in series or parallel mode using double precision (64-bit) FORTRAN 90 arithmetic on a HP Superdome symmetric multiprocessor at the University of Kentucky Computing Center and its forerunner a HP N-4000. Additional computations were made on a HP J2240 workstation in the Computational Fluid Dynamics Laboratory at the University of Kentucky. The runs generally consisted of 5×10^4 iterations of the DDSs studied here for each set of parameter values while power spectra were computed using the last 8192 points of the time series using a standard radix-2 FFT.

4.1 $\gamma_u = \gamma_v = 0$

In study of the above equations we should first note that by setting $\gamma_u = \gamma_v = 0$ we recover an uncoupled set of logistic maps. The logistic map was originally studied by P. Verhulst [103] as a simplistic population growth model and was popularized by R. May [98]. This map has

been studied extensively so it is a good place to start the discussion of the dynamics of our equations. As a model of population growth allowing $\beta < 0$ does not make sense so almost always studies are performed only for $\beta > 0$. But, in our case there is no such restriction on β so we choose to look at the entire range of β values where nondivergent solutions occur.

To begin this study we first present the so-called bifurcation diagram of the logistic map in Figure 2. This diagram was created by allowing β to cycle through values between -2 and 4 and iterating the equation

$$a^{(n+1)} = a^{(n)}\beta\left(1 - a^{(n)}\right),$$

starting with an initial value of $a^{(0)} = 0.4$, for some large number of iterations (500000) before a set number of iterations (10000) were plotted on the y-axis against the β values on the x-axis. The examination of Figure 2 reveals that *pitchfork bifurcations* occur at $\beta = -1$ and

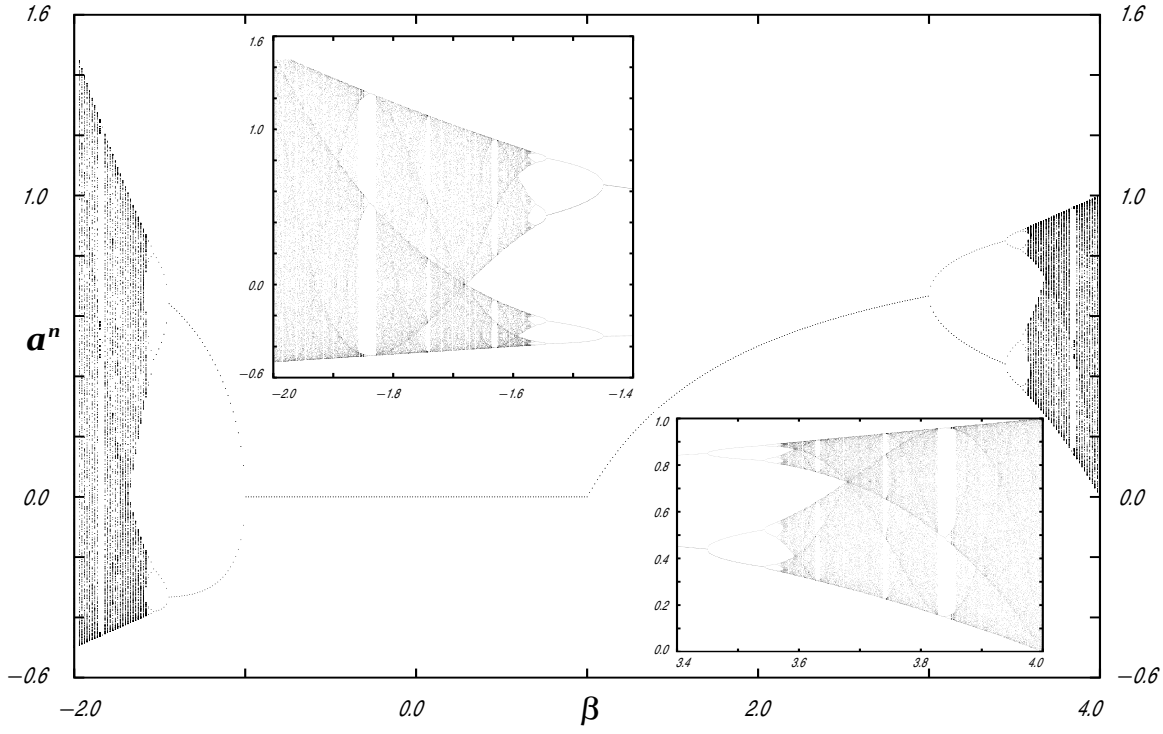

Figure 2: Bifurcation diagram of the 1-D logistic map for the interval $\beta \in [-2, 4]$.

$\beta = 3$ from steady to periodic states which are then followed by successive bifurcations to lower frequency subharmonics. The term bifurcation comes from the Latin *furca* and literally means to "fork into two" though generally it indicates a qualitative (often discontinuous) change in the behavior of a system as a control parameter is varied continuously. These bifurcations continue as the magnitude of the bifurcation parameter is continually increased and are known as *period doubling cascades* to chaos. M. Feigenbaum [104] has shown that the ratio of successive distances (in parameter units) between such bifurcations (in a related system) is a constant found to be $\delta \approx 4.669$ and conjectured that this constant would hold for all maps that are quadratic. This has been proven rigorously by Lanford [105]. Noting that this ratio implies that the sequence is converging it is also known (for the positive β case) that the *accumulation point* of these period doublings is $\beta \approx 3.569945672$.

What, then, occurs after the accumulation points have been surpassed? As can seen from Figure 2 the trajectory is not as easily described and such erratic behavior as is seen, with certain well-known attributes, is called *chaotic* (though not all parameter values after the accumulation points exhibit chaotic trajectories, see, *e.g.*, the period three window at 3.82). The following common definition of chaotic behavior is taken from R. Devaney [106]. A function $\boldsymbol{f} : \boldsymbol{V} \rightarrow \boldsymbol{V}$ is chaotic if:

1. Periodic points are dense in $\boldsymbol{V}$
2. $\boldsymbol{f}$ is topologically transitive
3. $\boldsymbol{f}$ displays *sensitivity to initial conditions* (SIC)

In other words, an infinity of periodic fixed points are existent, but they are repelling fixed points; any arbitrary open interval will become sufficiently mixed, under the action of $\boldsymbol{f}$, throughout all of $\boldsymbol{V}$; and any two arbitrarily nearby initial conditions will lead to very different trajectories (though they will possibly lie on the same *attractor*). An attractor, as defined by Takens [107], is a closed set, $\boldsymbol{A}$, such that any trajectory $\boldsymbol{x}$ that starts in $\boldsymbol{A}$ stays in $\boldsymbol{A}$ for all time, attracts some neighborhood of points after a sufficiently long time, and is invariant for all times thereafter ($\boldsymbol{f}\boldsymbol{A} = \boldsymbol{A}$), *i.e.* there is no subset of $\boldsymbol{A}$ which satisfies the above conditions. An attractor can be considered *chaotic* if its trajectories exhibit sensitivity to initial conditions and can often be distinguished as such by an asymptotic measure, *e.g.*, its characteristic exponent. In addition the term *strange* is applied to an attractor if it is seen

to display *fractal* attributes such as self-similarity and "nesting", as described by Mandlebrot [108]. This short description of the chaotic behavior associated with the family of quadratic maps will conclude our discussion on this simplification of the 2-D PMNS equation.

4.2 $\beta_u = \beta_v$, $\gamma_u = \gamma_v$

A still more realistic simplification was almost always implemented in the initial stages of this study. Specifically we allowed equality between like bifurcation parameters in the u and v equations which permitted us to investigate a 2-D parameter space as opposed to a 4-D parameter space (if we ignore that initial conditions might also act as bifurcation parameters). These initial studies of Eqns. (39), where it was required that $\beta_u = \beta_v$ and $\gamma_u = \gamma_v$, have been reported by McDonough and Huang [102] and Bible and McDonough [109]. Most importantly [102] established the 13 nondivergent types of behavior seen for this set of equations and recognized power spectral density (PSD) analysis as an appropriate method of solution classification. In addition the three common bifurcation sequences to chaos and two types of intermittencies were identified. The study in [109] investigated the sensitivity to initial conditions of this system and the coexistence of multiple attractors over closed sets of initial conditions. Here we will summarize the most important findings of these two studies and, in addition, investigate behavior for $\beta < 0$ which was previously uninvestigated.

4.2.1 Power Spectral Densities

We begin by listing the 14 types of behavior seen in time series resulting from the iteration of Eqns. (39) that have been identified [102] from their psds: *i)* steady, *ii)* periodic, *iii)* periodic with different fundamental frequency, *iv)* subharmonic, *v)* phase locked, *vi)* quasiperiodic, *vii)* noisy subharmonic, *viii)* noisy phase locked, *ix)* noisy quasiperiodic with fundamental, *x)* noisy quasiperiodic without fundamental, *xi)* broadband with fundamental, *xii)* broadband with different fundamental, *xiii)* broadband without fundamental, *xiv)* divergent. In Figure 3 we present examples of normalized psds from each of the above "non-noisy" classifications excluding steady (trivial) and divergent (nonstationary) in order of increasing perceivable

complexity. All of these behaviors were observed when iterations of Eqns. (39) were performed using the default initial conditions ($a^0 = 0.4, b^0 = 0.61$), as are all of the calculations described here unless otherwise noted. In Figure 3(a) the power spectrum of a periodic

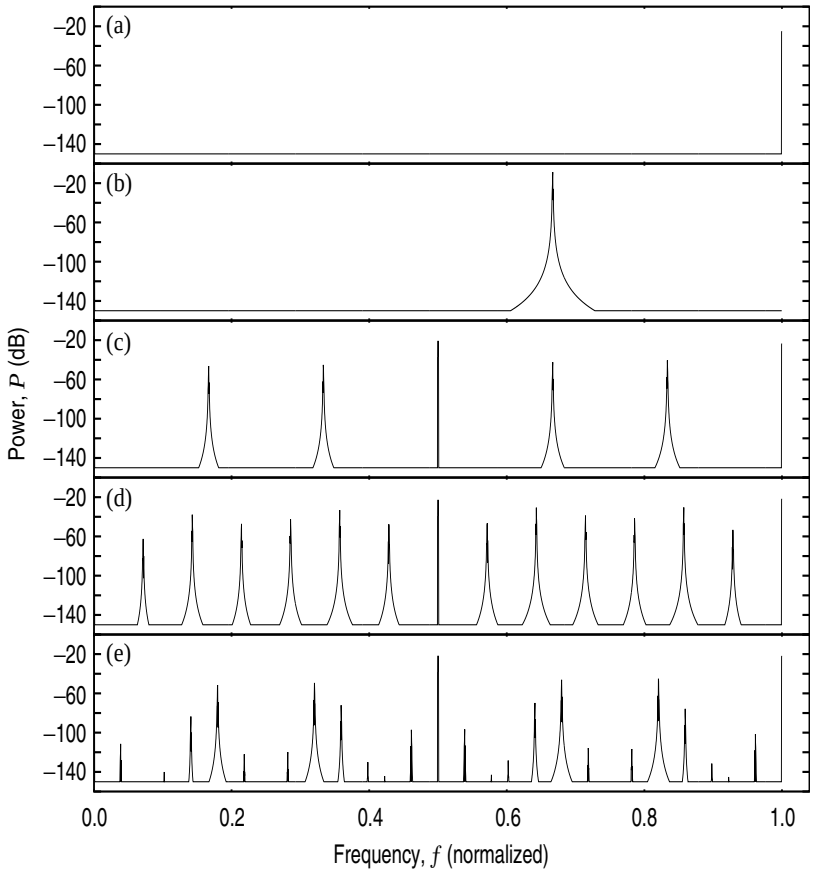

Figure 3: PSDs of example nonnoisy time series for; (a)$\beta = -1.4, \gamma = -0.45$, (b)$\beta = -1.84, \gamma = -0.17$, (c)$\beta = -1.8, \gamma = -0.332$, (d)$\beta = -1.37, \gamma = 0.27$, (e)$\beta = -1.34, \gamma = 0.27$

trajectory is seen. Periodicity is the most abundant type of behavior, aside from steady and divergent, seen for any of the DDSs studied here. From a modeling standpoint it has yet to be decided if periodic regimes should be allowed for use in the SGS model of turbulence, whereas it is obvious that the model should be "turned off" if the PMNS equation were to produce steady or divergent behavior (*i.e.* steady fluctuations are not associated with turbulence). If so we would like to avoid the bifurcation parameter ranges that are found to be producing periodic trajectories. Occasionally the mapping produces trajectories that are periodic with a different fundamental frequency (period 3). A typical psd for this class

of motion is seen in Figure 3(b). It has been shown by Li and Yorke [110] that the presence of period three trajectories implies that the system behaves chaotically at some parameter value. In Figure 3(c) we present the psd of a trajectory that has gone through a sequence of pitchfork bifurcations (period doubling → period doubling → period tripling) to produce subharmonic (period 12) behavior. Figure 3(d) displays the psd of a phaselocked trajectory. Phaselocking occurs in quasiperiodic regimes when the noncommensurrate frequencies (see previous discussion) of the quasiperiodic motion become commensurate. Finally, Figure 3(e) shows the psd of an example trajectory from the quasiperiodic classification. Such behavior has been explained previously and for more details see, *e.g.*, Frøyland [111].

In Figure 4 we present the psds for the remaining noisy behaviors. First, in Figure 4(a), is the psd of a noisy subharmonic (period 8) trajectory. Two very sharp spectral peaks are seen at the fundamental and second harmonic along with smaller "humps" at the third harmonic which rise about 15 decibels (dBs) above the dynamic noise. Second, in Figure 4(b) we present a psd of a noisy phase locked trajectory. The phase lock was of period 60 and the original quasiperiodicity was of much lower power than the period 12 subharmonic from which it originated. This leads (in the noisy case) to dynamical noise of proportional power to the quasiperiodicity and therefore it is difficult to distinguish the psd of Figure 4(b) as noisy phaselock as opposed to noisy subharmonic. Indeed even clean phaselocks can sometimes only be differentiated from subharmonic trajectories by knowledge of the bifurcation sequence that preceded or details in the power spectrum (peak amplitudes) and sometimes not at all. For these reasons they have been the most difficult type of behavior to identify correctly.

In Figures 4(c) and (d) are the noisy quasiperiodic trajectory psds with and without, respectively, the fundamental frequency still present. In the first case the quasiperiodic peaks are easily seen rising 15-25 dBs above the base noise and are thus easily identifiable. In the latter case the noise has continued to rise and the quasiperiodic peaks are more difficult to distinguish. This difficulty has sometimes led to the misidentification of trajectories nearing divergence with high levels of noise. This cannot be avoided as arbitrary rules concerning peak amplitudes must be used to "image process" the psd automatically and should not deter us from attempting to differentiate these types of noisy behavior. We will

remark more on the accuracy of our characterization scheme throughout. The final three behaviors are termed broadband due to their lack of any defining spectral characteristics, excluding the first harmonic. Figure 4(e) is the psd for broadband with the fundamental, 4(f) that for broadband with a different fundamental, and 4(g) that for broadband without the fundamental. One should notice that there are small humps that resemble quasiperiodicity

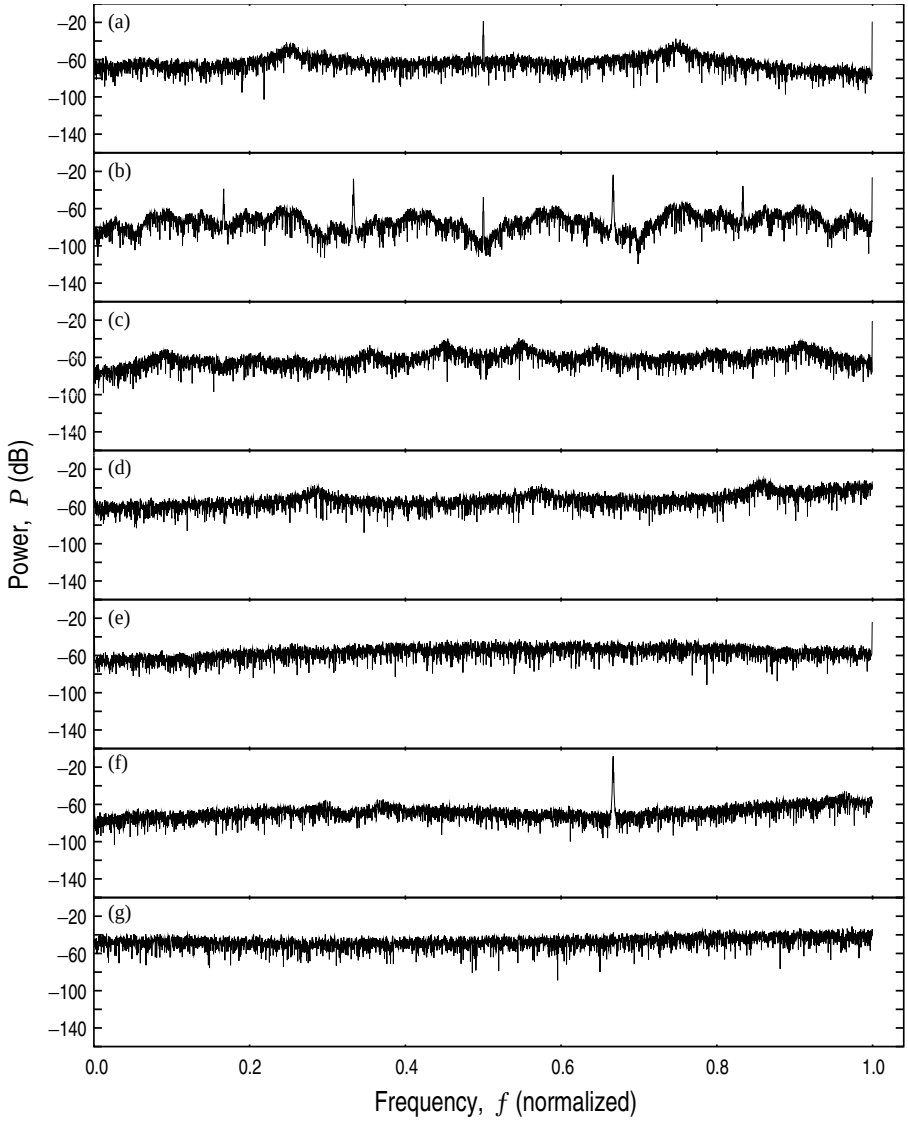

Figure 4: PSDs of example noisy time series for (a)$\beta = -1.56, \gamma = -2.623$, (b)$\beta = -1.602, \gamma = 3.22$, (c)$\beta = -1.26, \gamma = 0.43$, (d)$\beta = -1.75, \gamma = -1.84$, (e)$\beta = -1.64, \gamma = 0.15$, (f)$\beta = -1.84, \gamma = -0.985$, (g)$\beta = -1.9, \gamma = 3.8$

in the different fundamental case that raise doubt to the true dynamics of the trajectory.

Through numerical experiments we have confirmed that this case is indeed broadband with a different fundamental as it is born from the bifurcation sequence: period tripling → period doubling cascade → increasing noise, decreasing harmonic peak amplitudes (except first harmonic). This sequence is reminiscent of that at higher values of β ($\beta \approx 3.83$) for the 1-D logistic map (see Figure 2).

4.2.2 Time Series and Regime Map

Time series analysis is a very important aspect of studying dynamical systems and is attempted in this section, though this treatment is only cursory. In addition a particularly efficient method is introduced for viewing the effects of bifurcation parameter values on bifurcation sequences when the system contains multiple parameters. These concise plots are what we call regime maps and the details of these are discussed.

We begin by presenting the iteration histories (time series) of Eqns. (39) for a number of cases. Particularly, Figure 5 presents plots of u-component time series, lettered from (a) to (l), using the same ordering that was used previously for the psds, *i.e.* from periodic to broadband without the fundamental, corresponding to the power spectra of the previous section (Figures 3 and 4).

We first note two generalities that we have noticed. First it is found to be the case that periodic with a different fundamental behaviors, *e.g.* Figure 5(b), customarily exhibit larger magnitude fluctuations than normal periodicities, *e.g.*, Figure 5(a), as we would expect by analogy with the logistic map. It is also the case that chaotic fluctuations for the cases investigated here, using only $\beta < 0$ are generally greater in magnitude than those seen for previous studies using $\beta > 0$ (see [102]), as is also the case for the logistic map (see Figure 2).

From Figure 5 one should recognize that distinguishing behaviors by inspection of time series is likely to be extremely difficult. Most astounding are the similarities between the non-noisy quasiperiodic signal (Figure 5(e)) and the noisy subharmonic signal (Figure 5(f)), which are easily distinguishable from their power spectra. It could possibly be argued, though, that the extremely "turbulent" time series for the broadband with a different fundamental frequency (Figure 5(k)) and broadband without the funamental frequency (Figure 5(l)) are

qualitatively distinguishable from their peers, but not from one another. We note that we have not presented any intermittent time series here as such cases have been thoroughly discussed in [102] and mentioned briefly in the sequel.

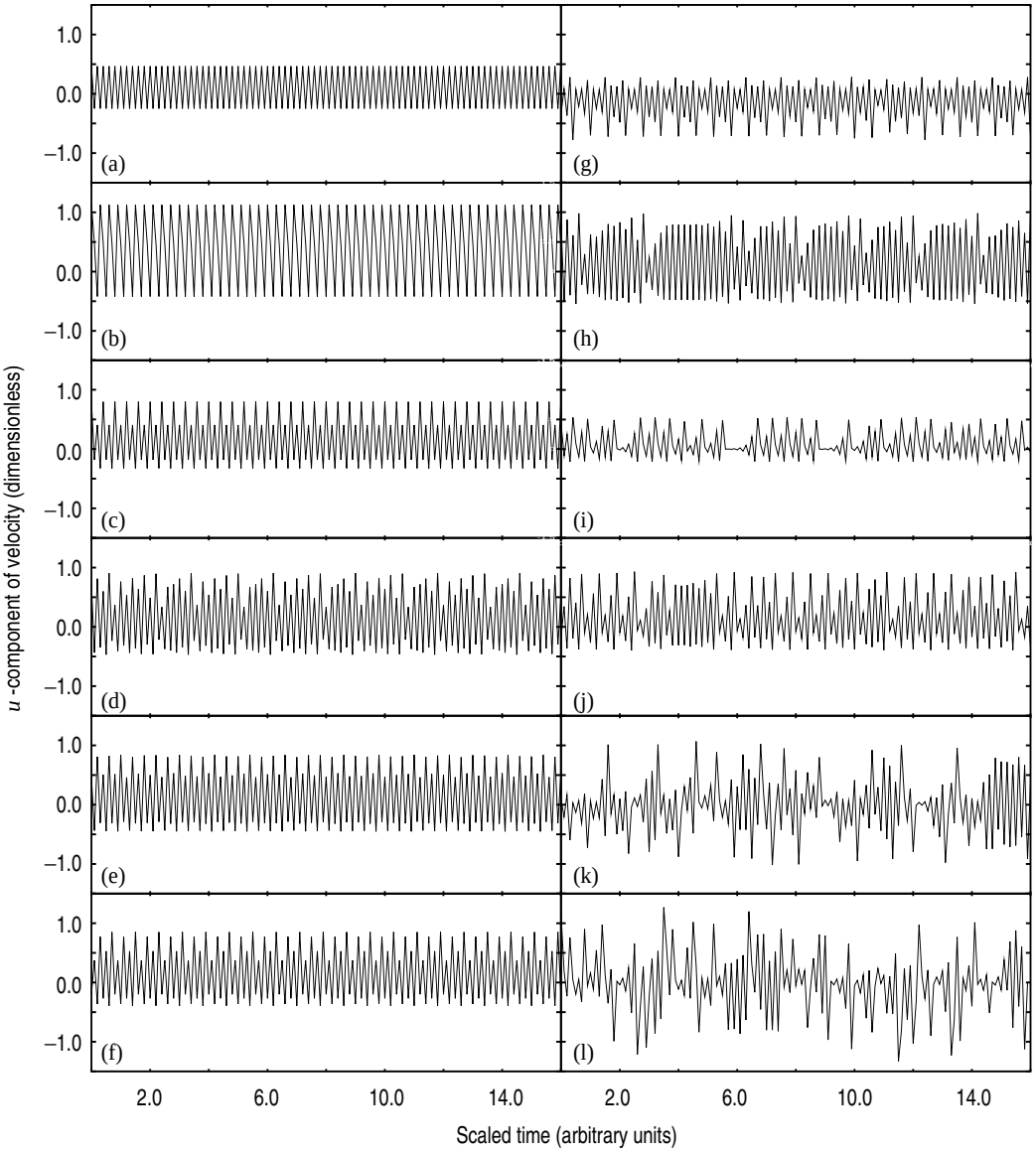

Figure 5: Time series corresponding to the PSDs of the previous section, ordered from (a) to (l) with increasing complexity as before.

The most appropriate method of studying a large number of cases (sets of bifurcation parameters along with initial conditions) of Eqns. (39) is to view a so-called regime map. Regime maps can be thought of as multidimensional bifurcation diagrams and are visual

representations of the types of behavior seen at combinations of relevant parameter values. The regime maps presented in this paper were created using a type of visual recognition algorithm [112] that recognizes distinctive traits in the automatically calculated power spectrum which is run for each grid point on a grid of bifurcation parameter values. The plots are then created, based on the result of the image processing algorithm, by color coding the 14 different types of behavior that have been described. The first regime map that we present (Figure 5(a)) is that for the case where $\beta_u = \beta_v$ and $\gamma_u = \gamma_v$ that we have been considering thus far. Near the regions of interest ($-2 \leq \beta \leq -1$, $3 \leq \beta \leq 4$) fine gridding of the parameter space has been used, and for the largely noninteresting region between these ranges a coarser grid has been employed. Specifically the finer grids are of 1001×3601 grid points resulting in grid spacings of $\Delta\beta = 0.001$ and $\Delta\gamma = 0.002$, and the coarse grid is 1001×1801 resulting in $\Delta\beta = 0.004$ and $\Delta\gamma = 0.004$, for a total of over 9 million combinations of β and γ values at which Eqns. (39) were iterated. The power spectrum was computed (most often for the u-component Fourier coefficient), and the type of behavior was classified, recorded, and plotted. We note that we have used here what we will refer to as the default initial conditions for the 2-D equations. These are $a^0 = 0.4$ and $b^0 = 0.61$ and, as of now, can be considered arbitrary choices. The color table of Figure 5(b) associates the 14 types of behavior with the respective colors that we have chosen to represent them.

One important aspect of regime maps of this type is that they allow for easy identification of bifurcation sequences and the chaotic regimes associated with each of these. For example, we can see that when $\gamma = 0$ the regime map of Figure 6 indicates that the 2-D PMNS equations proceed through the usual period doubling route to chaos, as it should:

$$\text{chaotic} \leftarrow \text{subharmonic} \leftarrow \text{periodic} \leftarrow \text{steady} \rightarrow \text{periodic} \rightarrow \text{subharmonic} \rightarrow \text{chaotic}.$$

In addition there are multiple regions which exhibit the Ruelle-Takens-Newhouse (RTN) scenario:

$$\text{steady} \rightarrow \text{periodic} \rightarrow \text{quasiperiodic} \rightarrow \text{chaotic}.$$

For instance, the region corresponding to $1 \leq \beta \leq 3.1$ where quasiperiodicity and subsequent chaos is seen as γ is decreased (starting at $\gamma \approx -0.2$ proceeding to $\gamma \approx -1.1$, dependent

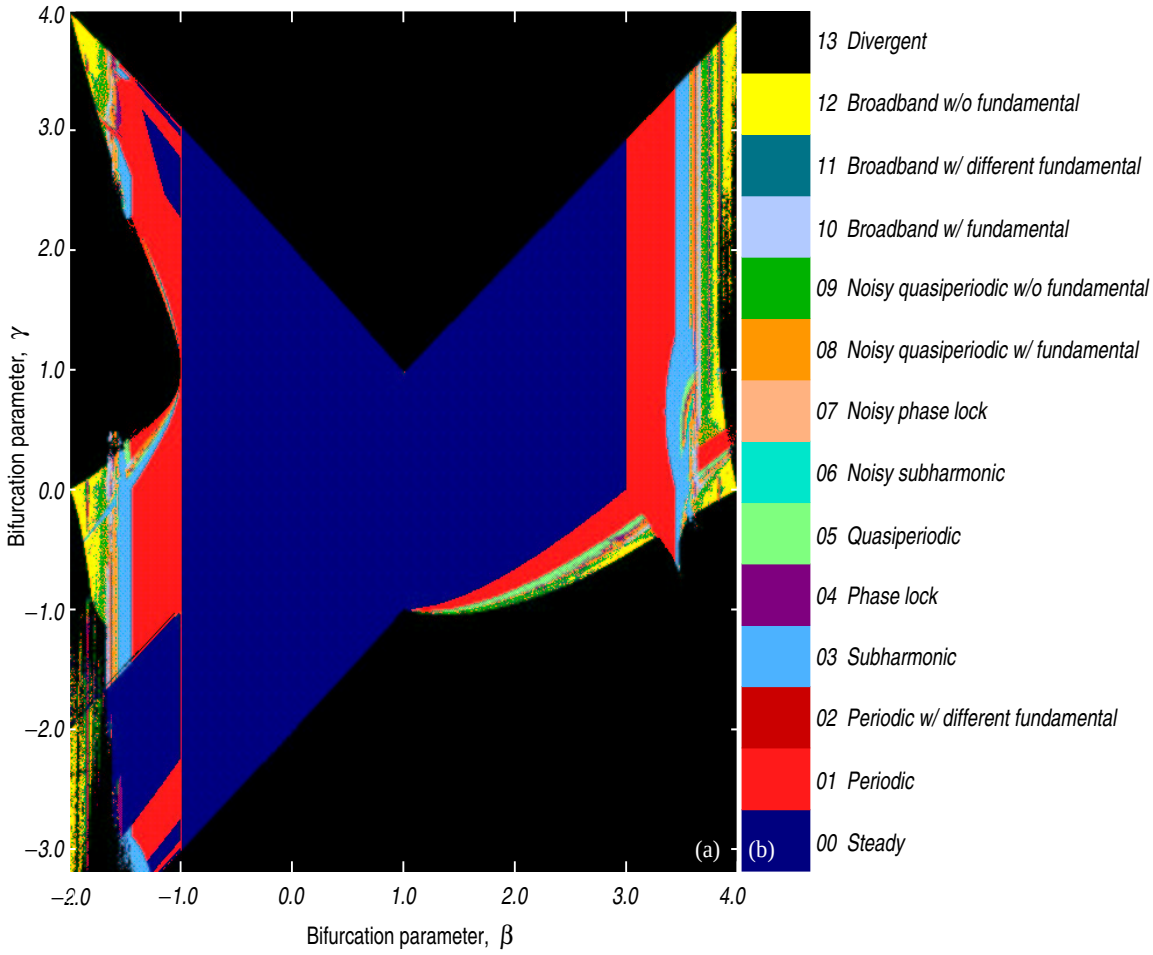

Figure 6: Regime map of 2-D PMNS equation with $\beta_u = \beta_v$ and $\gamma_u = \gamma_v$.

upon the value of β) was first introduced and studied in [102]. In addition the region $3.64 \leq \beta \leq 4.0$, $0.2 \leq \gamma \leq 0.4$ also displays this sequence and is associated with the large area of reemergent periodicity at high values of β that is sometimes, depending on the initial conditions implemented, connected to the initial periodic region by a periodic "bridge" [102]. Furthermore if we distinguish between the RTN scenario and a similar scenario through subharmonics, particularly

$$\text{steady} \rightarrow \text{subharmonic} \rightarrow \text{quasiperiodic} \rightarrow \text{chaotic},$$

an analogous "tail" of solutions to that seen for $\beta > 0$ is seen in the range $-1.5 \leq \beta \leq -1.0$,

$0.1 < \gamma \leq 1.0$, though the reader may need to view Figure 7 to distinguish this sequence. Additionally this transition exists for the range $3.5 \leq \beta \leq 3.6$, $0.3 \leq \gamma < 1.0$. All of these transitions are supposed to have very different dynamics leading to quite different types of chaos, as can be seen in the psds we presented earlier. Note that this is not a comprehensive list of all of the sequences to chaos of the mapping (as is evident in Figure 6(a)) but merely describes those that are the most visible.

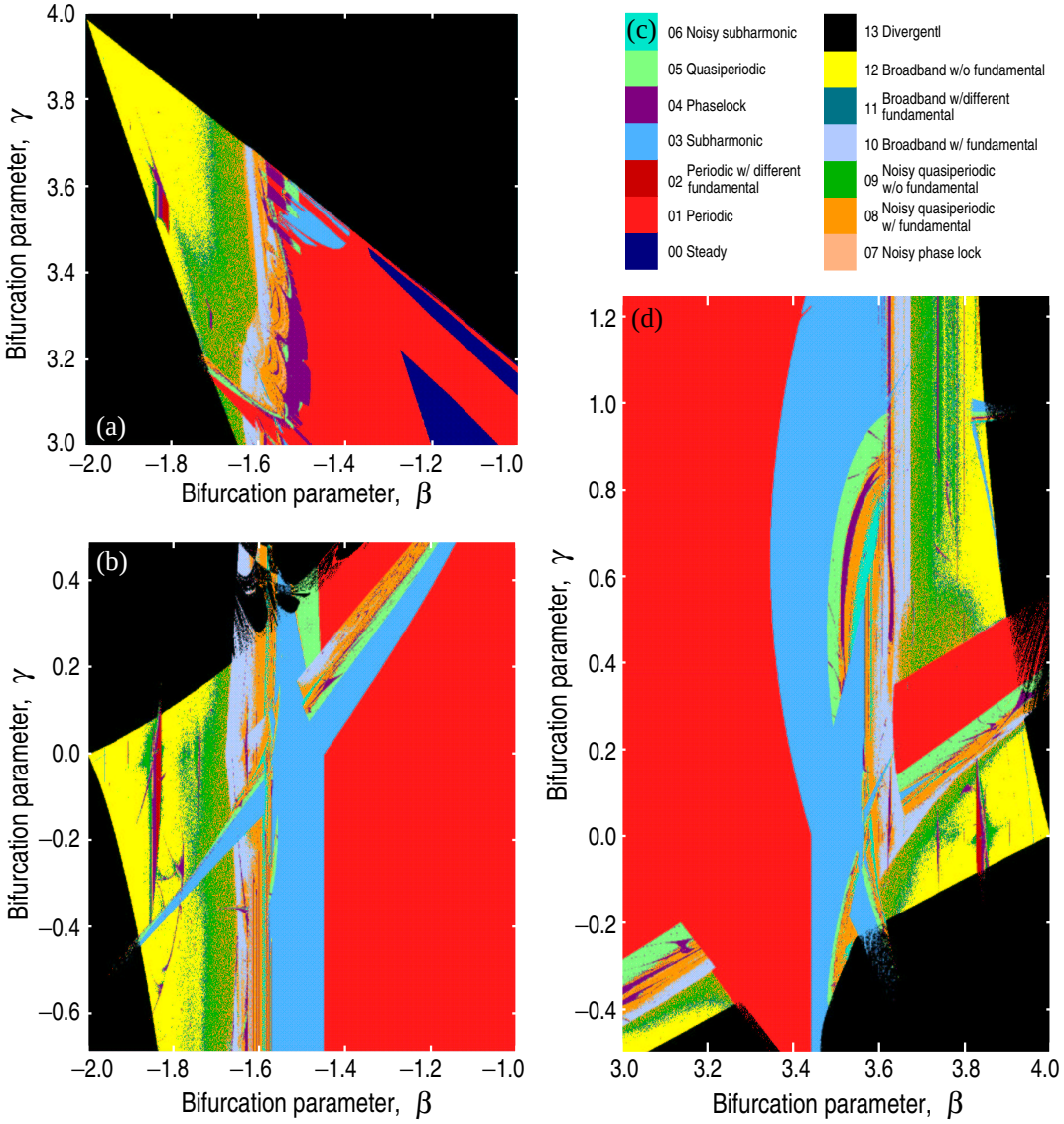

Figure 7: Details of 2-D PMNS regime map for $\beta_u = \beta_v$ and $\gamma_u = \gamma_v$.

The maps of Figure 7 provide details of the bifurcation sequences in the "interesting"

parameter regions, *i.e.*, at relatively low and high values of β. First, Figures 7(a) and (b) show details of the region $-2 \leq \beta \leq -1$, while Figure 7(d) is a blow up of the high β region ($3 \leq \beta \leq 4$). The bifurcation sequences described above are more easily identified along with many other transitions. Most notable are the multiple regions where transitions from periodicity directly to chaos are seen (*e.g.* between $\beta = 3.6$ and $\beta = 4.0$ for increasing γ) and the familiar windows of periodicity (*e.g.*, $\beta \approx 3.83$ and $\beta \approx -1.83$ for moderate values of γ) followed by subsequent bifurcations to chaos.

In addition, the low β, high γ region (part (a)) is seen to display a transition from periodic to phase-locked to quasiperiodic behavior in some parts. This is an interesting transition since ordinarily quasiperiodicity occurs before phaselocking and it could be argued that this is not phase-locking but merely period tripling occurring before a Hopf bifurcation to quasiperiodicity, though the dynamics of each are nearly identical.

4.2.3 Chaotic Regimes and Strange Attractors

It is of interest to look at these bifurcation sequences to chaos and their associated "strange attractors" in detail. First we denote the parameter regions which we have, to the best of our ability, verified to exhibit similar qualitative behavior throughout (though the details of the trajectories can be extremely contrasting). That is, for example, these regions might exhibit geometrically similar attractors for all of the parameter values within or might share a bifurcation sequence to chaos as one of the independent parameters is varied. Considering only the negative β range we will discuss the following three general regions displaying chaos: 1) moderate γ ($0.0 \lesssim \gamma \lesssim 1.0$) chaos, 2) high γ ($\gamma \geq 1.0$) chaos, and 3) low γ ($\gamma < 0.0$) chaos.

First we note that the moderate γ chaotic region is generally associated with the RTN transition to chaos, but the period doubling sequence is also seen (*e.g.* $\gamma = 0.0$). The transition scenario in this region can be characterized pictorially by making use of phase portraits. For those unfamiliar with this terminology a phase portrait is simply a plot of the time evolution of two (or more) dependent variables (in this case the two Fourier coefficients (a^n and b^n) of the 2-D PMNS equation) giving a picture of the behavior of the system in phase space. Figure 8 shows (for $\beta = -1.26$) the most common transition through

quasiperiodicity seen in this region. In part (a) we have an example phase portrait of period 4 quasiperiodic behavior found for $\gamma = 0.388$. This type of behavior is seen after successive pitchfork bifurcations to subharmonic (period 4) behavior followed by a Hopf bifurcation ($\gamma \approx 0.378$) to quasiperiodicity. The trajectory visits a different loop at each consecutive iteration. As the incommensurate frequency loses stability the loops grow in magnitude and approach one another (Figure 8(b) at $\gamma = 0.4149$). After the loops have crossed one another (*e.g.* Figure 8(c) at $\gamma = 0.423$) switching between loops occurs and the attractor becomes more complicated, but remains relatively non-noisy. Figure 8(d) shows the attractor (at $\gamma = 0.469$) just before encountering a reverse bifurcation to periodicity. Note how the quasiperiodic loops have crossed one another approximately along the $a = b$ axis and, also, how the edges of the attractor seem to be asymptotically approaching the unstable fixed points $a^n = 0$ and $b^n = 0$ before encountering the reverse bifurcation to periodicity.

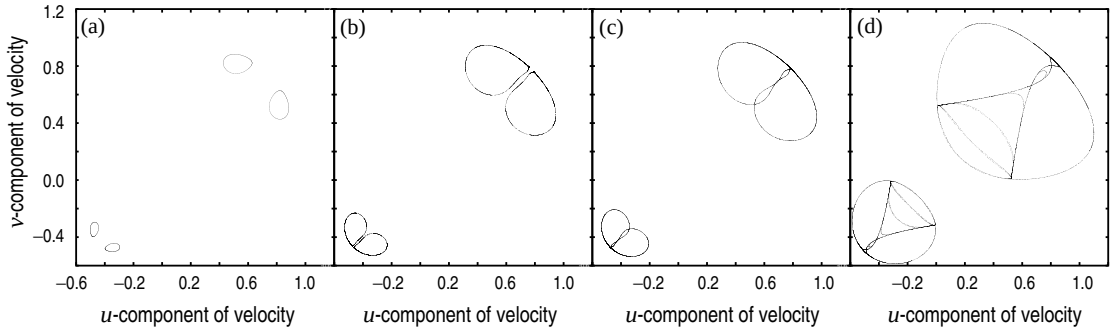

Figure 8: Phase portraits displaying the RTN transition to chaos through nonnoisy quasiperiodicity.

Another transition in this region is through noisy phaselocked behavior and occurs at lower values of β than the previous case. First we note that throughout any of the quasiperiodic regimes in this region frequent phase locking occurs, as can be seen by the many Arnol'd tongues of Figures 7(b) and (d). In Figure 9 we show an example of this type of transition for $\beta = -1.41$. Again the scenario begins with successive pitchfork bifurcations to subharmonic (period 4) behavior followed by a Hopf bifurcation ($\gamma \approx 0.176$) to quasiperiodicity. Soon thereafter the quasiperiodic loops begin to display individual complexity which is associated with the locking frequencies. For example Figure 9(a) shows such a complex quasiperiodic

attractor at $\gamma = 0.207$ along with the phase locked points seen at $\gamma = 0.208$, though the reader may need to zoom-in on the figure to note these phaselocked points. With further increase in γ (0.226) these frequencies isolate themselves and become noisy, as in Figure 9(b). Soon thereafter, as in Figure 9(c) at $\gamma = 0.228$, the noise begins to dominate and the locking frequencies are once again connected, but now through a strange attractor (though we have not performed a mathematical proof that this attractor is indeed strange, but is at least intermittently sensitive to initial conditions). Once the loops cross the trajectory becomes sufficiently complicated (Figure 9(d)) to be verifiably strange. This sequence of transitions to chaos is of special interest in that it has been observed in the fluid convection experiments of Gollub and Benson [71]

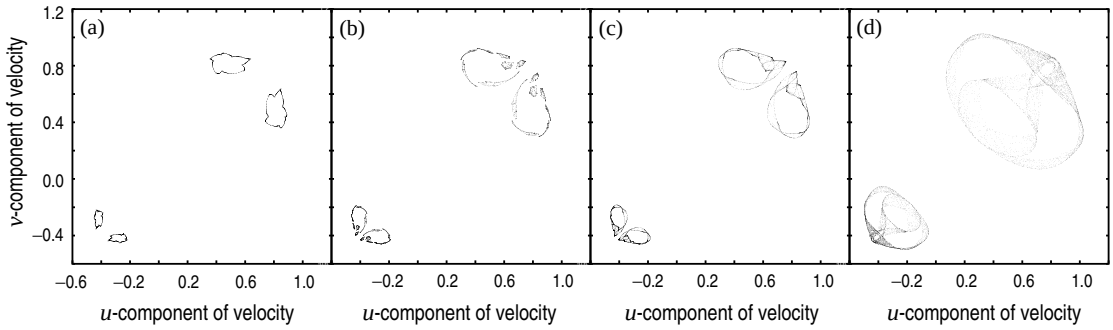

Figure 9: Phase portraits displaying the RTN transition to chaos through noisy phaselocked behavior.

Next we present two bifurcation patterns that produce similar strange attractors in the low γ region. Both display transitions similar to the noisy phase locked transition above though the details vary. In Figure 10 we present five phase plots at various values of β and γ. Part (a) shows a quasiperiodic trajectory that has gone through 3 pitchfork bifurcations before the Hopf bifurcation to quasiperiodicity. We would expect this trajectory to transition as one of the two above, but we see instead, as in part (b), that the Fourier coeffecients become perfectly correlated. This phenomena occurs over a large portion of the low γ region, centered around β values of -1.58. Further change in the bifurcation parameter values causes the return of a slightly altered quasiperiodic state (Figure 10(c)). This trajectory then undergoes a transition through noisy phaselocked behavior similar to that in Figure

9. Parts (d) and (e) are examples of a noisy quasiperiodic and a broadband without the fundamental frequency phaseplots in this transition. The effects of both the location of the original quasiperiodicities and locking frequencies along with the tendency for the dependent variables to correlate can be seen in these latter chaotic attractors.

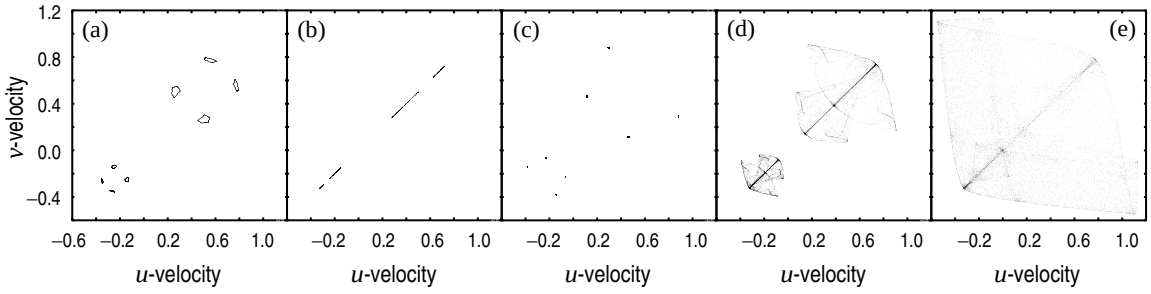

Figure 10: Phase portraits displaying the transition to broadband chaos through perfectly correlated variables; (a) $\beta = -1.577, \gamma = -0.317$, (b) $\beta = -1.578, \gamma = -0.318$, (c) $\beta = -1.626, \gamma = -0.42$, (d) $\beta = -1.63, \gamma = -0.43$, (e) $\beta = -1.68, \gamma = -0.48$,.

Figure 11 shows an alternate transition to nearly the same (geometrically) strange attractor. In general the majority of strange attractors in the moderate to low γ regions are of this size and shape. In part (a) we begin with the quasiperiodic phase plot corresponding to $\beta = -1.62$ and $\gamma = -0.08$. We then traverse parameter space in the positive γ direction. Again we encounter transition through noisy phase locked behavior and in Figure 11(b) we see an example of the resulting noisy quasiperiodic attractor at ($\gamma = -0.05$). With further increase in γ the dynamic noise soon dominates the quasiperiodicity and a broad band with fundamental frequency power spectrum is seen for the attractor of Figure 11(c) for $\gamma = 0.0$. An interesting phenomenon occurs with variation of β as in Figure 11(d) where $\beta = -1.67$ and $\gamma = 0.07$ when the trajectory jumps attractors. Lastly it is seen that with further variation in the parameters these two attractors combine to shape one similar to that of Figure 4.9, but without the strong tendency for the depedent variables to correlate (Figure 11(e) at $\beta = -1.67$ and $\gamma = 0.08$).

A few notes should be made regarding the above figures. First is the geometrical similarity between the strange attractors of Figures 8 and 9, corresponding to separate transitions to chaos. Second is the similarity of separate parts of the attractors reflected across the

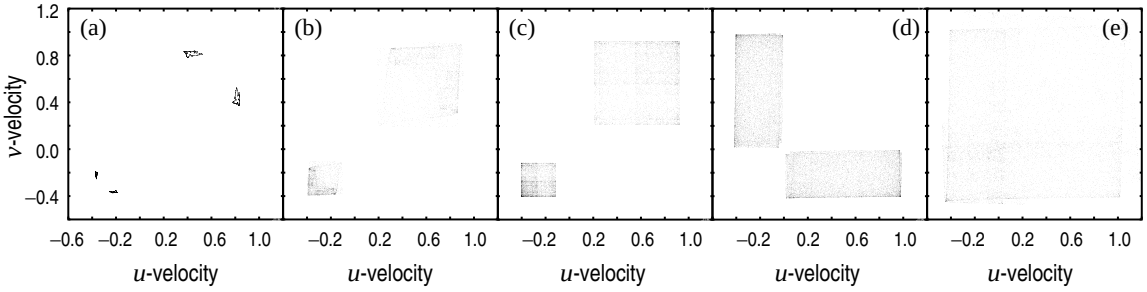

Figure 11: Phase portraits displaying the RTN transition to broadband chaos.

$a = -b$ axis and also the symmetry seen across the $a = b$ axis. Lastly, and probably most importantly, is the noticable effect that the type and shape of the quasiperiodicities and their phase locking frequencies have on the overall dynamics and geometry of the strange attractors with which they are associated.

We will omit such detailed description of the transitions to chaos for the positive β case and only present the phase plots (Figure 12) for a few of the unique strange attractors that we have found in this parameter space. One can find similarities in these attractors and those found for negative β and can, hopefully, draw conclusions concerning the bifurcation sequences that are implied by these attractors. The parameter values at which these attractors are seen are given in the figure caption.

Before we conclude our discussion on time series we would like to present a case that displays a type of self similarity in the time series during a period doubling cascade to chaos. In Figure 13(a) we present a time series (v-component) for the subharmonic (period 8192) case where we have used the bifurcation parameters $\beta = -1.569898$, $\gamma = -2.5$ and the default initial conditions. This time series is plotted with points instead of lines and for a larger range of iterations (100000) than those previously. These calculations were performed in quadruple precision (128-bit arithmetic) to improve their accuracy. At first it might appear that this time series is quasiperiodic or noisy subharmonic but instead numerical experiments that verify it develops from a periodic cascade and indeed repeats every 8192 iterations. Upon further inspection, as in Figure 13(b) and (c), this time series is seen to display the self-similarity common to chaotic systems. After the accumulation point of these period doublings is surpassed noise enters the system (*e.g.* at $\beta = -1.569899$,

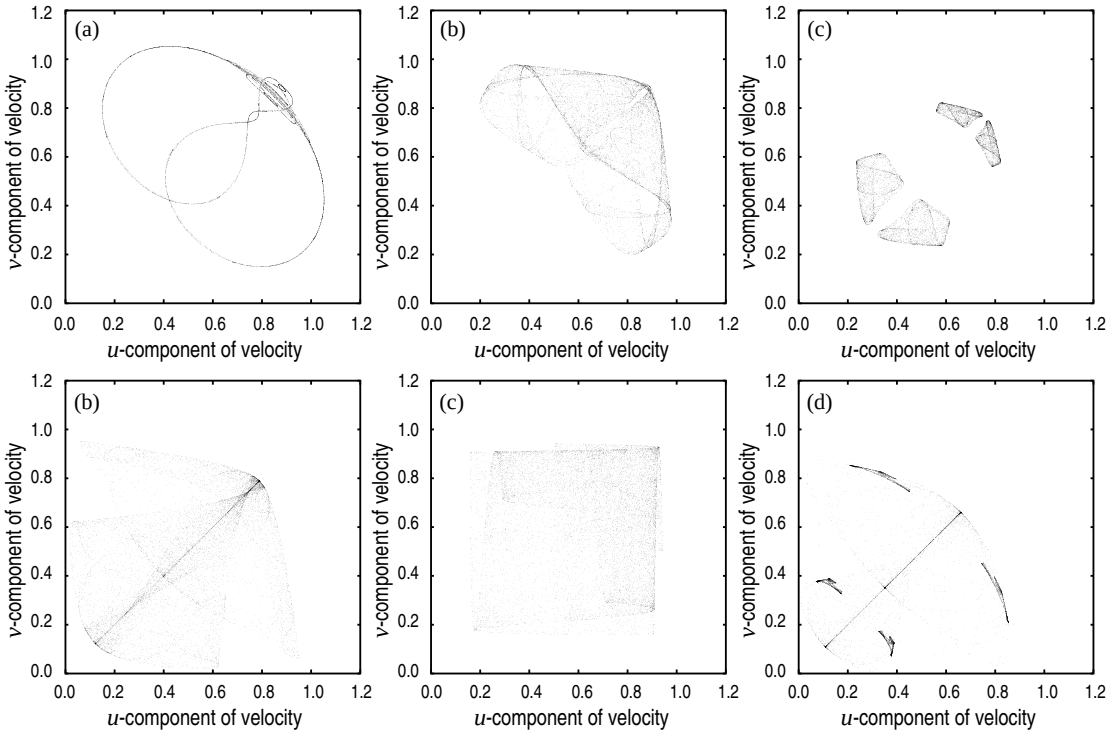

Figure 12: Various strange attractors: (a) $\beta = 2.5$, $\gamma = -0.745$; (b) $\beta = 3.1$, $\gamma = -0.4$; (c) $\beta = 3.57$, $\gamma = 0.6$; (d) $\beta = 3.83$, $\gamma = 0.6$; (e) $\beta = 3.8$, $\gamma = 0.09$; (f) $\beta = 3.829$, $\gamma = 1.71783$.

$\gamma = -2.5$) which causes the intermittent time series of Figure 13(d) which is plotted with the same magnification as that of part (c). This noise has caused the "mixing" of the highest harmonics captured here and causes a type of reverse cascade where the noise continues to grow. In fact this noise grows quite fast and when $\beta = -1.579$ the trajectory has already become a noisy period-4 subharmonic signal comprised of the four most definite "bands" of Figure 13(a) (note that their are two "bands" in the top half and two in the lower half), merging successive harmonics so that eventually all (or most in the subharmonic case) of the bands are merged with a high level of noise. We note that the addition of noise must necessarily occur before the accumulation point is reached (due to restrictions on the preciseness of calculations caused by machine epsilon, *i.e.*, the maximum number of digits to the right of the decimal place that a computer can store and perform calculations on), though it is believed, as propounded by Dalling and Goggin [113], that chaos seen in finite precision calculations is representative of the true dynamics of the system. An open question

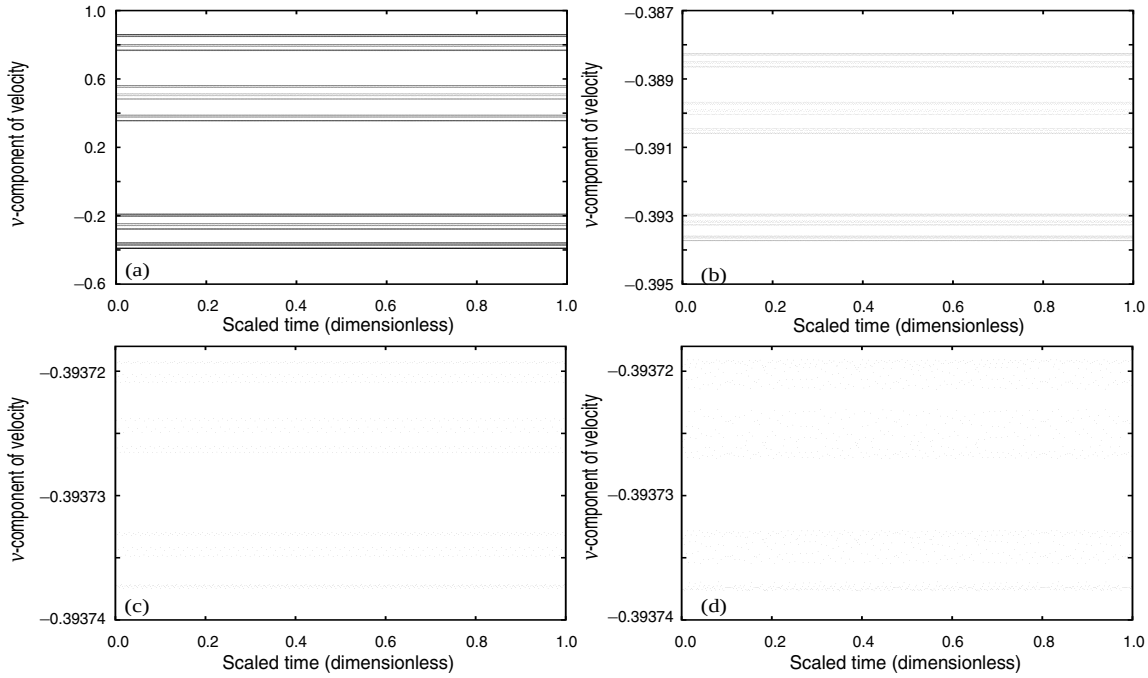

Figure 13: Time series displaying transition to chaos due to period-doubling and noise amplification.

is whether the noisy phase locks that we have seen to be very important in the dynamics of the strange attractors above "bifurcate" in this manner, *i.e.* through an ever increasing number of phase-locked points until the introduction of noise which then amplifies to connect the individuals. We expect that this is the case but the difficulty of finding such a sequence lies in the "nested" nature of quasiperiodicity and phase locks, *i.e.*, the sequence does not have to be "continuous" as it was in the period-doubling cascade as phase-locks are likely to be interrupted by quasiperiodicities and vice-versa in ever diminishing parameter spaces. A 1-D bifurcation diagram performed at very high precision is one possible way that this sequence could be observed though we have not performed such a study.

4.2.4 Effects of Initial Conditions

Thus far we have only looked at the behavior of the 2-D PMNS equations for an isolated set of intitial conditions, viz. $(a^0 = 0.4, b^0 = 0.61)$. It is well known that multiple attractors

can exist for multidimensional dynamical systems and the dynamics of such dependence is investigated in this section. For more on this aspect of the 2-D PMNS see [109]. We begin this study by investigating the outcome of allowing that $a^0 = b^0$. From Eqns. (39) we see that when we make the above substitution while restricting the bifurcation parameters as we are here, such that $\beta_u = \beta_v$ and $\gamma_u = \gamma_v$, we are left with identical equations now of the form:

$$u^{(n+1)} = \beta u^{(n)} \left(1 - u^{(n)}\right) - \gamma u^{(n)} u^{(n)}.$$

These equations act much like the logistic map as they are completely independent of one another, and each only deviates from the logistic map by a factor of γ on the quadratic term. A similar simplification can be made under the condition that $a^0 = 1 - b^0$. By making this substitution into Eqns. (39) we find that the system equations reduce to

$$u^{(n+1)} = \beta u^{(n)} \left(1 - u^{(n)}\right) - \gamma u^{(n)} (1 - u^{(n)}),$$

which is another generalization of the logistic map where now both the linear and quadratic terms are a factor of γ removed from the usual logistic map case.

From these analyses we can draw the conclusion that special initial conditions will not, in general, behave in qualitatively the same manner as will the 2-D PMNS equations without special initial conditions. This fact is displayed in the following movies embedded in Figure 14. Each of the three movies, Movie 1 (1.3 Megabytes), Movie 2 (1.3 Mb), and Movie 3 (1.2 Mb), contain a sequential series of regime maps, as that displayed in Figure 6, where each individual map was constructed at a unique set of initial condition values. The first movie (Figure 14(a)) contains regime maps that all share the same initial condition $b^0 = 0.2$ but a^0 varies as the movie progresses. The step size of a^0 that corresponds to each slide in the movie is $\Delta a^0 = 0.1$, starting from $a^0 = 0.1$ and progressing to $a^0 = 1.0$. That is, the first regime map corresponds to using $a^0 = 0.1$ and $b^0 = 0.2$, the second to $a^0 = 0.2$ and $b^0 = 0.2$ and so on. The second and third movies are variations upon the first as they use $b^0 = 0.5$ and $b^0 = 0.8$, respectively. The reader can view the movies by moving the pointer over the part of the figure corresponding to the movie that they wish to view and then using the left mouse button. This will open a new movie window. To return to the text press escape. If this does

not work try clicking in the text and then back on the movie and pressing escape once again. All of the regime maps shown here correspond to the parameter ranges $-2.0 \leq \beta \leq 4.0$ and $-3.1 \leq \gamma \leq 3.6$ and consist of 512×512 evenly spaced grid points in those directions.

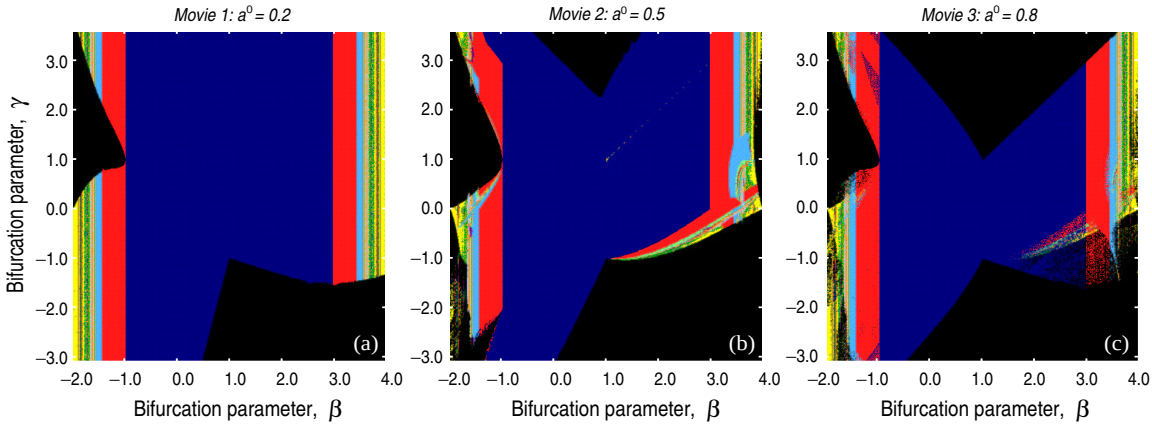

Figure 14: Movies displaying effects of alternate initial conditions on regime maps.

From the preceding movies we can make a number of generalizations about the effects of initial conditions. In particular it is noticeable that, as the previous analysis indicated, the choice of symmetric initial conditions, *e.g.* $a^0 = b^0$ or $a^0 = 1 - b^0$, produces regime maps that are much different than those seen for all other sets of initial conditions and for this reason should be avoided in any future studies aimed at gathering knowledge on the generic behavior of the PMNS equations. Another thing to notice is the effect of the initial conditions on the size of the area of parameter space that produces nonsteady and nondivergent behavior. It is easily seen by comparing, for example, Movie 1 and Movie 3, that higher valued initial conditions increase the area of divergence significantly, with high γ value stable behavior disappearing as the initial conditions increase. But even for the highest combination of initial conditions shown here ($a^0 = 0.9, b^0 = 0.8$) there still remains a significant area of parameter space that looks "interesting" and could be useful in turbulence modeling. Aside from this effect, it seems that the specific choice of the initial conditions does not greatly alter the overall shape of the regime maps. Instead initial conditions tend to shape the details of the behavior of individual trajectories, *e.g.*, by causing a trajectory to bifurcate at a different value of bifurcation parameter. One exception is the significant

region for negative β and γ that appears to produce a RTN (quasiperiodic) transition to chaos when higher valued initial conditions are used (see, *e.g.*, Movie 3,).

Another method for studying the effects of initial conditions is through the visualization of the basins of attraction for a particular set of bifurcation parameter values. A basin of attraction is the set of all initial conditions that asymptote to a specific type of behavior or attractor, though we use the former here. That is, an initial condition grid can be treated in the same manner as was the bifurcation paramater grid in the case of the regime map. It is of interest to do this from a modeling standpoint because it might be useful to know of trends in such basins that could possibly be utilized in the choosing of initial conditions to be used in the turbulence model, since there is no precedent for doing this. This was accomplished by dividing the square of continuous initial conditions corresponding to $a^0 \in [-1, 2]$ and $b^0 \in [-1, 2]$ into an equally spaced grid measuring 512×512 grid points. The choices of basins of attraction that we wish to study is somewhat arbitrary as we have studied many hundreds that produce interesting looking basins, though these were decided to be most relevant to what we are trying to do here.

We continue the trend of investigating behaviors for $\beta < 0$. We will look at three sets of basin pictures. The first basins shown are for relatively low values of β ($-1.628 \leq \beta \leq -1.57$) and high values of γ ($3.394 \leq \gamma \leq 3.8$). The four basins of Figure 15 are presented in order of increasing complexity. Part (a) shows the basins of attraction for the parameter values $\beta = -1.59$ and $\gamma = 3.395$. Here the x-axis corresponds to values of a^0 in the range $[-1 : 2]$ and the y-axis values of b^0 in $[-1 : 2]$. The color code that we use here is the same as that used for the previously discussed regime maps (see Figure 6). In addition to plotting the basins of attraction we have included the phase plots (b^n versus a^n) for the attractors associated with these basins in each case, though the reader will need to zoom-in considerably to distinguish their details. For example in part (a) we have a combination of quasiperiodic (green) and phase locked (purple) basins. It has been found that there are actually two (symmetric) quasiperiodic attractors which have been plotted in white and black dots, respectively. In addition phase locking occurs, and the attractor becomes the 6 phase points (plotted in black) within the largest basins of phase locked behavior. It is quite interesting that we have only found 1 phase locked attractor (though many initial conditions have been tested)

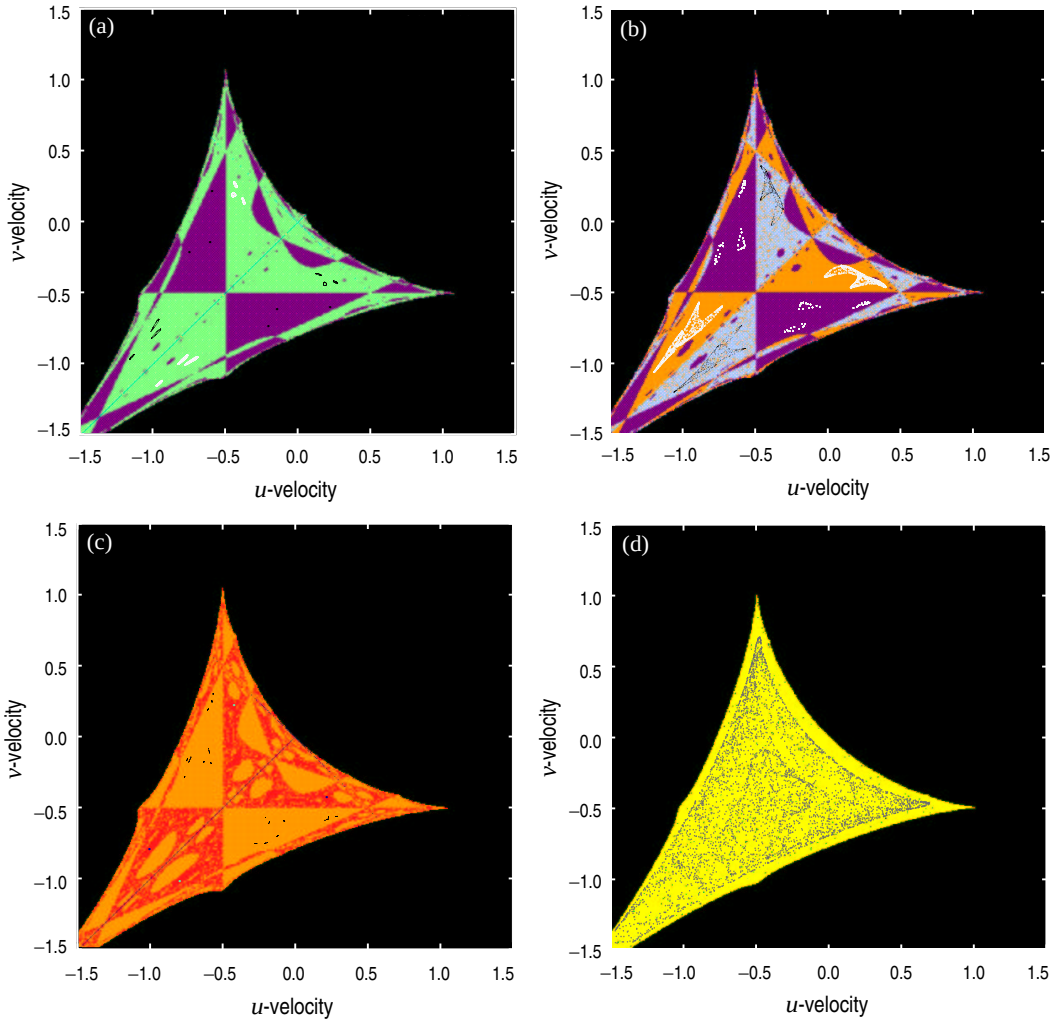

Figure 15: Basins of attraction for cases in the high γ chaotic regime.

and that this attractor lies approximately halfway between each corresponding loop on the separate quasiperiodic attractors. This type of phenomenon clearly plays a very important role in the overall dynamics of the eventual chaotic attractor.

In part (b) we present the same type of plots, the basins of attraction and associated attractors, for slightly modified bifurcation parameter values ($\beta = -1.609$ and $\gamma = 3.394$). At first the basins of attraction look more interesting than in the previous case, as more than two basins are identified by the power spectral identification algorithm. Indeed, though, when we plot the attractors for initial conditions in these basins we find the same total number of attractors as in the previous case. First we notice that the phase locked frequencies

have become noisy (as have the quasiperiodicities), typical for the noisy phase lock transition to chaos described previously. Second we note that we find two symmetric and seemingly identical (though reversed) attractors corresponding to the noisy quasiperiodicities, irrespective of whether or not they belong to the orange basin (noisy quasiperiodicity) or the light blue basin (noisy subharmonic with the fundamental frequency). This discrepancy is caused by the difficulty, mentioned previously in the discussion of power spectra, in distinguishing noisy attractors when the noise grows to approximately the same magnitude as the primary spectral peaks (note how the u-components of one of the attractors have grown very close together in approaching the $a^n = 0$ axis). In fact it would be difficult for the human eye to appropriately classify the power spectra for the two noisy quasiperiodic attractors seen in Figure 15(b). Next we present the basins of attraction and attractors after further variation in the bifurcation parameter values ($\beta = -1.628$ and $\gamma = 3.62$). Upon inspection of part(c) we find that there are three attractors seen, 2 periodic and 1 noisy quasiperiodic. We distinguish the two periodic attractors by plotting their phase points in different shades of blue. The noisy quasiperiodic trajectories are plotted in black. Finally, in part(d), we present the basins and attractor (grey) found for the bifurcation parameters $\beta = -1.8$ and $\gamma = 3.8$. Here the similarity in the shape of the chaotic attractor associated with the high γ region and the shape of the basins of attraction for this region is clearly seen.

Next we look at the moderate to low γ range. In Figure 16 we present the basins of attraction and attractors for four sets of parameter values: $\beta = -1.26, \gamma = 0.388$ in part (a), $\beta = -1.41, \gamma = 0.208$ in part (b), $\beta = -1.626, \gamma = -0.42$ in part (c), and $\beta = -1.793, \gamma = -0.264$ in part (d). The first two parts of the figure are to be noted for their geometric similarities with respect to their basins of attraction and w.r.t. the quasiperiodic attractor of part (a) and the phase locked attractor of part (b). As the bifurcation sequence continues the region of nondivergence diminishes and the level of noise grows (part(c)). Lastly, in part (d) we see that even though the attractor is sufficiently within the chaotic regime there still exists a phase locked basin of attraction simultaneously.

An obvious attribute of each of the basins of attraction that we have presented thus far, excluding Figure 15(b) and, perhaps, Figures 16(c) and 16(d), is the symmetry of basins observable with respect to the $x = y$ axis. Of course this axis corresponds to $a^0 = b^0$ and

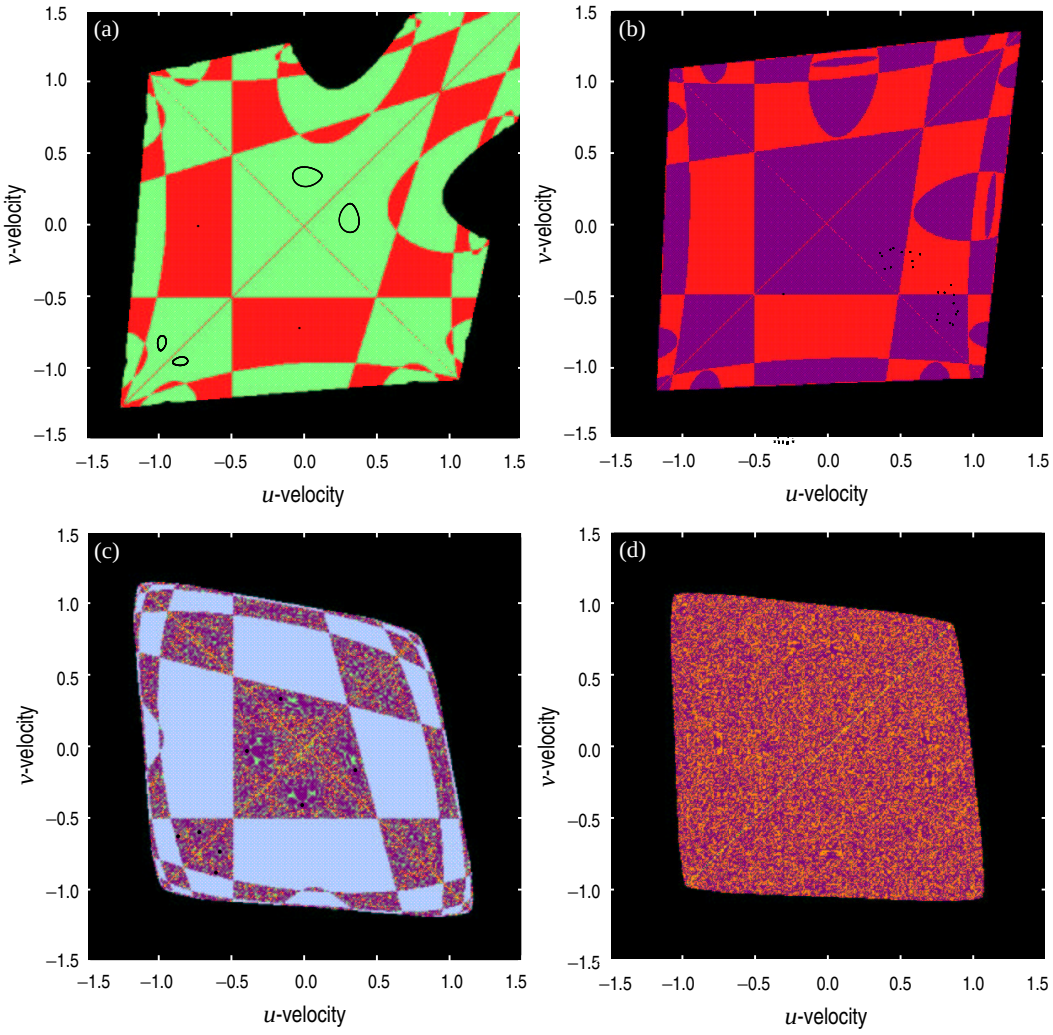

Figure 16: Basins of attraction for cases in the moderate to low γ chaotic regimes.

the following analysis will shed light on the observed symmetries. Consider the following generalized initial condition sets that are symmetric with respect to the $a^0 = b^0$ axis:

$$a_1^0 = b_2^0, \tag{40a}$$

$$b_1^0 = a_2^0. \tag{40b}$$

Here subscripts correspond to the separate initial condition sets, and superscripts are the usual iteration counter. By substitution of Eqns. (40) into Eqns. (39), along with the bifurcation parameter restrictions, $\beta_u = \beta_v$ and $\gamma_u = \gamma_v$, we can derive the following result for

the first iterations of the separate initial conditions:

$$a_1^1 = \beta a_1^0 \left(1 - a_1^0\right) - \gamma a_1^0 b_1^{(n)},$$

$$b_1^1 = \beta b_1^0 \left(1 - b_1^0\right) - \gamma a_1^0 b_1^{(n)},$$

and

$$a_2^1 = \beta b_1^0 \left(1 - b_1^0\right) - \gamma a_1^0 b_1^{(n)} = b_1^1,$$

$$b_2^1 = \beta a_1^0 \left(1 - a_1^0\right) - \gamma a_1^0 b_1^{(n)} = a_1^1.$$

We see, then, that the symmetric condition $a_1 = b_2$ and $b_1 = a_2$ will also hold for all future iterations independent of β and γ. This indicates that symmetry is *necessary* for all coupled bifurcation parameter values, and, in fact, the u-component of the trajectory found for one set of initial conditions will behave identically to (neglecting variations due to round off error) the v-component of the trajectory corresponding to the symmetric initial condition, and vice versa. This interesting aspect of the 2-D PMNS equations (with coupled bifurcation parameters) is the reason for the multiple symmetric attractors, along with the symmetric basins, displayed in the above figures. We comment that is expected, due to the symmetries of the N.-S. equations, that similar symmetry could be seen in fluid flows if the initial conditions could be thus specified.

Finally we present some of the most interesting basins plots that we have found. The plots of Figure 17 correspond to the following bifurcation parameter values: $\beta = -1.5698, \gamma = -2.5$ in part (a), $\beta = -1.57, \gamma = -2.5$ in part (b), $\beta = -1.6016, \gamma = 0.4563$ in part (c), and $\beta = -1.832, \gamma = -1.03$ in part (d). We note that the first two come from the region associated with the self similar time series of Figure 13 discussed previously. The basins of part (c) live in the moderate γ region very near the divergent region for the initial conditions used in the original regime map (Figure 6). Last, in part (d), is a basin that lives in the "island" region at low values of both β and γ, islands being terminology for small sets of parameter values that lead to stable behavior surrounded by parameter values that cause divergence. Again in Figure 17(b), as in Figure 15(c), we see that the psd analyzer indicates behavior that is not symmetric about $a^n = b^n$ axis. The reason for this is that the

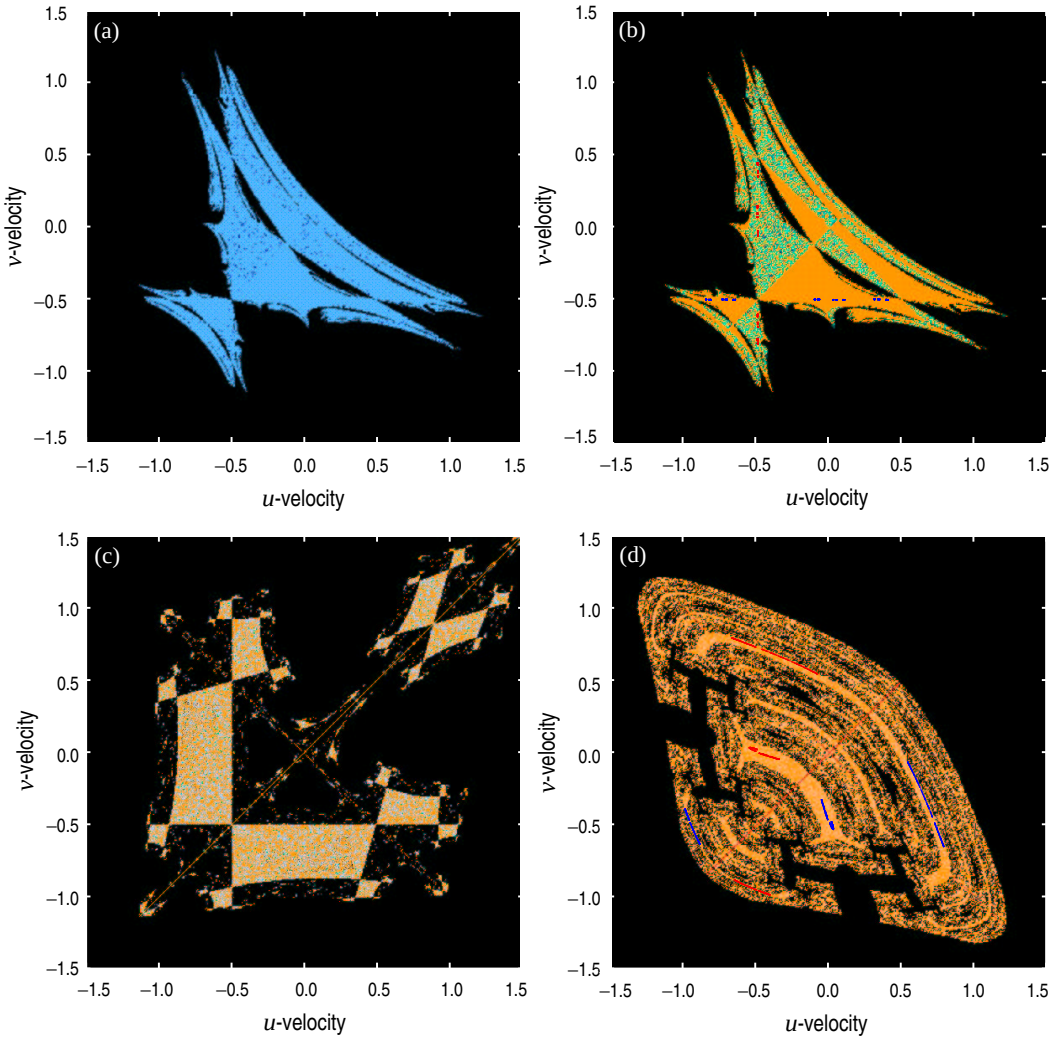

Figure 17: Basins of attraction for interesting cases.

psd analyzer, in these cases, has been implemented for the u-component Fourier coefficient, which due to the details of the dynamics of the attractor, produces a slightly different psd than that of the symmetric initial conditions, but is not an example of a violation of the well known theorem [26] that any of the n independent variables in a dynamical system that contribute to the geometry of an n-dimensional attractor can be used to assess that geometry, *i.e.* behave alike.

We neglect to present the basins of attraction for $\beta > 0$ as these cases have been covered in [109], and the behavior of the basins is similar to those presented for $\beta < 0$, except restricted to $[a^0, b^0] \in (0, 1) \times (0, 1)$, analagous to the discussion of attractors for both

cases in the previous section. The most important finding of this section has been the symmetry in attractors and basins of attraction for symmetric conditions. Previously we noted that quasiperiodic loops often appear to approach one another about the $a^0 = b^0$ axis and aymptotically expand towards the unstable fixed points $a^0 = 0$ and $b^0 = 0$. These dynamics are likely linked to the discoveries in this section concerning symmetric initial conditions but the details of this connection have not been worked out.

4.3 Decoupling Bifurcation Parameters

As we have noted in Section 4.2, it is not generally appropriate, in the context of the physical interpretation of the bifurcation parameters, to set $\beta_1 = \beta_2$ and $\gamma_1 = \gamma_2$, and in addition this condition leads to specialized behavior as was seen in the previous section. Thus we would gain a better understanding of the PMNS equation by decoupling of these bifurcation parameters. Still, the simplification of retaining one of the equality constraints makes such a study simpler and more intuitive. Therefore, in this section, we study the behavior of the system while employing the bifurcation parameter constraints $\beta_u \neq \beta_v$, $\gamma_u = \gamma_v$ and $\beta_u = \beta_v$, $\gamma_u \neq \gamma_v$. It is also a straightforward expectation, considering the previous findings concerning symmetric attractors found when applying both constraints, that the 2-D PMNS equations will produce quite different dynamics, though qualitatively the behaviors may remain consistent. For further results concerning the uncoupling of bifurcation parameters see McDonough *et al.* [114]

4.3.1 $\beta_u \neq \beta_v$, $\gamma_u = \gamma_v$

First, to get an overall idea of the effects of increasing the dimension of the parameter space, we shall present results from numerical experiments allowing $\beta_1 \neq \beta_2$ with $\gamma_1 = \gamma_2$. This corresponds to permitting the modeling of different wavenumbers, or different cell Reynolds numbers, in the component velocities in each direction. The calculations were made using a slightly altered set of initial conditions ($a_0 = 0.55$, $b_0 = 0.51$) than from the previous section.

In Figure 18 we present β_u versus β_v regime maps at eight $\gamma_u = \gamma_v$ values (parts (b)–(i)). We show these in a static plot for the convenience it allows for future referencing; but,

for more details on the evolution of this regime map as the value of the γs is varied, the reader can follow the figure link (as before) to view a movie (Movie 4) showing this regime

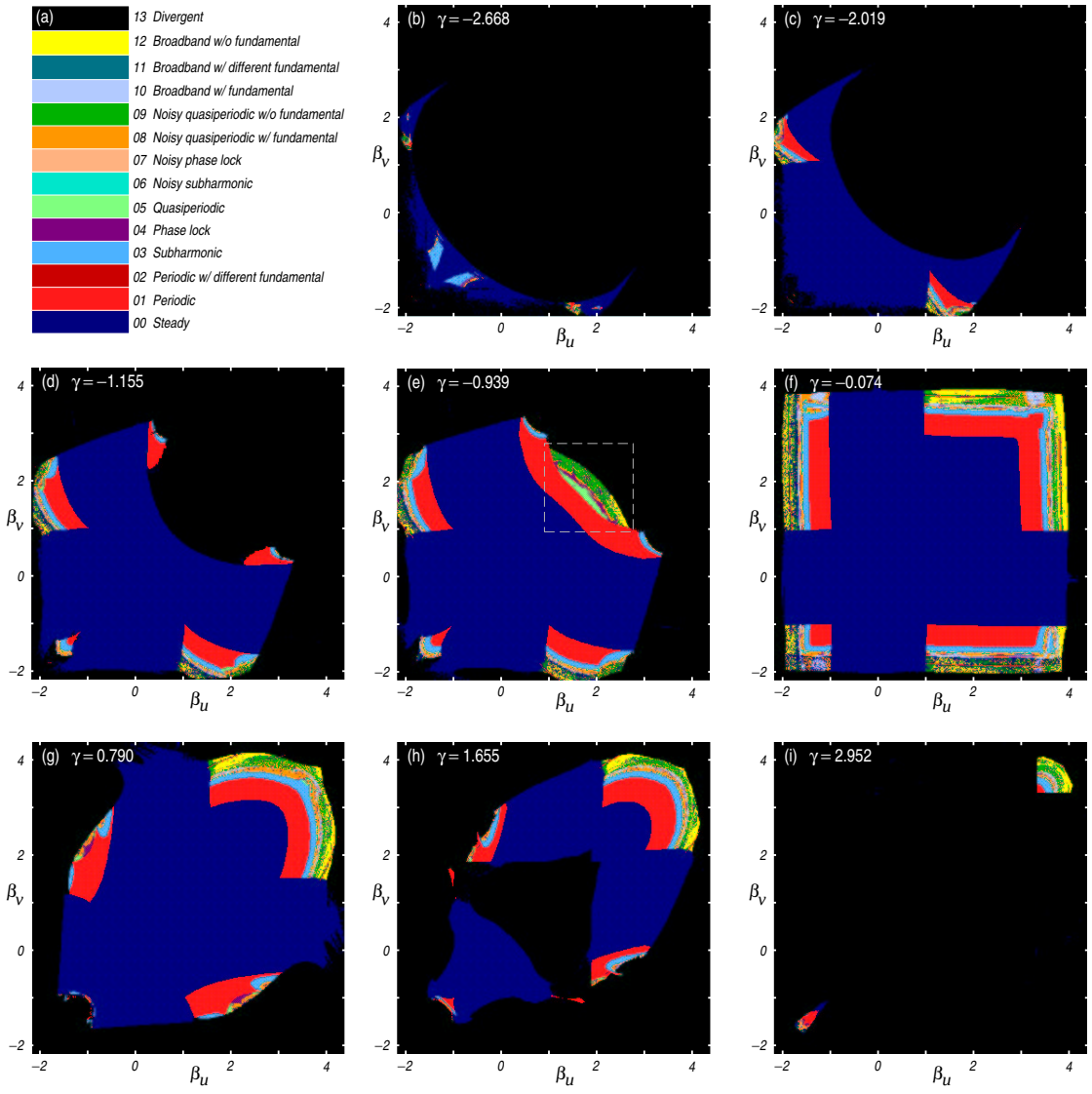

Figure 18: Bifurcation map for $\gamma_u = \gamma_v$, βs vary on both axes from -2.2 to 4.4. The animation (665 KB) corresponds to allowing $\gamma_u = \gamma_v$ to vary from -3.1 to 3.6 in increments of $\Delta\gamma \approx 0.216$.

map at 32 values of $\gamma_u = \gamma_v$ increasing in magnitude from -3.1 to 3.6 in equal increments of approximately 0.2163. The spacing between grid points in both coordinate directions is $\Delta\beta \simeq 0.0088$, and the limits are $2.2 \leq \beta \leq 4.4$. This movie is slightly different than those presented in section 4.2 as we now project the slices onto their respective planes instead of

viewing the slices in a volume.

At highly negative γs there exists a large region of divergence surrounding a relatively small region of nontrivial behavior (see, *e.g.*, part (b) at $\gamma = -2.668$). As γ is increased (becomes less negative) a gradual transition from divergence to steady behavior is seen at moderate values of β while the interesting regions of nonsteady, nondivergent behavior grow in size (see, *e.g.*, part (c) at $\gamma = -2.019$ and part (d) at $\gamma = -1.155$). When the value of the γs reaches -1 we see the addition of an arc of interesting behavior centered about the $\beta_u = \beta_v$ axis which we have outlined in part (e). Further increase in the values of the γs causes a transition to a largely steady regime surrounded by a "shell" of more interesting behavior (see, *e.g.*, part (f)). The existence of sharp-edged transitions that remain fairly constant in their parameter space locations (independent of the value of γ) suggests the existence of threshold values of β that determine the initiation of non-steady behavior whenever they are exceeded by the value of either β_u or β_v, with few notable exceptions. Once such exception to note is the existence of a range of βs, $-1 < \beta_i < 1$, that very rarely produce behavior that is either nonsteady or nondivergent, independent of the complementary β and γ values.

As γ is increased further the area of divergent trajectories begins to increase as the flow becomes excited by higher velocity gradients, becoming increasingly sensitive to the directional Re numbers (β values). By the time γ reaches a value of 1.655 (part (h)) an interesting phenomena is seen as a region of divergence has appeared surrounded by non-divergence. Effects of this type clearly impose modeling difficulties but can probably be overcome by actively monitoring the evolution of the DDS to prevent its divergence, thus maintaining numerical stability during a simulation. We could also hope that the correct mappings from physics to bifurcation parameters are found from laboratory experiments or direct numerical simulation and that such mappings prevent the model bifurcation parameters from attaining values within this region due to their (possibly) unphysical nature. Furthermore, from the standpoint of SGS modeling, this region of divergence is primarily interior to a basically uninteresting region of steady behavior, where the model would be turned off most of the time. Continuing to increase γ causes further divergence until only a small region of nondivergence is observable at $\gamma = 2.952$ (part (i)). At γ values greater than this the regions of nondivergence continuously disappear and are completely gone by

$\gamma = 3.6$.

It is of interest to show a detailed regime map from a location within the regime maps of Figure 18 to demonstrate the complicated geometry and entangled nature of the basins of behavior within those regime maps. We remark that the complex qualitative nature of the following figures is quite general for the 2-D PMNS equations and not simply an aspect of the particular location chosen to detail here. Figure 19 depicts the details of the arc-shaped region that appears at moderate γs centered around the $\beta_1 = \beta_2$ axis as seen in Figure 18(e), for example.

We have performed the calculations used in constructing Figures 19 (b,c) at slightly different parameter values than those used in constructing Figure 18(e). Here we have employed $\gamma = -1.0$ while the bifurcation parameters β_u and β_v vary in successively smaller ranges as indicated. From part (b) one can see that this portion of the regime map displays the RTN transition to chaos previously described. In part (c) we present a magnification of a section of Figure 19(b). Here the distance between parameter points has been further decreased from $\Delta\beta \simeq 0.00065$ to $\Delta\beta \simeq 0.000325$, and the fractal nature of the region boundaries has become more evident. With reference to Figure 6 we note that this region corresponds to a γ point within the "tail" region from $1 \leq \beta \leq 3$ that has previously been studied in detail in [102].

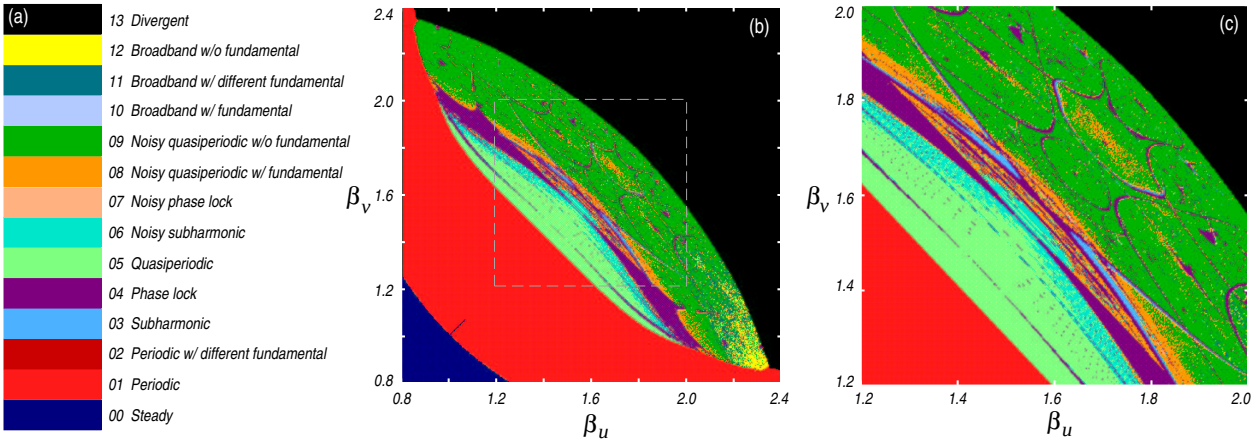

Figure 19: Details of $\beta_u - \beta_v$ regime map displaying RTN transition.

Indeed we find that the dynamics remain consistent with that presented in Figures 8

and 9, but a notable difference is seen. Initially (after a Hopf bifurcation) there are two quasiperiodic loops (Figure 20(a) at $\beta_u = 1.78$ and $\beta_v = 1.22$), and phase locking occurs to a period 72 trajectory which then experiences a reverse cascade to the phase locked trajectory of Figure 20(b) at $\beta_u = 1.78$ and $\beta_v = 1.27$. But in this instance the trajectory immediately transitions to the noisy quasiperiodic attractor of Figure 20(c) at $\beta_u = 1.78$ and $\beta_v = 1.32$, instead of going through a noisy phase locked regime as does the similar attractor of Figure 9 or remaining nonnoisy until the loops cross as in Figure 8. The inset of part (c) details the

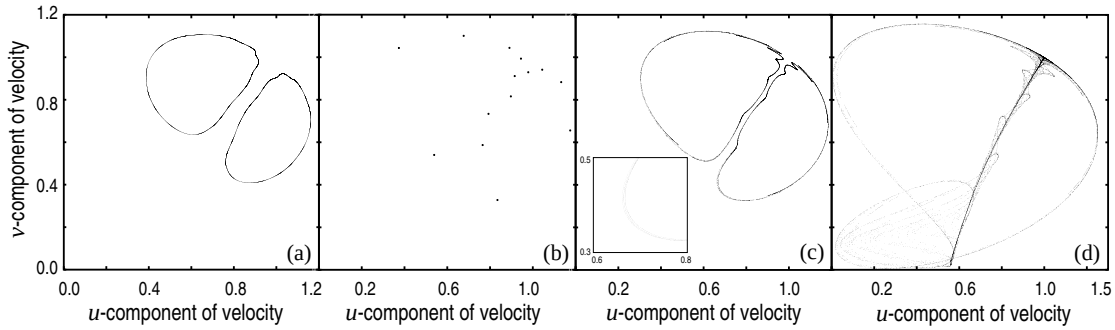

Figure 20: Phase portrait displaying the RTN transition to chaos through noisy quasiperiodicity.

"rings" that are seen for this case. Eventually the two separated loops become entangled and lead to, for example, the strange attractor seen in part (d) at $\beta_u = 2.22$ and $\beta_v = 1.2$. We associate this behavior more with the behavior seen previously in Figure 8 than that in Figure 9 and contribute the added complexity to the allowance that $\beta_u \neq \beta_v$. We would prefer to go into this amount of detail for trajectories in all of the regions of interest, but for brevity we move on to briefly discuss the case where $\beta_u = \beta_v$ with $\gamma_u \neq \gamma_v$.

4.2.2 $\beta_u = \beta_v$, $\gamma_u \neq \gamma_v$

We have indicated thus far that the values of γ_u and γ_v in Eqns. (39) are directly related to the strain rates, u_y and v_x, and presented demonstrations of the dependence of the β_u versus β_v regime maps on values of $\gamma_u = \gamma_v$ ranging from -3.1 to 3.6. Next we show the strict dependence of the γ_u versus γ_v regime maps on a range of $\beta_u = \beta_v$ values from -2.2 to 4.4. This might be considered a more realistic simplification than the last since the

directional Reynolds numbers, which they are most closely associated with, are more likely to be approximately equal, though we note that the directional cell Reynolds numbers that will be used are less likely to be approximately equal than would the large scale directional Reynolds numbers since they contain normal strain rate information.

In presenting the results we follow the same procedure as in the previous case. In Figures 21(b)–(i) we present a static plot of γ_u versus γ_v regime maps at eight $\beta_u = \beta_v$ values. Again, for a more continuous representation of the changes in this regime map as the value of the βs is varied, the reader can click on the figure link to view a movie (Movie 5) that displays the evolution of this regime map at 32 values of $\beta_u = \beta_v$, increasing in magnitude from -2.2 to 4.4 in equal increments of approximately 0.2129. The spacing between grid points in both γ directions is $\Delta\gamma \simeq 0.0088$. The initial conditions used here are the same as in the previous case, *viz.*, $a_0 = 0.55$ and $b_0 = 0.51$.

We can most easily discuss these changes if we describe the evolution of the regime map as we move on the β axis in both directions away from $\beta = 0$. As in the previous section we again find that for $-1 < \beta < 1$ there exist nearly exclusively steady and divergent behaviors at all values of γ_u and γ_v. A typical $\gamma_u - \gamma_v$ regime map for this type of behavior is given in Figure 21(d) corresponding to bifurcation values of $\beta_u = \beta_v = -0.710$. In addition there appears to be only nominally small regions of interesting behavior until after the period-doubling cascades to chaos have finished at $\beta \approx -1.57$ and $\beta \approx 3.57$, excluding small parameter regions corresponding to the thin tails of RTN transition behavior seen in and noted for the original regime map (Figure 6). Examples of $\gamma_u - \gamma_v$ regime maps within this largely uninteresting region can observed in Figure 21(e) using $\beta = -1.348$, in Figure 21(f) for $\beta = 3.123$ and also for $\beta = 3.548$ in Figure 21(g). Typical examples of $\gamma_u - \gamma_v$ regime maps after further increases in the magnitudes of the βs are shown in parts (b) and (h) of Figure 21. Finally, with further increase in the magnitude of the βs, the transition to broadband behavior occurs before the trajectories diverge (see, *e.g.*, part (i)).

Another aspect of Figure 21 to note is the evolution of the shape of the $\gamma_u - \gamma_v$ parameter space that produces nondivergence. First we note the similarity between Figure 21(b) and the original regime map for low values of β ($\beta \leq -1$). That is, one can draw an analogy between the original regime map displaying two regions of interesting behavior, one at high

values of γ and one for moderate to low values of γ, and the dynamics seen here where there exists the same type of separation. Another aspect of the evolution of the shape to note is that negative β chaos is ordinarily seen over the bottom left half of the $\gamma_u - \gamma_v$ space we have plotted here and positive β chaos is seen on the top right hand region of $\gamma_u - \gamma_v$ space (excluding the previous mentioned exceptions).

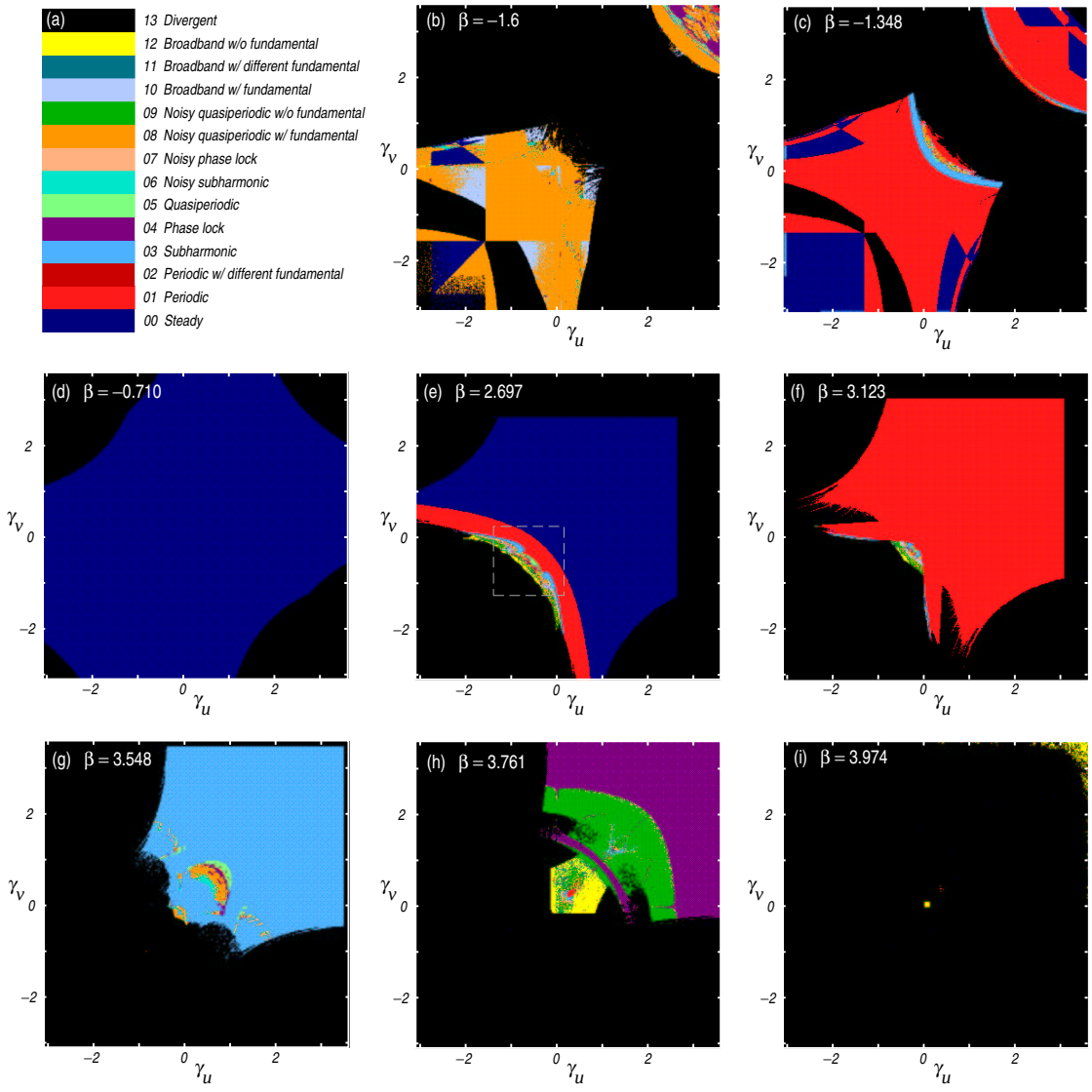

Figure 21: Bifurcation map for $\beta_u = \beta_v$, βs vary on both axes from -2.2 to 4.4. The animation (565 KB) corresponds to allowing $\beta_u = \beta_v$ to vary from -2.0 to 4.0 in increments of $\Delta\beta \approx 0.194$.

As we have discussed most of the interesting behavior occurs in the ranges $-2 \leq \beta \leq -1$

and $3 \leq \beta \leq 4$. Accordingly we note that we have resolved little of these regions with the coarse steps between slides in the previous movie. Therefore we present additional movies corresponding to these regions. A single still frame from each are shown in Figures 22(a) and (b). Click on each of these to open up the movie viewer. Part (a) (Movie 6) considers the negative β case and, part (b) (Movie 7) the positive β case. The β step size between successive images varies as we have chosen interesting values of β from the original regime map, and these values are given at the top of each slide. The grid spacing is $\Delta\gamma \approx 0.0145$ in both the x and y directions over the γ range $-3.4 \leq \gamma \leq 4.0$, corresponding to maps that are 512×512 grid points.

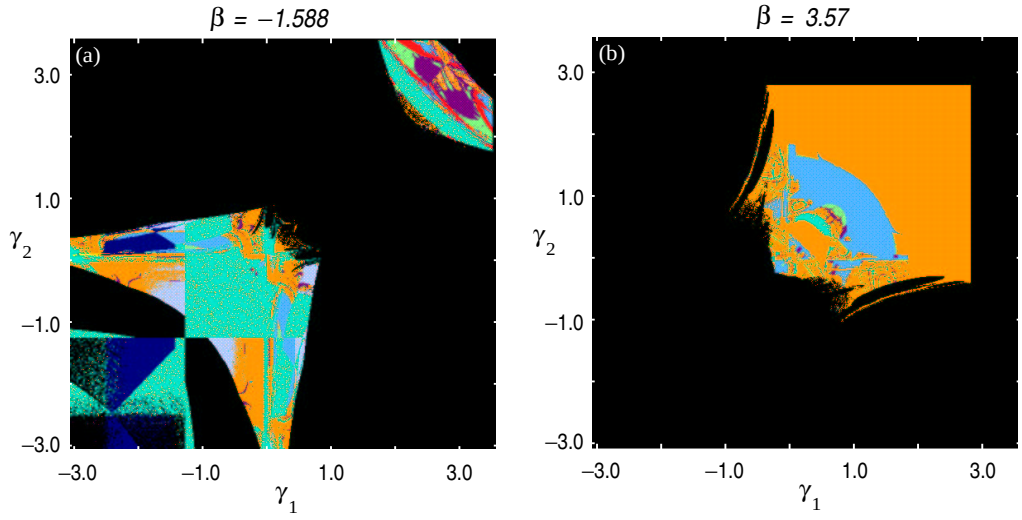

Figure 22: Bifurcation map movies for $\beta_1 = \beta_2$, γs vary on both axes from -3.1 to 3.6. The animation corresponds to allowing $\beta_1 = \beta_2$ to vary from -2.0 to -1.0 (part (a)) and 3.0 to 4.0 (part (b)).

The details illuminated in these movies emphasize the large range of behaviors that can be seen in a relatively small parameter space. Concerning turbulence modeling it is not known whether or not this is necessarily a good feature. Such sensitivity might be advantageous in simulating physical transitions from one flow state to another while it would be disadvantageous if it is found that the subgrid-scale model promotes instability in the large-scale calculations when transitioning often between, *e.g.*, subharmonic and chaotic behavior often. The wholesale changes seen over small changes in β in both movies are

related to the "columns" of solutions seen in the original regime map and the "shell" of solutions seen in the previous section.

As in the previous section we now examine arbitrary regions that appear interesting in the regime maps of Figure 22 and aid our overall understanding of the behavior of the PMNS equations. First we investigate the regime map of Figure 22(b). Particularly interesting is the fractal nature of the region in the upper right-hand corner of this regime map which is shown in detail in Figures 23(b,c). Next we show (in Figures 24(b,c)) and describe the colorful region of interesting behavior that is hopefully recognized by now as displaying the RTN transition and which was outlined in Figure 21(e).

The last group of bifurcations, from subharmonic/quasiperiodic to successive modes of chaos, are in a relatively small parameter space, usually somewhere between $\beta \approx 3.4$ and $\beta \approx 4.0$ in the positive case and between $\beta \approx -1.4$ and $\beta \approx -2$ in the negative case. We have chosen to show details of an example after this transition occurs for the negative β case. Specifically the γ_u versus γ_v regime maps of Figure 23 correspond to a $\beta_u = \beta_v$ value of -1.6. From Figure 21(b) we see that noisy quasiperiodic with the fundamental frequency trajectories are most prevalent over much of the nondivergent range of γ values. There are also regions of subharmonic and steady trajectories as can be seen in the lower left-hand corner of Figure 21(b).

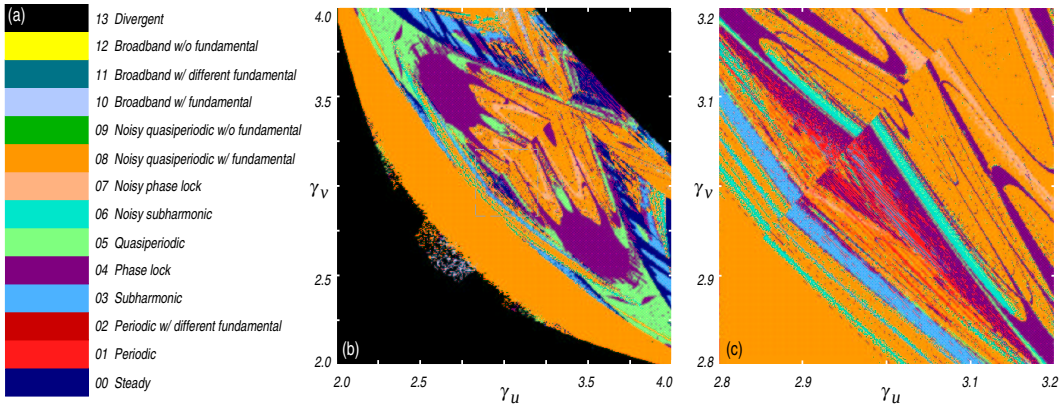

Figure 23: Details of $\gamma_u - \gamma_v$ regime map within high γ chaotic regime at $\beta = -1.6$.

More interesting, though, is the region at the upper right-hand corner of the regime map of Figure 21(b). To investigate this area we again perform the calculations on successively

finer grids. Indeed, as one can see from examination of Figures 23(b) and (c), a wide array of behavior types is seen within a small parameter space at this value of the βs. Easily distinguishable are regions of subharmonic, noisy subharmonic, quasiperiodic, noisy quasiperiodic, phase locked and periodic with a different fundamental behaviors. The basin boundaries can be classified as fractal and the high degree of "mixing" of the basins should be noted. Also, an interesting axis of threshold combinations of γ_u and γ_v values, especially evident in Figure 23(c), is seen though little is known about the reasons for the occurrence of such an axis, other than the that it is likely dependent upon the choice of initial conditions.

Lastly we consider the interesting region observed at moderate β values as, *e.g.*, in Figure 21(e). As mentioned previously this region exists over a wide range of β values but migrates in $\gamma_u - \gamma_v$ space as the values of the βs are varied. It also grows in size until the transition to mostly subharmonic behavior occurs at $\beta \approx 3.2$.

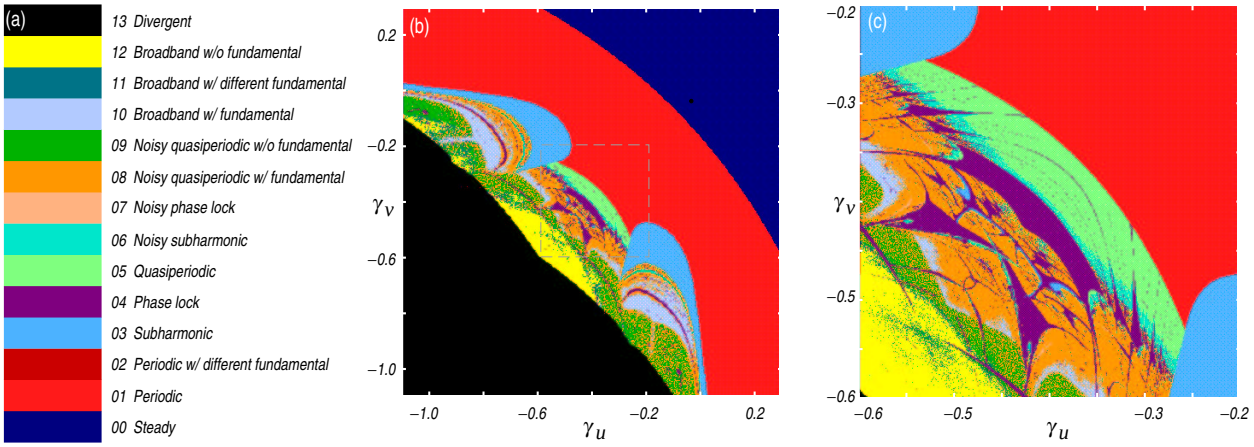

Figure 24: Details of $\gamma_u - \gamma_v$ regime map displaying RTN transition at $\beta_u = \beta_v = 2.91$.

In Figure 24(a) we again present the color table and list the behaviors associated with those colors. In part (b) we display the γ_u-γ_v regime map over a range of values from $-1.1 \leq \gamma \leq 0.3$ calculated for the $\beta_1 = \beta_2$ parameter value of 2.91. In part (c) we provide a zoomed-in view of the most interesting part of this regime map, from γ values of -0.6 to -0.2. The transition is that described previously through noisy phaselocked behavior, though the psd analyzer, in error, indicates noisysubharmonic after quasiperiodic. Readers more familiar with dynamical systems will notice the many Arnol'd tongues of part (c). In

Figure 25 we present example phase portraits associated with this transition, which should be familiar to the reader by now. The bifurcation parameter values at which these trajectories were calculated are given in the figure caption.

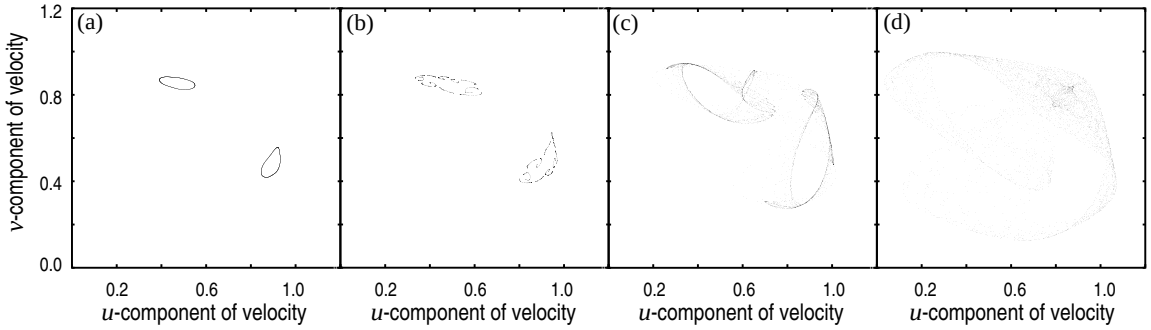

Figure 25: Phase portrait displaying the RTN transition to chaos through noisy phaselocked behavior at $\beta = 2.91$; (a)$\gamma_u = -0.45, \gamma_v = -0.32$, (b)$\gamma_u = -0.52, \gamma_v = -0.32$, (c)$\gamma_u = -0.58, \gamma_v = -0.41$, (d)$\gamma_u = -0.65, \gamma_v = -0.48$.

4.2.3 $\beta_u \neq \beta_v$, $\gamma_u \neq \gamma_v$

As the last generalization to make concerning the 2-D PMNS equations we need to discuss allowing the independence of all four bifurcation parameters. Least of all a brief study of this case, which is all that is possible here, will tell us if general behaviors and trends, *e.g.* the previously defined common regions of chaos, persist.

We have deliberated on the proper method to present results in this section and have concluded that regime maps of the type presented in the first section with β versus γ will be best, even though each is likely to be steady or divergent over a large portion of the entire relevant parameter space, as was the original regime map (Figure 6). The figures of this section consist of β_v versus γ_v maps calculated for various selectively chosen values of β_u and γ_u. In all of these we have reverted to the default initial condition ($a^0 = 0.4$, $b^0 = 0.61$). The parameter ranges are $-2 \leq \beta_v \leq 4$ and $-3.4 \leq \gamma_v \leq 4.0$ using a grid that is 1024×1024 corresponding to $\Delta\gamma \approx 0.0072$ and $\Delta\beta \approx 0.0058$. Since the parameter space is four dimensional it is very difficult to describe the effects of altering 1 bifurcation parameter separately so we will concentrate on relating the findings in this section to those in previous

sections so that they are more intuitive.

In Figure 26 four sets of regime maps are presented. The first two plots are of cases for which the sets of bifurcation parameters corresponding to the u-component equation are in the high γ chaotic region. Specifically, we have chosen $\beta_u = -1.59$ and $\gamma_u = 3.395$ and $\beta_u = -1.6, \gamma_u = 3.1$, respectively. Recall that for the first case we have found that, when $\beta_u = \beta_v$ and $\gamma_u = \gamma_v$, the basins of attraction (Figure 15(a)) corresponded to both a phase locked and a quasiperiodic attractor. In Figure 26(a) we see that these attractors are quite unstable to perturbations in the bifurcation parameters as only a relatively small region of nondivergence is seen over the entire $\beta_v - \gamma_v$ parameter space. Secondly, in Figure 26(b), we present another high γ case with reduced γ_u. This region displays only a slightly larger region of nondivergence and a larger region of periodicity. We note also that these regions occur for relatively high γ_v values, corresponding to high strain rate components in those directions.

Next we look at a set of bifurcation parameters within the tails displaying the RTN transition at moderate β values in the case where both constraints were applied. Specifically we look at the cases where $\beta_u = -1.26$ and $\gamma_u = 0.388$ and where $\beta_u = 1.1$ and $\gamma_u = -1.01$, respectively. The β_v versus γ_v regime maps are presented in Figures 26(c) and (d). The regime map for the negative β case (part (c)) is somewhat more complex than that for positive β and displays a greater amount of periodicity, *i.e.*, it is closer to the chaotic regime. Also, the resemblance of part (d) and the original regime map is of note. In both cases chaos is primarily associated with regions in the far left and far right of the plots, corresponding to relatively low and high values of β_v, again suggesting that threshold values of β exist after which chaos is "most likely" to occur.

Next we look at the moderate value γ regions of chaos that experience a period doubling cascade to chaos with increasing magnitude of the βs in the doubly constrained case. In Figure 27(a) and (b) we present β_v versus γ_v regime maps for the two cases $\beta_u = -1.626, \gamma_u = -0.42$ and $\beta_u = -1.793, \gamma_u = -0.264$. These values of β put us well into the chaotic regimes of Figure 6. Due to this the regime maps of Figure 27(a) and (b) show a large area of chaos spanning the entire range of β_v. Previously unseen is the chaotic behavior that occurs at low magnitudes of β_v, *e.g.*, $\beta_v = 0$.

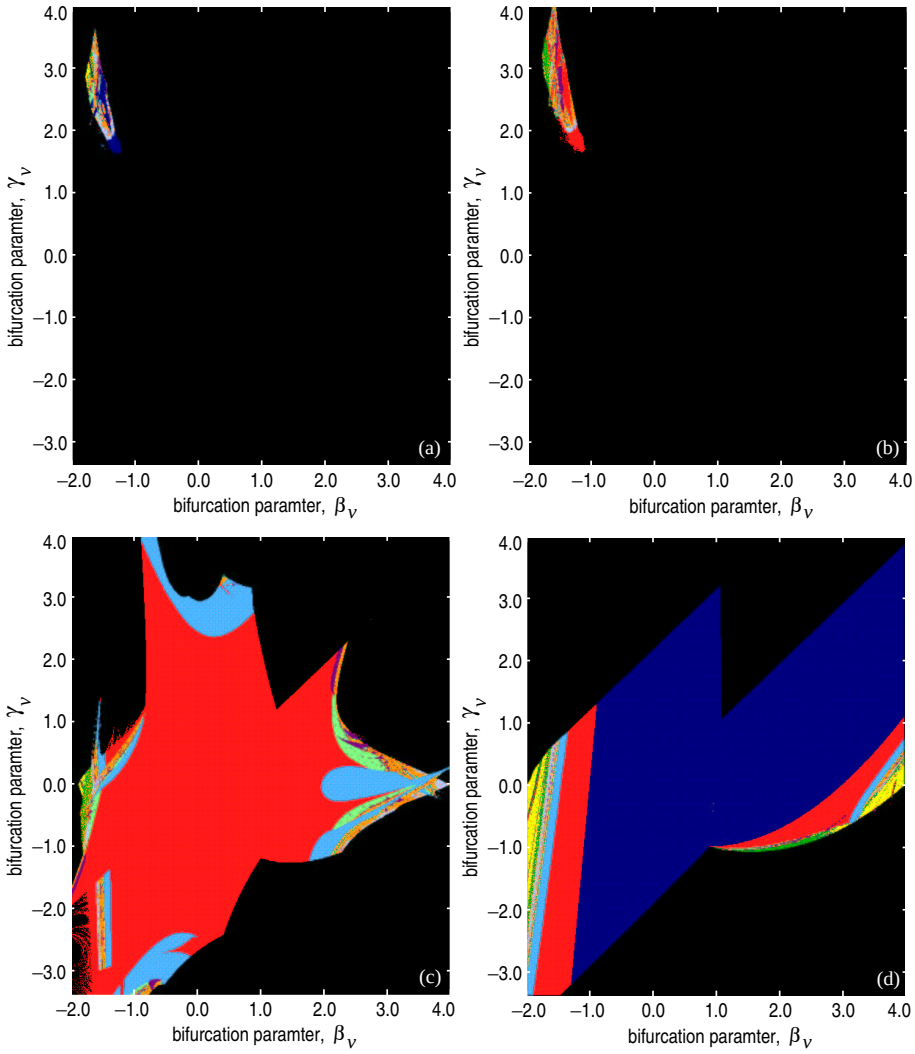

Figure 26: $\beta_v - \gamma_v$ regime maps corresponding to hand-picked values of β_u and γ_u.

Next we look at cases within the range of β previous classified as noninteresting ($-1 \leq \beta \leq 3$) to see if the uncoupling of all of the bifurcation parameters adds a great deal of interesting behaviors to this region. The regime maps of Figures 27(c) and (d) correspond to the two cases ($\beta_u = -0.5, \gamma_u = 2.1$) and ($\beta_u = 2.0, \gamma_u = 0.156$), respectively. We see that, as we would expect, additional interesting behavior is seen as the magnitude of β_v grows. Interesting though is that chaos occurs in the first case (part (c)) for β_v values that would only have been steady for the coupled case. This is assumed to be caused by relatively high value of γ_u which was used in this case. The figure in part (d) again resembles the original

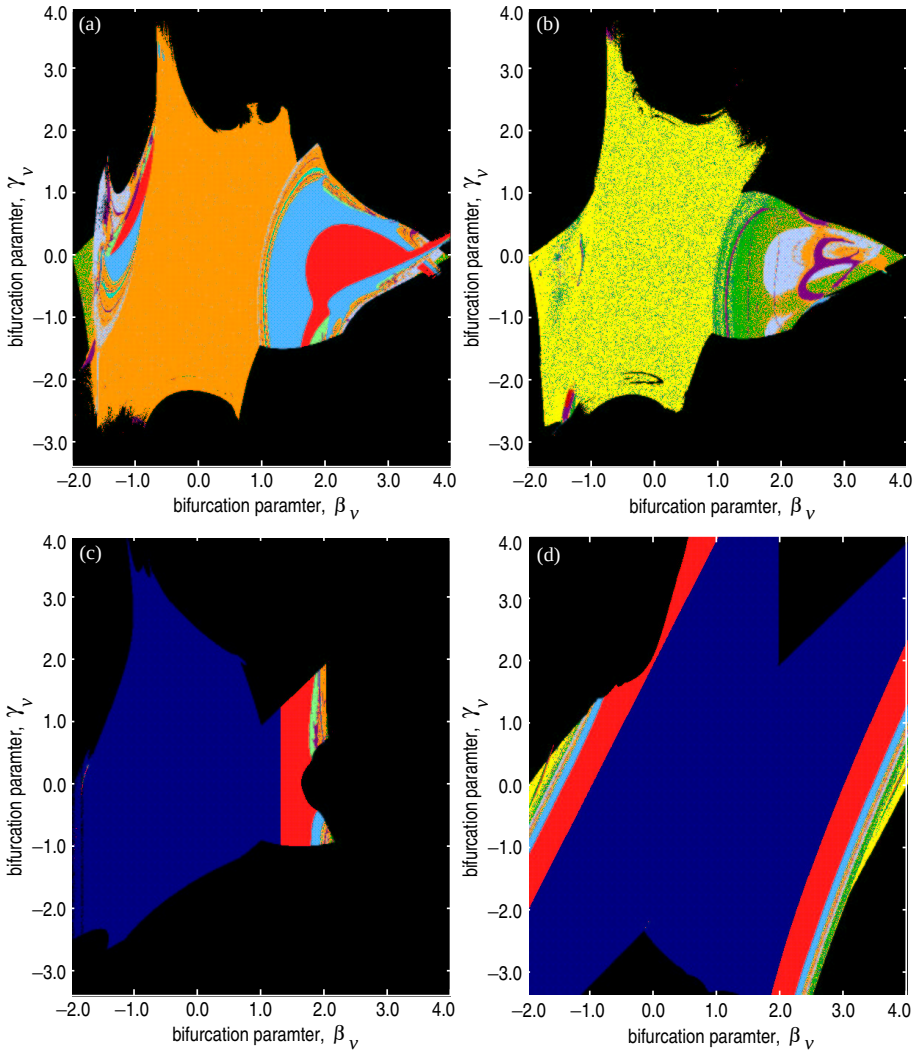

Figure 27: $\beta_v - \gamma_v$ regime maps corresponding to hand-picked values of β_u and γ_u.

regime map.

Finally we present some other various $\beta_v - \gamma_v$ regime maps from arbitrary locations in $\beta_u - \gamma_u$ space. These were found for the following sets of bifurcation parameters: part (a); ($\beta_u = -1.602$, $\gamma_u = 0.456$), part (b); ($\beta_u = 3.52$, $\gamma_u = 0.62$), part (c); ($\beta_u = 3.59$, $\gamma_u = 0.1$) and part (d); ($\beta_u = 3.85$, $\gamma_u = -0.05$). We first note about these regime maps the common geometries they share with one another and with those regime maps seen previously and which could possibly be useful in choosing the proper ranges of β and γ in 2-D simulations. Second we note that generally the regime previously referred to as high γ chaos is not seen

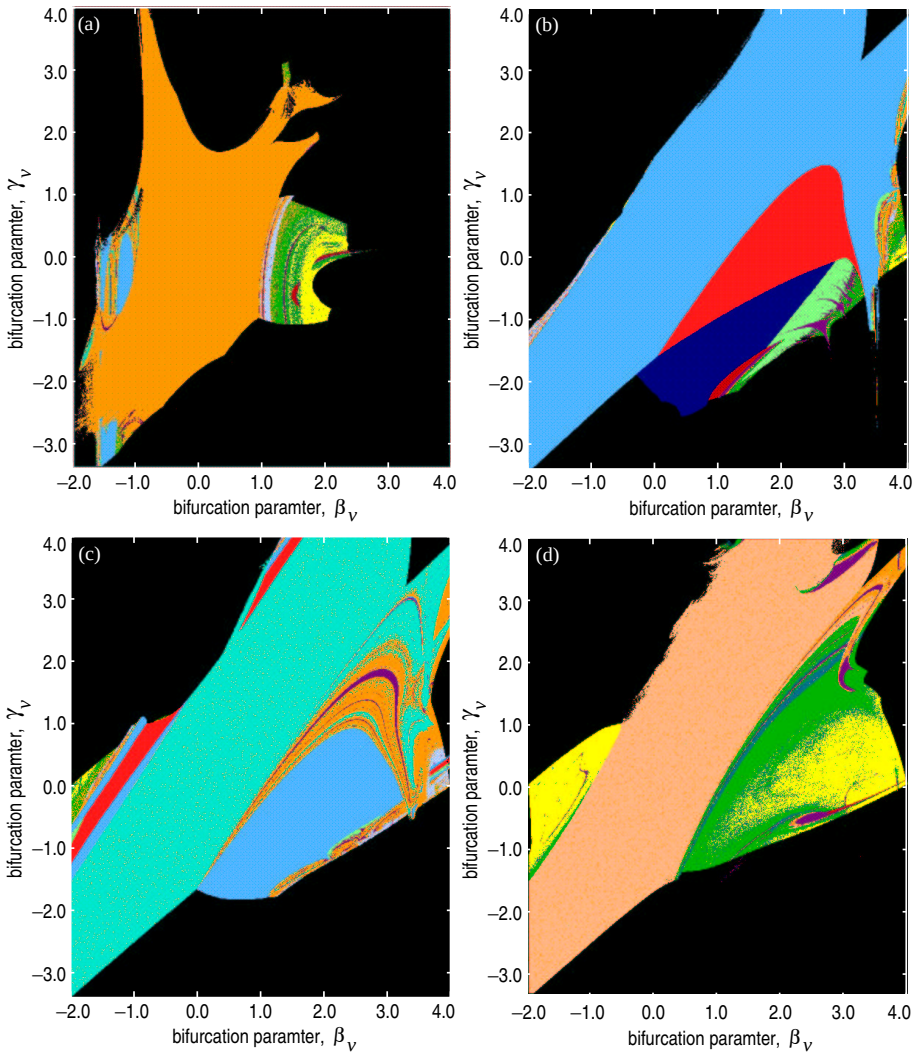

Figure 28: $\beta_v - \gamma_v$ regime maps corresponding to hand-picked values of β_u and γ_u.

for $\beta < 0$ and low γ chaos is not generally seen for $\beta > 0$. This issue could complicate the modeling procedure and could require separate restrictions on γ depending on which side of 0 the βs are on. These figures also indicate that general regimes tend to stretch across all of the $\beta_v - \gamma_v$ space generally depending on the value of β_u for their overall nature. Primarily there is a region of similar behaviors that stretches across the $x - y$ axis and in addition there are often regions of unique behaviors in a small portion of the highly negative β_v range (often near $\gamma_v \approx 0$) and in a triangular region for $1 \leq \beta_v \leq 4$ and $-0.5 \leq \gamma_v \leq 1.5$.

In finishing the discussion of the 2-D PMNS equations we include in Figure 30 pictures

of a few of the strange attractors we have seen that we think are interesting. We note the similarity between some of these and those seen in a previous study of a similar quadratic map by Sprott [115]. The wide range of geometric attractors seen in the uncoupled bifurcation parameter case can be contrasted to the small set of interesting attractors in the fully coupled case described previously. The bifurcation parameter values at which these trajectories were calculated are as follows: part (a); $(\beta_u = -1.26, \beta_v = 2.97, \gamma_u = 0.4, \gamma_v = 0.46)$, part (b); $(\beta_u = -1.26, \beta_v = 2.99, \gamma_u = 0.4, \gamma_v = -0.28)$, part (c); $(\beta_u = -1.26, \beta_v = -1.78, \gamma_u = 0.4, \gamma_v = -0.49)$, part (d); $(\beta_u = -1.626, \beta_v = -1.78, \gamma_u = -0.42, \gamma_v = -0.49)$, part (e); $(\beta_u = -1.626, \beta_v = 3.1, \gamma_u = -0.42, \gamma_v = -0.45)$, part (f); $(\beta_u = -1.626, \beta_v = 2.03, \gamma_u = -0.42, \gamma_v = -1.27)$.

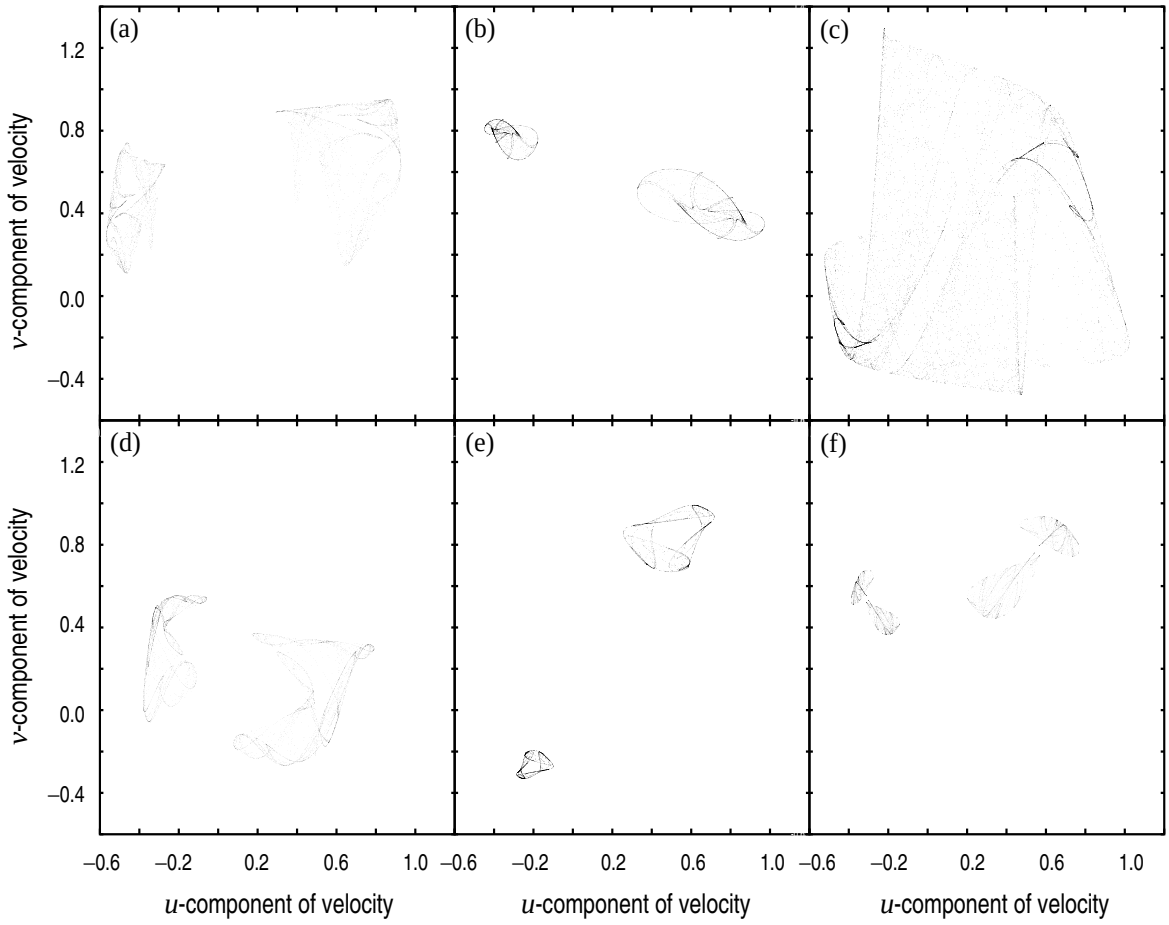

Figure 29: Various strange attractors.

V. STUDY OF THE 3-D PMNS EQUATION

The 3-D PMNS equations should be considered more important than the previously studied 2-D case since most often we will be performing turbulence simulations of three dimensional flows. We begin our study by recalling the form of the 3-D PMNS equation that was introduced in Chapter 3:

$$a^{n+1} = a^n \beta_1 (1 - a^n) - \gamma_{1,1} a^n b^n - \gamma_{1,2} a^n c^n, \tag{41a}$$

$$b^{n+1} = b^n \beta_2 (1 - b^n) - \gamma_{2,1} a^n b^n - \gamma_{2,2} b^n c^n, \tag{41b}$$

$$c^{n+1} = c^n \beta_3 (1 - c^n) - \gamma_{3,1} a^n c^n - \gamma_{3,2} b^n c^n. \tag{41c}$$

First we note that this system of discrete equations has nine independent bifurcation parameters. This makes a systematic study of the DDS difficult. Here we will study the above equations using a number of levels of simplification, analogous to those used in the 2-D case, to gain an understanding of their behavior. Hopefully the discussions of the previous section will be helpful in forming an intuition concerning their generic behavior.

5.1 $\beta_1 = \beta_2 = \beta_3$, $\gamma_{1,1} = \gamma_{1,2} = \gamma_{2,1} = \gamma_{2,2} = \gamma_{3,1} = \gamma_{3,2}$

By equating all three βs and likewise all six γs we reduce the number of independent parameters to two. The 2-D regime map corresponding to this simplification is presented in Figure 30. Here we have used a 512×512 grid to cover the region $[\beta, \gamma] \in [-2 : 4, -3.1 : 3.6]$. We once again present the color table we have used in Figure 30(b) and the regime map in part (a). Herein we have implemented the default 3-D initial conditions, viz., $a^0 = 0.4, b^0 = 0.61, c^0 = 0.53$.

We see that there are definite similarities between this regime map and that previously studied for the 2-D PMNS equation. This is an initial indication that the behavior is generically the same as that for the 2-D case which has been studied extensively. There are additional qualities seen in the regime map to note. First is that the region previously referred to as low β, high γ chaos has disappeared almost completely. This phenomenon has occurred for all of the many initial conditions sets that we have tested, though we do not

present those maps here. Therefore it is apparently a consequence of the further coupling of the third nonlinear equation that is introduced in the 3-D case. In addition the area of nondivergence for both positive and negative βs has been reduced considerably from that seen previously. This reduction occurs in the γ direction while the bifurcations in the β direction remain consistent with those previously seen, as we would expect since the nonlinear coupling is by γ.

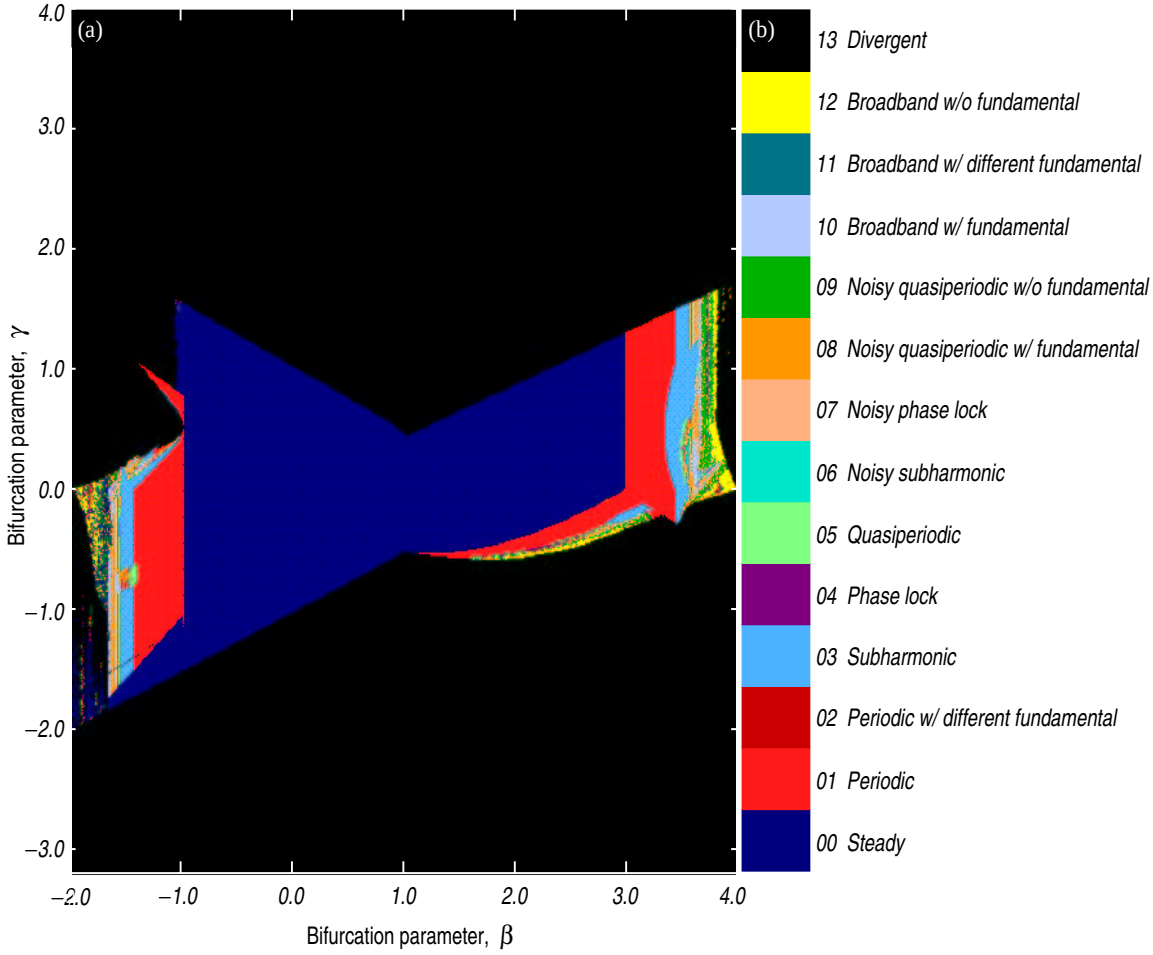

Figure 30: Regime map of 3-D PMNS equation with $\beta_1 = \beta_2 = \beta_3$ and $\gamma_{11} = \gamma_{12} = \gamma_{21} = \gamma_{22} = \gamma_{31} = \gamma_{32}$.

5.2 $\beta_1 = \beta_2 = \beta_3$, $\gamma_{1,1} = \gamma_{2,1} = \gamma_{3,1}, \gamma_{1,2} = \gamma_{2,2} = \gamma_{3,2}$

By a slight variation of the previous simplification the number of independent parameters

is increased to three. The coupling that is implemented in this section is the following: $\beta_1 = \beta_2 = \beta_3$, $\gamma_{1,1} = \gamma_{2,1} = \gamma_{3,1}$, $\gamma_{1,2} = \gamma_{2,2} = \gamma_{3,2}$. We denote these values as β, γ_1 and γ_2, respectively. We will be using much coarser grids in this section and those that follow for two reasons; first file sizes would become unmanageable if not, and second our purpose in these sections is not to detail specific regime maps, as has been done previously, but to identify trends in such regime maps and similarities with the well studied 2-D case.

The $\gamma_1 - \gamma_2$ regime maps of Figure 31 correspond to the above case and consist of 128×128 evenly spaced grid points in those directions. The range of each is $-3.1 \leq \gamma \leq 3.6$. Part (a) corresponds to a β value of -1.7, part (b) to $\beta = 2.58$, and part (c) to $\beta = 3.72$. We have included a movie that includes $\gamma_1 - \gamma_2$ regime maps for many other values of β between -2 and 4. The reader can access this movie 8 (3.4 Mb) by clicking on the figure, as before. The similarities between this movie and Movie 5, associated with $\gamma_u - \gamma_v$ regime maps in the 2-D case, should be noted. Again most of the interesting behavior occurrs for $-2 \leq \beta \leq -1$ and $3 \leq \beta \leq 4$. A notable exception to the similarity of the two is the absence of the low β, high γ chaos, as was also seen in the previous section. We will not go into any more detail on this case.

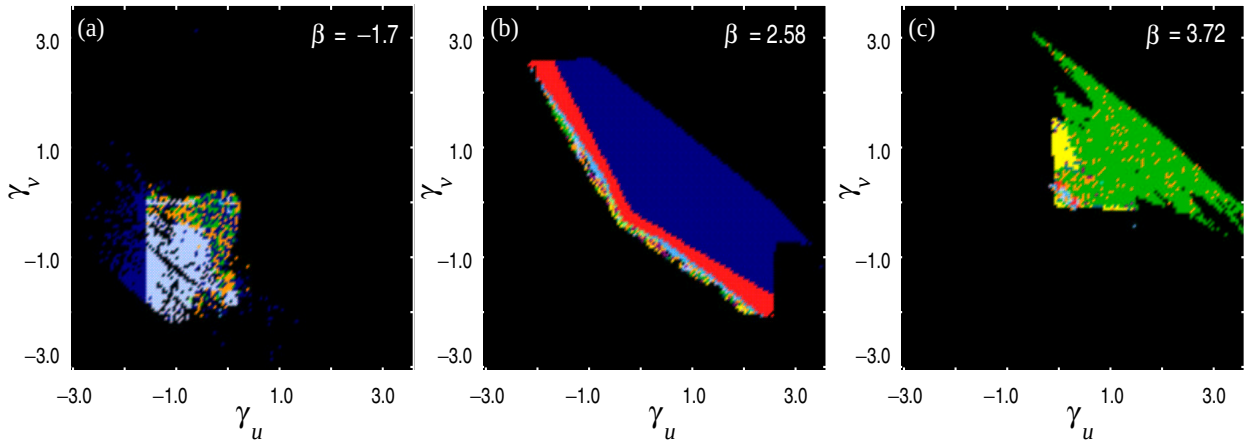

Figure 31: Plots and movie of $\gamma_1 - \gamma_2$ regime maps at various values of β.

5.3 $\gamma_{1,1} = \gamma_{1,2} = \gamma_{2,1} = \gamma_{2,2} = \gamma_{3,1} = \gamma_{3,2}$

Another simplification that will aid our understanding is that to 4 four dimensions in which the four independent parameters are β_1, β_2, β_3 and γ, where $\gamma = \gamma_{1,1} = \gamma_{1,2} = \gamma_{2,1} = \gamma_{2,2} =$

$\gamma_{3,1} = \gamma_{3,2}$. Generally we have defined three subregions of γ space, viz., low, moderate, and high. Therefore we will present movies displaying the 3-D β space for an example γ value within each of these subregions. Movies 9 (3.3 Mb) 10 (5.3 Mb) and 11 (3.4 Mb)

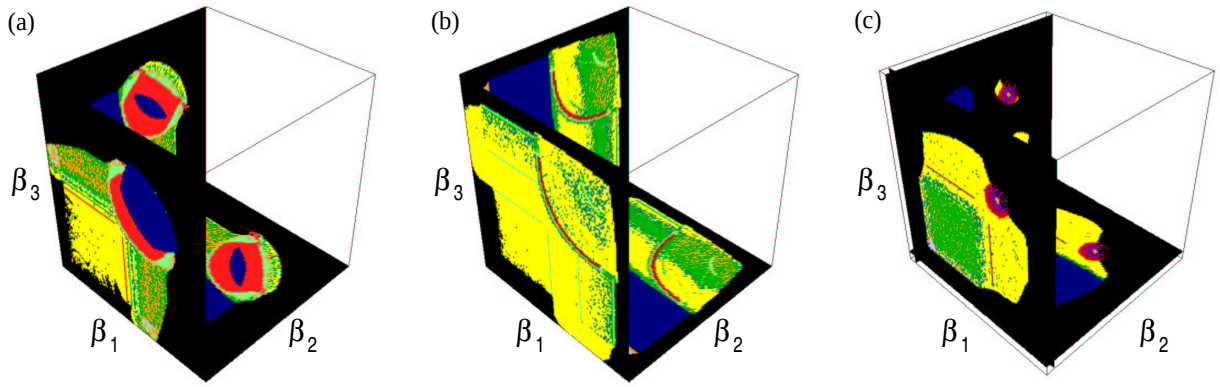

Figure 32: Plots and movies of $\beta_1 - \beta_2 - \beta_3$ regime maps at three values of γ.

of Figure 32 consist of multiple frames corresponding to grids of 128×128 evenly spaced grid points in the $\beta_2\beta_3$-plane. Each frame is for a specific value of β_1 and in turn each movie corresponds to a specific value of γ. The movie of part (a) corresponds to a value of $\gamma = -0.75$, part (b) to a value of $\gamma = -0.175$, and part (c) to a value of $\gamma = 0.3$. Continuing to look for simplifications of the 3-D PMNS equation is not pursued here for two reasons; viz., any higher dimensional simplification is not likely to provide futher knowledge of the qualitative behavior of the system and will most likely behave in an overly simplified manner with respect to the unsimplified equations.

5.4 Full Parameter Space

The complete description of a 12-D parameter space, such as that associated with the PMNS equation, where the system displays chaotic behavior is, as the reader may by now have realized, extremely labor intensive if not impossible. In this section we hope to shed light on this full parameter space by picking a few specific cases to investigate in the same detail as those previously. Here we have chosen to examine two cases. The first examines the effects of varying one γ values and the second measures the effects of varying one β value. The best way to measure such effects is, again, viewing regime maps. Specifically, in the first

case we study the $\beta_3 - \gamma_{3,2}$ regime map at eight values for $\gamma_{3,1}$ in the range $[-2.5 : 2.5]$. The remaining parameter values are as follows: $\beta_1 = -1.5$, $\beta_2 = 3.75$, $\gamma_{1,1} = 0.05$, $\gamma_{1,2} = -0.1$, $\gamma_{1,2} = 0.1$ and $\gamma_{2,2} = 0.05$. These regime maps can be viewed by clicking to access the movie (Movie 12) of Figure 33(a).

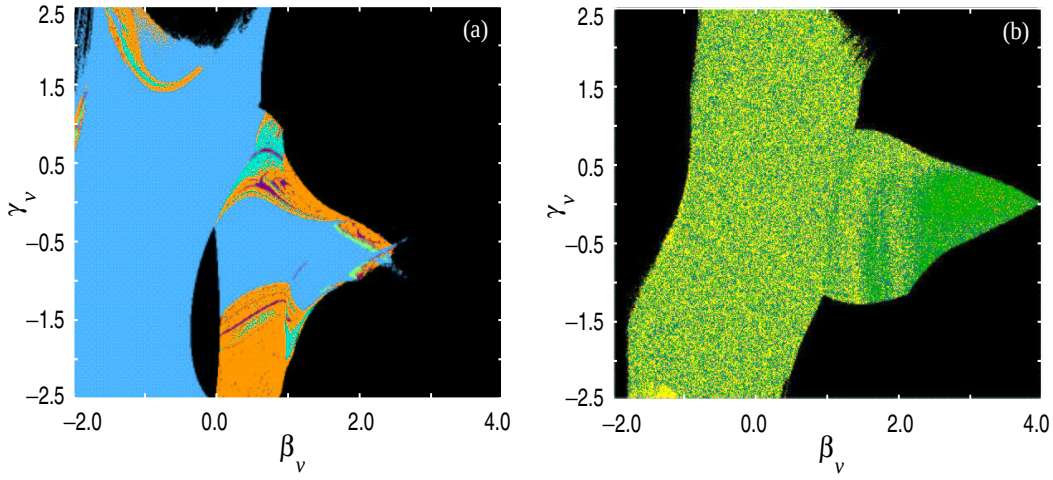

Figure 33: Plots and movies of regime maps for the uncoupled bifurcation parameters case.

In part (b) of the same figure we have embedded the second movie (Movie 13). Here we again view successive $\beta_3 - \gamma_{3,2}$ regime maps but now they are taken at eleven unique values of β_1 in the range $[-1.75 : 3.75]$ while the other parameter values are as follows: $\beta_2 = 3.75$, $\gamma_{1,1} = 0.05$, $\gamma_{1,2} = -0.1$, $\gamma_{1,2} = 0.1$, $\gamma_{2,2} = 0.05$ and $\gamma_{3,2} = 0.0$. As we would expect due to our previous discussions we find that the variation of β_1 as is done in part (b) causes a more noticeable effect on the regime maps than does the variation of $\gamma_[3, 1]$ as was shown in part (a). We also notice that the same general geometry is seen that has been noted previously for $\beta - \gamma$ regime maps seen in the 2-D case with unequal bifurcation parameters. These similarities are more than enough to conclude that, analagous to the way the 2-D equations were shown to behave similarly to the 1-D logistic map, the 3-D equations will generally behave similary to the 2-D equations.

In conclusion the 3-D equations will display the following general behaviors. First is that the βs act as the main bifurcation parameters. That is transition sequences are associated with varition in the β more so than with the γs. That is not to say important transitions do

not occur with variation of the γ as was shown to be the case for the tails associated with the RTN transition to chaos seen in the 2-D equations. But generally a high magnitude for any β values is enough to guarantee chaos over some portion of the remaining 8-D bifurcation parameter space while high magnitude γ values do not guarantee interesting behavior and, in the positive γ case, will often lead to large regions of divergence over the remaining parameter space. This view of the dynamics of the PMNS equations correlates well with our perception of turbulence associated with the Navier-Stokes equations, *viz.* generally flows act similarly with respect to bifurcations to turbulence with respect to increasing Reynolds number, though the details vary, while in contrast they display traits that are quite diverse and flow type specific (*e.g.* shear flows, jet flows, etc.) indicative of the connection between flow dynamics (bifurcations) and flow physics (*e.g.* velocity gradients). Second is that most interesting behavior will occur for at least one of the βs within either the region $[-2,-1]$ or $[3,4]$ though exceptions have been seen. In addition, the choice of the remaining βs to be within the so-called noninteresting region ($[-1,3]$) does not include addition behaviors that are not seen if those βs are restricted to the interesting regions as the chaotic regimes stretch across the entire remaining parameter space as was hinted at in the Figures 28. This characteristic will aid in the implementation of the SGS model as it allows for us to restrict the β to the ranges $[-2,-1]$ and $[3,4]$ without omitting a statistically significant amount of interesting behaviors that might be physically realistic while avoiding the large regimes of steadiness and divergence seen for the uninteresting ranges where the model would be turned off.

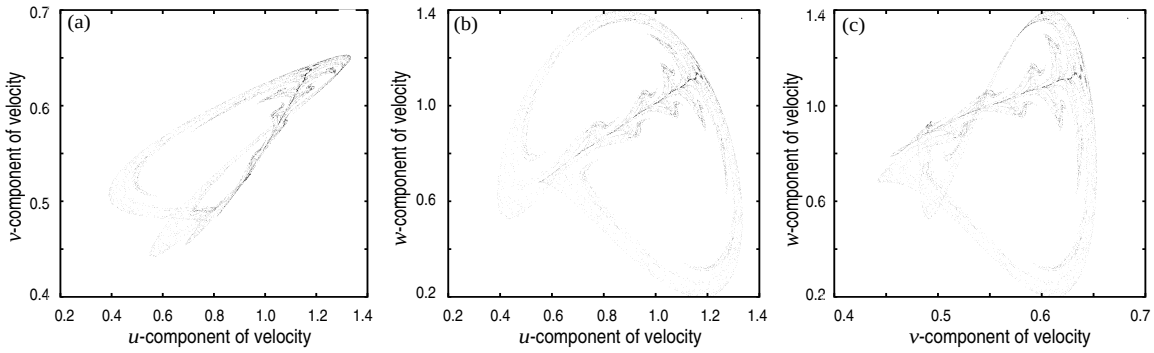

Figure 34: A 3-D strange attractor.

Of course the strange attractors of the full 3-D equations show an increase in complexity beyond those seen previously, as can be seen in the three planar projections of the strange attractor of Figure 34. This trajectory was calculated using the default initial conditions and the bifurcation parameter values: $\beta_1 = 1.1$, $\beta_2 = 1.34$, $\beta_3 = 1.8$, $\gamma_{1,1} = -0.7$, $\gamma_{1,2} = -0.66$, $\gamma_{2,1} = -0.2$ and $\gamma_{2,2} = -0.25$, $\gamma_{3,1} = -1.06$ and $\gamma_{3,2} = 0.0$. Unfortunately this calls into question whether the previous discussion concerning the restriction of the β values is valid, as this trajectory is seen for all three βs within the so-called noninteresting range. It is possible that similar attractors can be found for βs within the interesting ranges, but we have not found any to speak of.

VI. A PRIORI TESTING OF PMNS TURBULENCE MODEL

In this chapter we investigate the validity of the "poor man's Navier-Stokes" equation as a subgrid-scale "synthetic velocity" model for use in turbulence simulations. In Chapters IV and V we demonstrated that the PMNS equation produces a wide array of behaviors, but it has yet to be shown that they can produce physically realistic time series. Here we perform *a priori* tests of the PMNS equation turbulence model by testing its ability to produce physically realistic turbulent fluctuations. This is accomplished by qualitatively and quantitatively judging the likeness of a time series produced by weighted linear combinations of this dynamical system and that of a high-pass filtered turbulent signal from experiment.

6.1 *A PRIORI* TESTING OF SGS MODELS

Most often SGS models are tested *a priori*, *i.e.* in the absence of any LES, since this type of test is more fundamental as a consequence of the fact that it is not affected by the spurious sources of error inherent in LESs such as numerical discretization, aliasing, etc.. In such tests the model dependent variables are calculated using fully resolved data from an experiment or DNS and then model output (employing model parameter values calculated from the resolved data) is compared with this data. As such, the test that we consider here could be categorized as a doubly *a priori* test in that the model independent variables are not calculated *per se* using resolved data but, instead, optimal model independent variables are found using a curve fitting algorithm. The test considered here also differs from most in that statistics are not calculated and compared to experiment/DNS but, instead, SGS velocity fluctuations are used as the basis for comparison.

Ideally the SGS model, when implemented in an LES, would produce LES results that compare well with measurements of statistics such as drag coefficients, mixing rates, etc. from experiment or DNS. In addition one would like to reproduce dynamical characteristics such as the so-called "turbulence structures," *e.g.* vorticity tubes, intermittent bursts, etc.. As the study of SGS synthetic velocity models is still in its infancy, little is known of the properties of these models that are most important in regards to the overall success of the

LES in which they are to be used. Here we take the position that with so little known about the quantitative characterization of successful SGS velocity models the most reasonable characterization parameter is the "qualitative appearance" of the velocity time series. It is important to note that SGS velocity models *should not* aim to reproduce exactly the SGS velocities as separate realizations of any turbulent flow are unique due to the sensitivity to initial conditions characteristic of turbulence.

In the following subsection we will discuss the characterizing parameters of chaotic signals that might be used to quantify the qualitative similarity of individual time series. Next we proceed to discuss the experimental turbulence data used here, the specific form the synthetic velocity model takes and the algorithm which we have used to optimize the synthetic velocities.

6.2 ANALYZING CHAOTIC SIGNALS

The field of analysis of chaotic data sets has seen tremendous growth in the last decade with studies being aimed at the prediction of future states of financial, biological, ecological, and environmental systems to name a few (see Schreiber and Schmitz [116] and references therein). Primarily the current research concerns the extraction of nonlinear dynamical systems associated with a particular data set and use of these systems for prediction (see, *e.g.* Gollub *et al.* [117]). The approach that we take is somewhat different in that we are attempting to validate a given model by curve fitting its time series to that of a chaotic system over short time intervals and thus the methods that we will be using are noticably different and, in a sense, less demanding since we will never require exact prediction of future states but only that the dynamics of the model system are qualitatively similar to that of the experimental time series.

As we have noted previously the bifurcation parameters of Eqns. (41) must be calculated automatically using Eqns. (28) and (32). This requires determination of the relevant constants in those equations. One method for extracting such constants would be through the curve fitting procedure discussed here using full spatial and temporal data. Here we will demonstrate the ability of the PMNS to mimic, qualitatively and semi-quantitatively, the dynamics inherent in the small-scales of turbulent flows through curve fitting of the optimal

bifurcation parameters, thus allowing the determination of said constants given that the appropriate data were available. Here we examine the characteristics of chaotic signals that are most relevant to curve fitting with special regards to reproducing the dynamics necessary for success of a SGS synthetic velocity model.

Given two time series the reader would most likely be able to judge the degree of similarity of the two through qualitative comparisons. For our purposes we must quantify such qualitative assessments by recognizing the aspects of time series that are used in such reasonings. We comment that, to date, most efforts in this subject area have concentrated on curve fits that are alternative to that presented here in that they attempt to minimize the point-to-point error in the fabricated time series. We do not think that such an approach is justified (in this case) due to the sensitivity to initial conditions previously mentioned inherent in turbulence, and thus we will not use it. An alternative procedure is one that uses time series characterization parameters that are indicators of the qualitative appearance of the the time series. In this case these characterization parameters are classified into three categories: statistical properties, dynamical systems properties, and turbulence specific properties.

In McDonough *et al.* [118] such an approach was taken to fitting linear combinations of the 1-D logistic map to a time series from a chaotically forced instance of the 1-D Burgers equation with considerable success. Here we give a brief description of the rationale behind the parameters which were used in that study and which have been adopted in this study, along with parameters that are being implemented for the first time here. We can start with description of the most common statistical parameters; averages, variations, norms and correlations. We assume the reader is accustomed to positive, negative, and overall averages so we exclude their definitions. The *variation* property attempts to compensate for the lack of dynamical considerations inherent in averages by considering the average difference between successive signal values and is calculated (in the discrete signal case) as

$$\overline{V}(u) = \frac{1}{N-1} \sum_{n=1}^{N-1} |u^{(n+1)} - u^{(n)}|, \tag{42}$$

where u is the signal under consideration, and N is the total number of discrete values of $u^{(n)}$. Positive and negative variations can be defined in the same way as for positive and

negative averages where, in addition, each neighbor of the point being considered must be of the same sign as that point. The mathematical quantity widely used to describe the "size" of the signal is the norm. The most appropriate norm for physical systems in which the energy is finite for a finite time is the L^2 norm. For the discrete time signal considered here the L^2 norm is defined as

$$||u||_2 \simeq \left[\frac{T}{N-1} \sum_{n=1}^{N} |u^{(n)}|^2 \right]^{\frac{1}{2}}, \tag{43}$$

where T is the length of the "physical" time interval. Similarly the L^1 norm is

$$||u||_1 \simeq \frac{T}{N-1} \sum_{n=1}^{N} |u^{(n)}|. \tag{44}$$

The correlations of a signal are measures of the "memory" (or lack thereof) of the signal. The autocorrelation can be constructed for any value of time delay as

$$C(u,\tau) = \frac{\langle u(t), u(t+\tau) \rangle}{||u||_2^2} = \frac{1}{||u||_2^2} \int_0^T u(t)u(t+\tau)dt. \tag{45}$$

where τ is the time delay under consideration. Similarly we could measure the correlation of two of the dependent variables, removing the dependency on τ:

$$C(u_1,u_2) = \frac{\langle u_1(t), u_2(t) \rangle}{||u_1 u_2||_2} = \frac{1}{||u_1 u_2||_2} \int_0^T u_1(t)u_2(t)dt. \tag{46}$$

One seemingly unhelpful yet common definition of a "turbulent" time series is that the signal appears "chaotic", *i.e.*, it contains "structures" that deviate from a Gaussian distribution and multiple scales on which fluctuations occur. Such properties of a chaotic signal require additional characterization parameters for their quantification. It should be noted that visual inspection of the power spectrum and power spectral quantities such as maximum and minimum power and power decay rate are commonly used for this purpose but here we will not use any power spectra. Instead we will use statistical properties such as moments, dynamical systems properties such as the frequencies and magnitudes of slope changes and numbers of crossing points, and the turbulence property commonly referred to

as intermittency to characterize this qualitative behavior.

One can gain information similar to that contained in the PDF of the signal by considering the various moments of the data. The two most referenced moment calculations are the skewness (third moment) and flatness (fourth moment). These are, respectively,

$$S = \frac{\overline{u^3}}{\left(\overline{u^2}\right)^{\frac{3}{2}}} = \frac{\frac{1}{N}\sum_{n=1}^{N}(u^{(n)})^3}{\left[\left[\frac{1}{N}\sum_{n=1}^{N}(u^{(n)})^2\right]^{\frac{3}{2}}\right.}, \tag{47}$$

for skewness, and

$$F = \frac{\overline{u^4}}{\left(\overline{u^2}\right)^{2}} = \frac{\frac{1}{N}\sum_{n=1}^{N}(u^{(n)})^4}{\left[\left[\frac{1}{N}\sum_{n=1}^{N}(u^{(n)})^2\right]^{2}\right.}. \tag{48}$$

Use of crossing points in studies of dynamical systems dates back to the late 1800s as such points were used by Poincaré [61] to study the motion of stellar bodies and were found to be a good method of reducing the dimension of the system. For this reason we choose to calculate four such points of crossing at values of zero, the average, the positive average, and the negative average. Similarly the number of slope changes can be used to identify the number and frequency of oscillations, just as one does when visually inspecting a time series plot. Just as was done for the average and variation, we can also consider the fraction of this total where the value of the point at which the slope is changing is either positive or negative. The deficiency of quantifying only the number of slope changes is that fluctuations of any magnitude are grouped similarly. In an attempt to compensate for this we have made use of the turbulence specific property known as intermittency. Intermittency is usually quoted in reference to chaotic "bursts" seen in turbulence and is most often recognized as the ratio of the time during which the flow is turbulent at a particular point in the flow to the overall time. Here we quantify intermittencies by two features; the total number of oscillations that have magnitudes within given ranges, and the number of instances when the time between successive oscillations of each of these groups falls into time intervals of a given range. Finally, we also wish to differentiate between bursts that are centered upon the mean and those with a center of gravity displaced from the mean. Therefore we introducee a group of paramaters that calculate the average variances with respect to the mean of the

oscillations that fall within each of the specified oscillation magnitude ranges.

6.3 EXPERIMENTAL DATA

The main objective of this paper is to demonstrate the ability of the 3-D PMNS equation to produce physically realistic time series in the context of turbulence SGS modeling. To accomplish this task we must make use of real turbulence data. Due to the traditional interest in only statistics of turbulent flows, time series from points within a fully resolved turbulent flow have become increasingly hard to come by, but, infact, can be easily stored (for a minimal number of points) during DNSs. A corollary objective of this paper is to promote the storage and reporting of such time series as we believe they can be put to good use in the formulation of SGS models. Experimentally much work has yet to be done so that fully resolved, in space and time, turbulent data can be collected.

The data that we use here is from the homogeneous stably stratified shear turbulence experiments of Keller and Van Atta [119, 120] with a beginning Taylor microscale Reynolds number of $\Re_\lambda = 30$. Though vertical measurements of temperature were the main interest of that work we do not extend this study for temperature, though the thermal energy equation is easily incorporated into the model (see McDonough and Joyce [121]). Instead, we will utilize the time series of the u- and v-components of the velocity as the signal we wish to curve fit. The z-component was not measured. We note that intrinsically this means that our fitting will be underconstrained as we will be curve fitting two components of a 3-D dynamical system to a 2-D time series. The measurements of Keller and Van Atta were performed using standard X-wire and cold-wire techniques with measurement rates of 5kHz where the initial Taylor microscale Reynolds number was around 30. The full 40960 points of both u- and v-component velocities are shown in Figure 35 Note the qualitative differences in the u- and v-component velocities. [**?**].

Since we are attempting to model the SGS scale terms it is appropriate to filter this signal and curve fit the high-passed information. Additionally, the resulting signal has been low pass filtered to remove any experimental noise. We have used a Gaussian sharp cut-off filter for these purposes, removing the highest and lowest 6 percent of frequencies. The frequency range that we wish to reproduce is that between these values and is assumed to fall

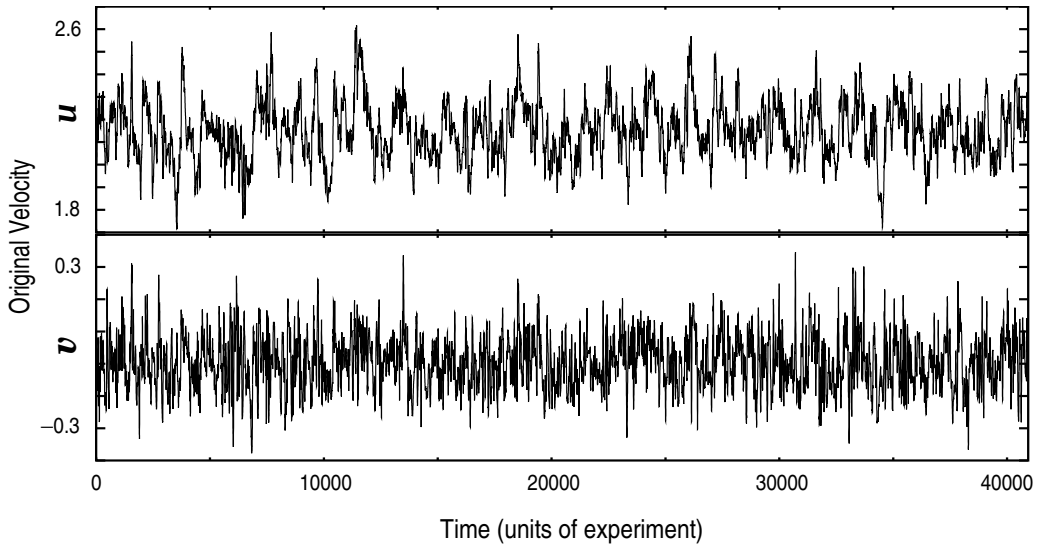

Figure 35: Time series taken from isotropic turbulence experiment.

in the inertial subrange. We will not need to consider the full 40960 points since the model will never calculate such an extensive trajectory without recalculation of the bifurcation parameters and instead concern ourselves with the final 8192 points. Figure 36(a) displays the normalized u- and v-component velocities of this high-low pass filtered signal while Figure 36(b) is a zoomed-in view of the signal from $1000 \leq t \leq 2000$.

In discussing the qualitative appearance of the time signal seen in Figure 36 it is helpful to refer to the characterization parameters that we have previously defined. The intermittencies and correlations of the signal of Figures 36 are qualitative features of this signal that are particularly noticeable. It is seen that the signal is "chaotic" in that multiscale, non-Gaussian behavior is observable. For example, structures such as amplitude peaks that are two to three times the average peak magnitude are common and are often preceded/succeeded by regions of relatively low variation. We should note the qualitative similarities between the u- and v-components of Figure 36 with respect to these structures.

6.4 SYNTHETIC VELOCITIES

In previous attempts at curve fitting chaotic maps to empirical data [118] a complicated function consisting of switching and duration functions, linear combinations of chaotic maps

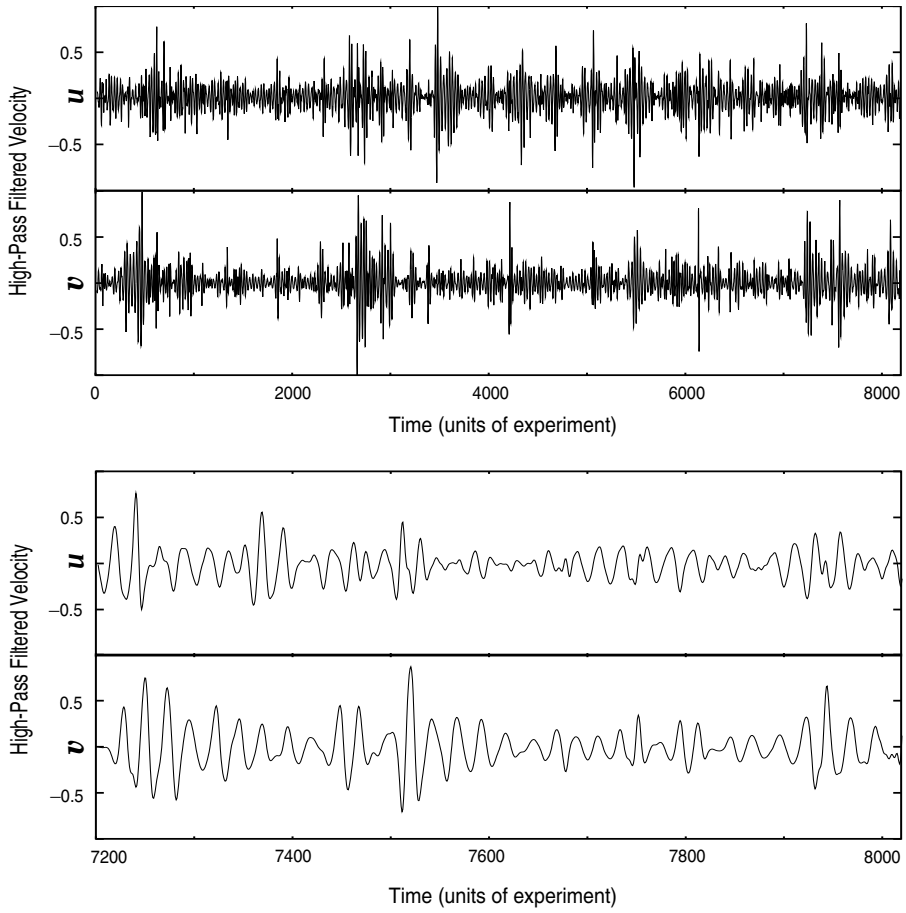

Figure 36: High-pass filtered experimental time series.

at current and previous iterates, and weighting factors was used, and results were quite satifactory. With the advent of the derivation of the PMNS equation from the N.–S. equations it was believed that a simpler and more intuitive approach to data fitting was called for. In the present study we take the position that filtered velocities from empirical data contain multiple wavenumber fluctuations that are subgrid-scale, *modulo* some wavenumber overlapping between the LES and SGS model. With this in mind we have proposed that such multiple wavenumber fluctuations can be modeled with combinations of appropriately weighted instances of the PMNS equation corresponding to the magnitudes of their basis functions in the associated expansions. We note though that this method deviates slightly from the physical situation in the sense that the multiple instances of the PMNS equations are uncoupled where as in the true dynamical system (N.–S. equation) this is not the case.

The first aspect of this framework to consider is that each instance of the PMNS equation used is intended to model oscillations of a specific frequency/wavenumber range. Therefore, specific instances of the PMNS should embody similar frequencies to that frequency range being modeled and therefore should be scaled individually. We will use an arbitrary wavelength stretching parameter for this purpose since the discrete map of Eqns. (41) does not have an inherent physical timescale. In the turbulence model implementation these time scales would be calculated from results of the large scale solution. We will denote the wave-stretching parameter as λ. A λ value of unity is associated with no stretching of the signal and each successive integer value of λ is associated with successive wavelength doublings (interpolations) such that

$$u_i = u_i^*, \tag{49a}$$

$$u_{i+1} = \frac{u_{i+1}^* + u_i^*}{2}, \tag{49b}$$

where u^* indicates the original signal from the PMNS equation, and u denotes the modified signal.

Of course associated with different wavenumber oscillations are individual amplitude factors associated with the Fourier coefficients in the appropriate expansion in wavespace of the signal. Correspondingly we will denote an amplitude factor, α, to be associated with each instance of the PMNS equations used. The general form of the model is then

$$u_n = \sum_{k=1}^{K} \alpha^k M_n^k(\beta_i^k,\, \gamma_{i,j}^k,\, \lambda^k) \tag{50}$$

where k indexes the instances of the PMNS equation used (from 1 to K), M_n^k is the value of the k^{th} instance of the PMNS equation (Eqns. (41)) at the n^{th} iteration as determined by the stretching factor, λ^k, and the bifurcation parameters, β_i^k and $\gamma_{i,j}^k$. As was the case for the time scales, the turbulence model would calculate the needed amplitudes factors using high-pass filtered large-scale solution results. These definitions lead to the need to determine the values of eleven independent parameters per instance of the PMNS equation.

As we have mentioned previously the initial conditions are not considered in this study

and they are chosen arbitrarily ($a^0 = 0.4$, $b^0 = 0.61$, $c^0 = 0.5$). Additionally, each instance of the PMNS equation is executed for 5000 steps before the curve fitting procedure is implemented in an attempt to avoid initial transients of those mappings.

6.5 GENETIC ALGORITHM CURVE FITTING

The method for curve fitting the signal defined by Eqns. (41) and (50) to that in Figure 36 that we have chosen is to optimize the independent parameters of Eqn. (50) by minimizing an objective function related to the characterization parameters outlined previously. This is accomplished through use of a genetic algorithm (GA) code that we will only briefly cover as it is discussed in detail by Yang *et al.* [122].

The genetic algorithm approach borrows its name from Darwin's theory of "survival of the fittest." Fitness in the genetic algorithm curve fitting is viewed in terms of the value of an objective function which is to be maximized, or in this case, minimized. Evaluation of the objective function occurs at each "generation" of the GA. The dependency of fitness on each "individual", or independent parameter, is randomly tested and "natural selection" occurs as unfit "parents" undergo "mutations" so as the "child" will have a better chance of survival. This technique is carried out by the encoding and decoding of bits of binary numbers. The details of this process are beyond the scope of this paper but for more, again, see [122]. Here we are more concerned with the weightings associated with each characterization parameter used in the evaluation of the objective function and in their effects on the overall success of the fit. The nature of these weights is as follows. We let p_i denote the numerical result of computing the value of characterization parameter i and define

$$\delta p_i = p_i^{\text{meas}} - p_i^{\text{model}}, \tag{51}$$

so that we can define a least-squares functional, as in [118], for N_p properties as

$$Q = \sum_{i=1}^{N_p} \phi_i (\delta p_i)^2 \tag{52}$$

where ϕ_i are the weights associated with individual characterization properties.

In previous studies the weights of Eqn. (52) were chosen such that by considering groups of similar properties (with likewise similar parameter values) all groups were dictated to have approximately the same effect on the evaluation of the objective function. It would be helpful, though, if we had sufficient evidence to justify the individual weights used. Presenting such evidence is not the aim of this paper and therefore we will merely report the most successful combination of parameter weightings found over the duration of hundreds of curve fitting experiments.

6.6 RESULTS AND DISCUSSION

In the previous sections we have outlined the methods by which we have performed *a priori* tests of the "poor man's Navier-Stokes" subgrid-scale model. The formulation of Eqns. (41) and (50) allow for the independent selection of eleven parameters per instance of the PMNS equation, each additional instance presumably incorporating a wider range of frequencies and wavenumbers into the model. Therefore, we can perform a basic step-by-step approach to find the minimum number (and thus simplest model) of instances of the PMNS equation that successfully reproduce the dynamics of the high-pass filtered (and presumably subgrid-scale) velocity time series studied here. It would also be of interest to find the maximum amount of filtering allowable such that the PMNS SGS model can still recover the physics of the filtered information. Such a procedure could also be considered in terms of Reynolds' averaging techniques but is not performed here.

Of course, as most of the parameters discussed in section 6.2 and used by McDonough *et al.* [118] are classical statistical properties there is a many-to-one mapping from time series realizations to parameter values. Unfortunately we have found that often times minimization of the objective function where these statistical properties are heavily weighted leads to unrealistic time series (bad fits). From further numerical experiments we have found that favorable results are seen as a result of weighting the "dynamical" parameters, such as crossing points, intermittencies, burst delay times and mean oscillation variances, more heavily. As in the case of the Poincaré mapping discussed previously, dynamical variables act to decrease the dimension of the given signal reducing the ratio of the many-to-one mapping

described above thus increasing likelihood of success in curve fitting. These principles are often used in recreating attractors from noisy data sets using singular value decomposition or other methods (see, *e.g.*, Grassberger *et al.* [123] or Kostelich and Schreiber [124]).

6.6.1 One Instance of the PMNS Equation, $K = 1$

Referring back to the target time series of Figure 36 we note that multiscale behavior seen there suggests multiple wavenumber fluctuations that will make an accurate fit using only one instance of the PMNS equation difficult. This case, though, would be ideal from a theoretical standpoint as it would require determination of the minimum number of unknown constants. It is also a good case to test procedures concerning weighting of characterization parameters in the evaluation of the objective function of the genetic algorithm.

Here we would like to succinctly summarize our results. First, for comparison, we present, in Figure 37 the experimental time series and PMNS time series side-by-side at a number of different magnifications, along with the power spectra, for both the u-component and v-component velocities. In parts (a) and (b) of this figure are time series corresponding to u- and v-component velocities, respectively. Each time series plot is divided into two halves. On the left-half of each is the plot of some portion of the experimental (high-pass filtered) signal and on the right-half is a plot of an equal length segment of the time series corresponding to the result of the curve fitting procedure when executed for over 100,000 generations of the genetic algorithm. In parts (c) and (d) we present the same family of plots only zoomed-in on a portion of those plots of parts (a) and (b). Parts (e) and (f) are in turn magnifications of parts (c) and (d). In parts (g) and (h) we present comparisons of the power spectra calculated from the last 8192 points of the time series corresponding to the experimental data and the result of the curve fitting algorithm.

The first thing to note concerning the time series shown in Figure 36 is that only 1 instance of the PMNS equation captures a great deal of the dynamics of the small-scales, even though we have filtered out fluctuations from only the lowest 6% of wavenumbers. This bodes very well for the ATD/PMNS procedure in general as calculation of model parameter values using the inertial range information found from high-pass filtering of grid-scale results is somewhat computationally expensive, and we would prefer to perform such a procedure

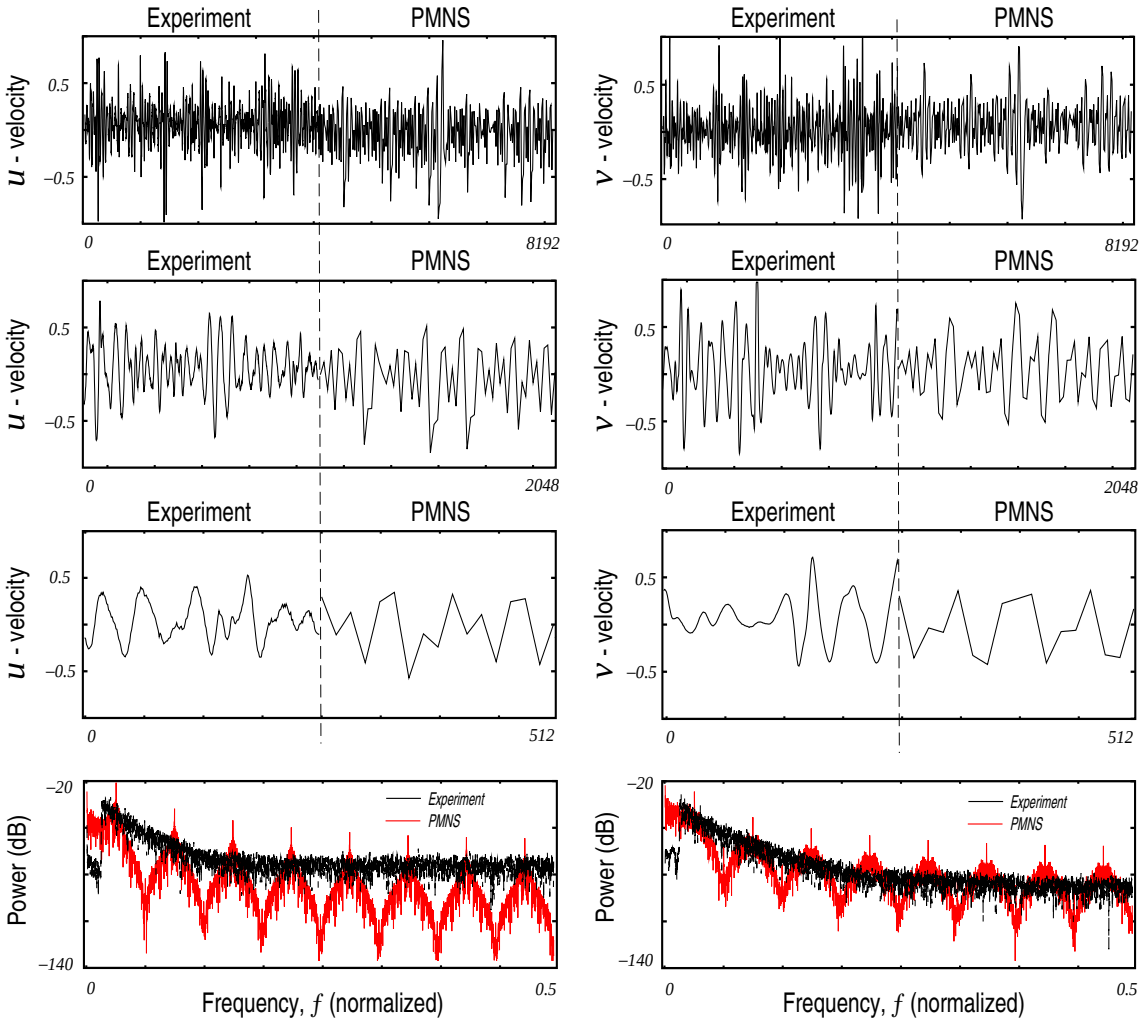

Figure 37: Results of curve fitting procedure for one instance of the PMNS equation.

only once. On the other hand, there are differences in the dynamics of the time series as can be seen at all three levels of magnification. First there is the obvious lack of as many bursting structures in the PMNS time series as can be seen from parts (a) and (b). Second large fluctuations appear to have a greater wavelength in the PMNS time series than in the experimental time series. Third fine-scale structure that is seen in the experimental time series is, somewhat, missing from the PMNS time series, as is most obvious in parts (e) and (f).

In discussing the power spectra of parts (g) and (h) let us first note that power spectra corresponding to the experimental data are shown in green and the power spectra corre-

sponding to the PMNS result are shown in red. Secondly we note that there are still visible low power fluctuations at the low wavenumbers that we have already sharp-cut filtered. This behavior is due to the normalization of time series data to $[-1:1]$ that we have performed, after the initial high-pass filtering, so that the curve fitting procedure is more straightforward. Third we note the sharp spectral peaks seen in the power spectra of the PMNS time series but not in those corresponding to the experimental data (which show a power law decay as they should). These are due to the fashion in which we have stretched the PMNS time series, *viz.*, discrete, evenly spaced, interpolation, and are not indicative of the type of behavior the PMNS equation alone would produce at the bifurcation parameters chosen by the genetic algorithm. In fact the PMNS behavior is strictly broadband without fundamental in this case.

6.6.2 Two Instances of the PMNS Equation, $K = 2$

In the present section we consider the case where we have used two instances of the PMNS, as proposed in Section 6.4, to produce time series. Figure 38 is analogous to that seen in the previous section (Figure 37) and contains results from the curve fitting algorithm when using two instances of the PMNS equation.

From the time series comparisons we see that much improvement is seen from the previous case. For instance, the high magnitude fluctuations are of approximately the same wavelength and are beginning to show intermittent qualities similar to that of the experimental data. In addition, small-scale fluctuations are seen, though their magnitude is still somewhat larger than for the experimental time series. But, as we can see most clearly in parts (c) and (d), the additional instance of the PMNS equation has allowed for a greater number of high frequency, moderate magnitude fluctuations than are seen in the experimental time series. The PMNS power spectra show better correlation with the experimental power spectra than in the previous case, but still much improvement can be made.

6.6.3 Three Instances of the PMNS Equation, $K = 3$

We expect that as we continue to add instances of the PMNS equation we will continue

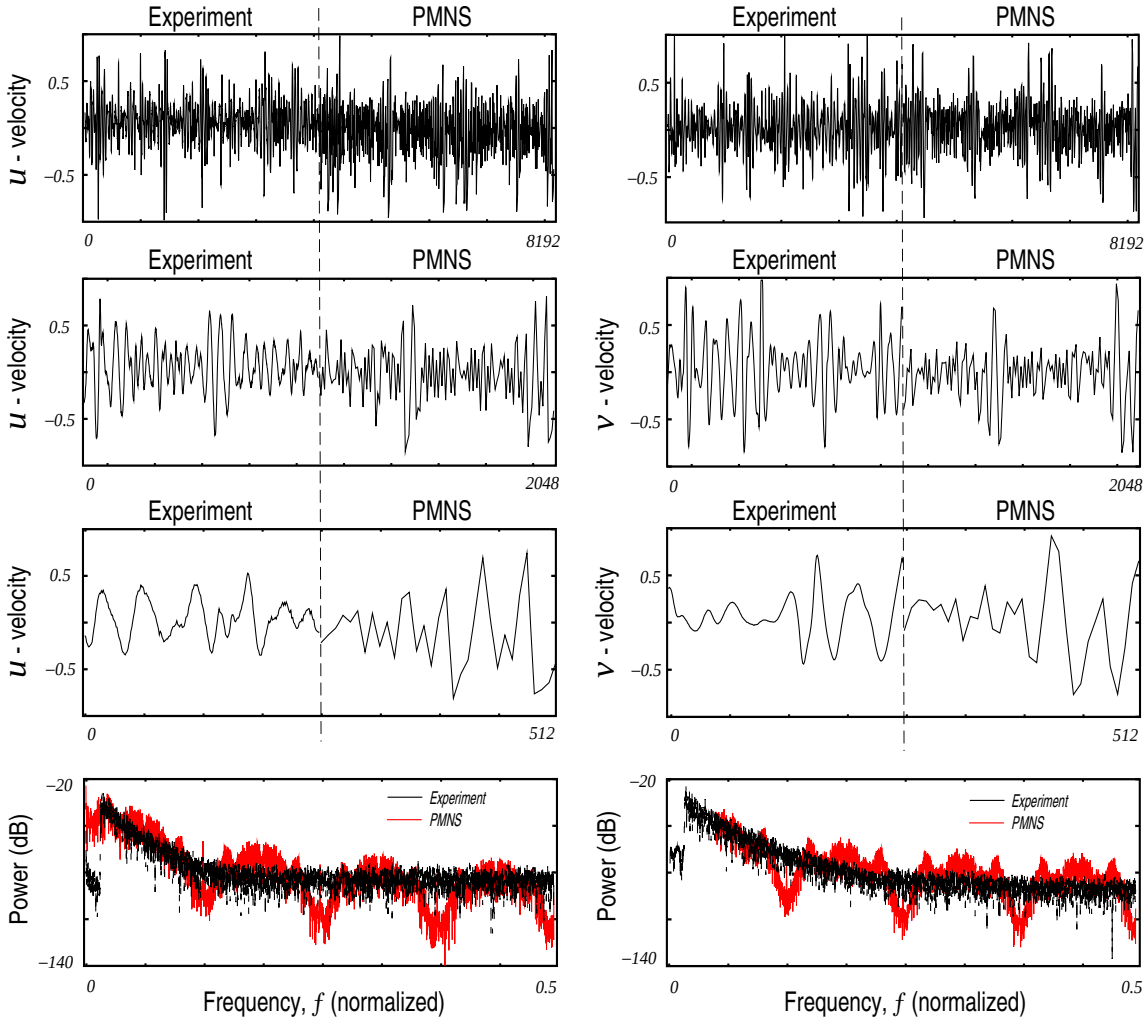

Figure 38: Results of curve fitting procedure for two instances of the PMNS equation

to see improvement in the qualitative likeness between the time series from results of the curve fitting algorithm and the experimental data. This hypothesis is confirmed in the results presented in Figure 39 comparing the time series and power spectra found using three instances of the PMNS equation and those of experimental data.

We see in Figure 39(a)–(f) time series comparisons that are an improvement upon the last case in a number of ways. First the intermittencies more closely resemble those of the experiment. Secondly the high frequency, moderate magnitude fluctuations that were too prevalent in the previous case have been dampened and fluctuations are generally of the approximate magnitude and duration as those seen for the experimental data. In addition

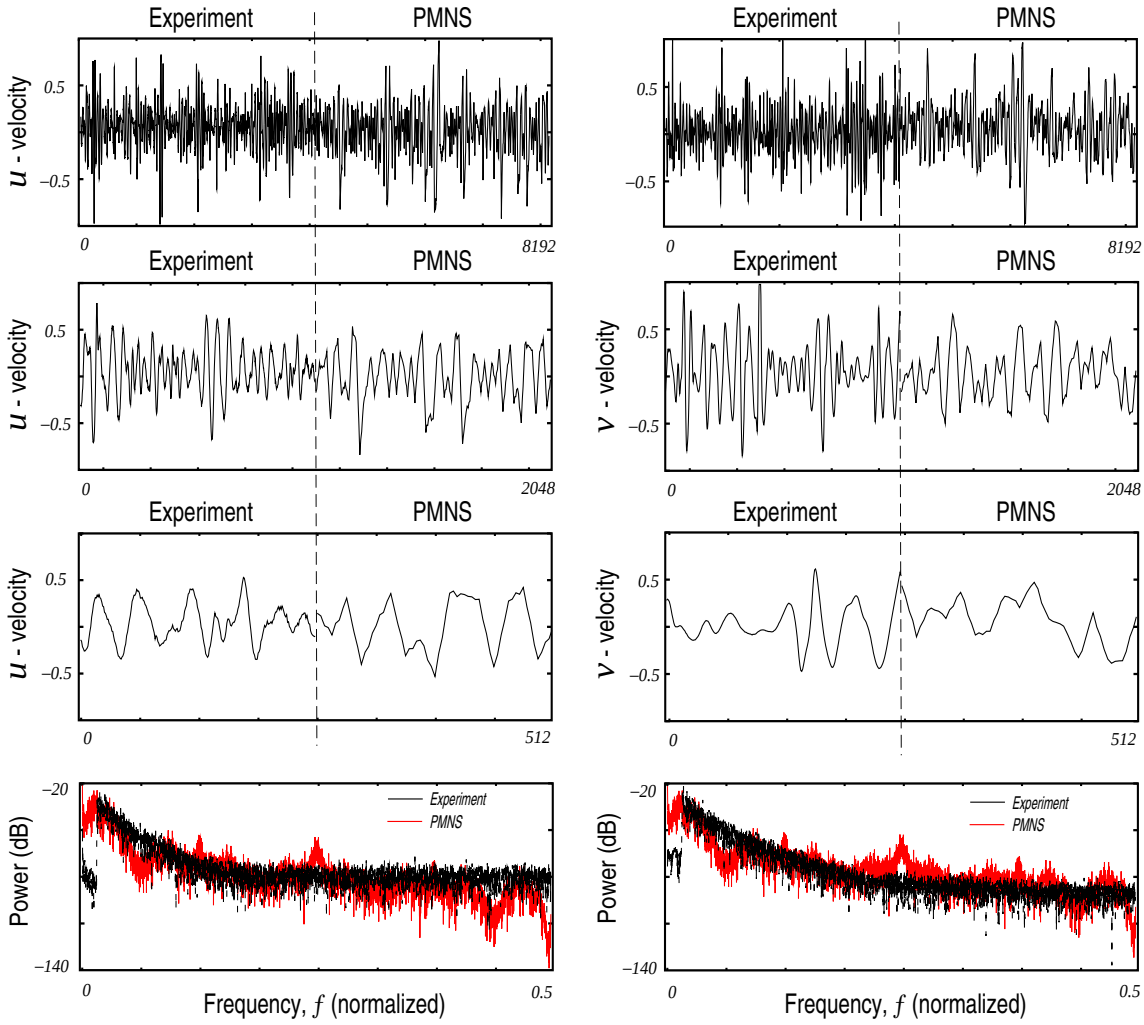

Figure 39: Results of curve fitting procedure for three instances of the PMNS equation.

extremely fine-scale structures can be seen (see, *e.g.*, Figure 38(e)) that were absent in the previous two cases. The power spectra are indicators of these improvements as they show a high level of correlation over a large range of wavenumbers. It is also seen that the power spectra of the PMNS equation results show a marked drop in power at the cutoff frequency, as we would hope.

6.6.3 Four Instances of the PMNS Equation, $K = 4$

Further increases in the number of instances of the PMNS equations used result in proportionately smaller improvements in the results. For instance, Figure 40(a)-(h) shows com-

parisons of the results from using 4 instances of the PMNS equations and experimental data.

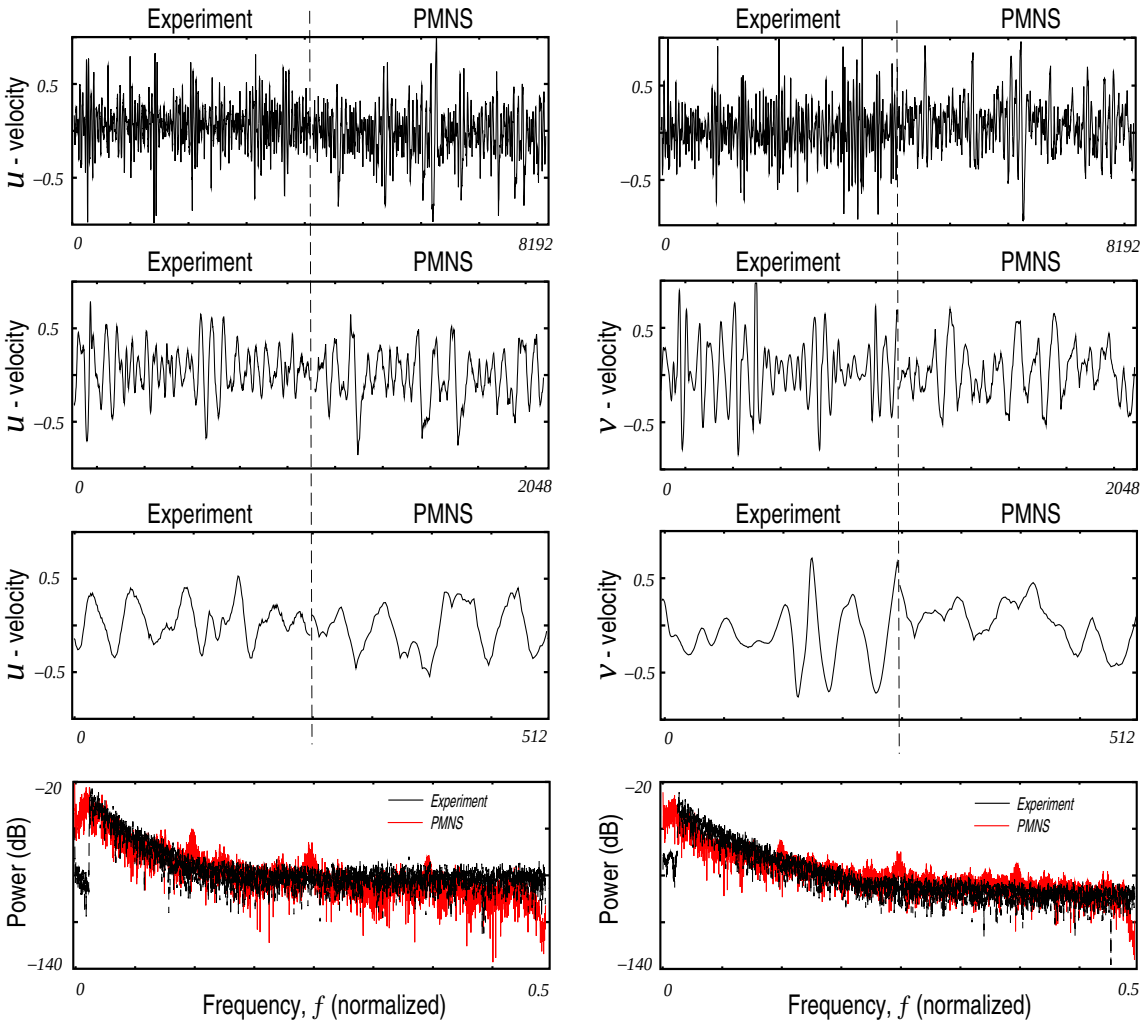

Figure 40: Results of curve fitting procedure for four instances of the PMNS equation

Both the time series of parts (a)–(f) and the power spectra of parts (g) and (h) show slight improvement over those presented in the previous section for three instances of the PMNS equation. The time series show acceptable levels of intermittency, wavelength magnitudes, and fine-scale structure. In fact, the fit seems to be equally good when viewing the highest level of magnification (parts (e) and (f)) as it does when viewing almost the entire time series (parts (a) and (b)). The power spectra display similar decay rates to that of the experiment and similar magnitudes throughout the spectrum of wavenumbers. Peaks are still seen at the

main harmonics caused by the stretching procedure and we assume that these are present because the curve fitting algorithm is attempting to reproduce the drop in magnitude at low wavenumber due to the sharp-cutoff filtering.

VII. SUMMARY AND CONCLUSIONS

This study has been focused primarily on numerical investigations of a novel turbulence subgrid-scale model while partially concerned with the theory behind its implementation. As such, in Chapters I and II background information was provided so that the reader could understand the motivation behind this work as much as possible. Included were relevant reviews of previous work in turbulence simulations, including the field of subgrid-scale models known as synthetic velocities, and a summary and discussion of the additive turbulent decomposition method for which the synthetic velocity model presented here was first proposed for use, though it could also be used in large-eddy simulations and even possibly Reynolds' averaged Navier-Stokes procedures. The advantages of the combined ATD-synthetic velocity procedure were noted to be threefold:

1) Filtering is performed on the solutions to the Navier-Stokes equations as opposed to the equations themselves; thus the grid-scale equations to be solved are consistent with the Navier-Stokes equations given a valid subgrid-scale synthetic velocity model is used.

2) The procedure makes use of the subgrid-scale model results to enhance the wavenumber content of the simulations, as opposed to discarding the model information as is done in RANS and most LES formulations.

3) The "Poor Man's Navier-Stokes" synthetic velocity model is a valid model of Navier-Stokes physics, specifically one in which all of the parameter values are shown to be directly related to N.–S. physics and can be calculated from grid-scale results, as opposed to a model of flow statistics.

Concerning the last of these advantages Chapter III was dedicated to the derivation of the 3-D PMNS equation SGS model from the N.–S. equations. This derivation has provided the necessary relations between model parameters and physics to make this endeavor justifiable. In fact, the material in Chapters II and III is practically all that is needed to correctly employ this turbulence simulation technique, though details of implementation are left to future studies.

In Chapter IV we began the detailed study of the PMNS synthetic velocity model with numerical investigations of the 2-D PMNS equation for a number of cases. Specifically we

first looked at the case where $\gamma_u = \gamma_v = 0$ which simplifies to the an uncoupled set of logistic maps. We then progressed in the study by investigating the behaviors seen when it was required that $\beta_u = \beta_v$ and $\gamma_u = \gamma_v$, including detailed studies of the observed transitions to chaos, strange attractors, and effects of initial conditions. Notably we found that equated initial conditions lead to spurious solutions and concluded their use should be avoided. In addition we have found many other interesting phenomena that are discussed including self-similarity of time series and coexistent multiple symmetric strange attractors. In the final sections of this chapter we studied the effects of uncoupling the bifurcation parameter values. Evidence of the existence of threshold values of the primary bifurcation parameters, β_u and β_v, for which if either or both β were in excess of this value chaos was likely to occur independent of the values of the remaining bifucation parameters, was seen in all of these cases. It is proposed that these values, along with those β values for which divergence is always seen, be used as limits on the values of these parameters in the implementation of the SGS model, *i.e.*, $-2 \leq \beta \leq -1$ and/or $3 \leq \beta \leq 4$. In contrast the γ values generally affected the bifurcation sequences and solution behavior in subtler ways. It was seen, though, that high values of the γs produced unique chaotic regimes frequently for βs < 0 and, conversely, low values of the γs exhibit chaos for βs > 0. Still, more work needs to be done, possibly in the form of full-scale implementation of the model, before appropriate restrictions can be placed on the γs. As of now we would propose to apply the commonly used range $-3 \leq \gamma \leq 3$ which accounts for most of the interesting behaviors seen but also encompasses a large range of nondivergence.

In Chapter V we studied the 3-D PMNS equation. Drawing inferences from numerical evidence shown here it was concluded that the 3-D equation could be expected to behave in a qualitatively similar manner to that seen in the previous chapter for the 2-D equation. Specifically the ranges of the main bifurcation parameters that were seen to produce chaos in a few simplified forms of the 3-D equation appeared to be the same as those found for the 2-D equation. An exception to this rule was noted, however, when it was seen that high values of γ rarely produced anything other than divergence in the 3-D case. An example of an interesting attractor was presented that was calculated using bifurcation parameters that could be associated strictly with the noninteresting range of βs between -1 and 3, calling

into question the assumption that it might be appropriate to restrict the values of β to the ranges $[-2, 1]$ and $[3, 4]$.

Chapter VI was concerned with the *a priori* testing of the ability of the PMNS equation model to produce turbulent like fluctuations. This was accomplished through the use of a genetic algorithm search to find optimal bifurcation parameters that, when implemented in the model, produced an accurate "fit" of experimental turbulence data, as determined by the minimization of a least squares functional containing values for both cases of time series characterization parameters. Results were found to agree with the hypothesis presented that use of multiple instances of the PMNS equation would improve such a fit by their inclusion of multiple wavenumber fluctuations corresponding to increasing the number of "shells" included in the shell model of the Navier-Stokes equations given in Chapter III. The best results were achieved for 3 and 4 instances of the PMNS equation although the results when using only one instance were sufficiently good to merit optimism concerning the possiblity of using an isolated instance in model implementation, thus minimizing the required arithmetic.

References

[1] Wilcox, D. C., *Basic Fluid Mechanics*, DCW Industries, La Cañada, CA, 1998.

[2] Aris, R., *Vectors, Tensors, and the Basic Equations of Fluid Mechanics*, Dover, New York, 1989.

[3] Panton, R. L., *Incompressible Flow*, John Wiley and Sons, Inc., New York, 1996.

[4] Richter, J. P., *The Notebooks of Leonardo da Vinci*, Dover, New York, 1970.

[5] Frisch, U., *Turbulence, The Legacy of A. N. Kolmogorov*, Cambridge Univ. Press, Cambridge, 1995.

[6] Rouse, H., and Ince, S., *History of Hydraulics*, Dover, New York, 1963.

[7] Tsinober, A., *An Informal Introduction to Turbulence*, Kluwer Academic Publishers, The Netherlands, 2001.

[8] Boussinesq, J., *Theorie de l'écoulement Tourbillant*, Acad. Sci., Paris, 1877.

[9] Lumley, J. L., "Some comments on turbulence," *Phys. Fluids A*, **4**, pp. 203–211, 1992.

[10] Reynolds, O., "On the Dynamical Theory of Incompressible Viscous Fluids and the Determination of the Criterion," *Phil. Trans. Royal Soc. London*, **186**, pp. 123–164, 1895.

[11] Libby, P. A., *Introduction to Turbulence*, Taylor and Francis, New York, 1996.

[12] von Karman, T., "The fundamentals of the statistical theory of turbulence," *J. Aero. Sci.*, **4**, pp. 131–138, 1937. Reprinted in *Centennial of Powered Flight: A Retrospective of Aerospace Research*, AIAA J. Supplement, 41, 2003.

[13] Taylor, G. I., "Statistical theory of turbulence, I, II, III and IV" *Proc. Roy. Soc. London A*, **151**, pp. 421–478, 1935.

[14] Kolmogorov, A. N., "The local structure of turbulence in an incompressible viscous fluid at very high Reynodls numbers," *C. R. (Doklady) Akad. Nauk SSSR*, **30**, pp.

301–305, 1941. Reprinted in *Proceedings: Mathematical and Physical Sciences*, **434**, Turbulence and Stochastic Process: Kolmogorov's Ideas 50 Years On, 1991.

[15] Kolmogorov, A. N., "On degeneration of isotropic turbulence in an incompressible viscous liquid," *C. R. (Doklady) Akad. Nauk SSSR*, **31**, pp. 538–540, 1941.

[16] Kolmogorov, A. N., "Dissipation of energy in locally isotropic turbulence," *C. R. (Doklady) Akad. Nauk SSSR*, **32**, pp. 16–18, 1941. Reprinted in *Proceedings: Mathematical and Physical Sciences*, **434**, Turbulence and Stochastic Process: Kolmogorov's Ideas 50 Years On, 1991,

[17] Obukhov, A. M., "On the distribution of energy in the spectrum of turbulent flow," *C. R. (Doklady) Akad. Nauk SSSR*, **32**, pp. 22–24, 1941.

[18] Prandtl, L., "Bericht über Untersuchungen zur ausgebildeten turbulenz," *Zeitschrift für Angewandte Mathematik und Mechanik*, **5**, pp. 136–139, 1925.

[19] Landau, L. D. and Lifshitz, E. M., *Fluid Mechanics*, 1^{st} edition, Pergamon Press, Oxford, 1959.

[20] Kraichnan, R. H., "The structure of isotropic turbulence at very high Reynolds numbers," *J. Fluid Mech.*, **5**, pp. 497–543, 1959.

[21] Kraichnan, R. H., "Isotropic turbulence and inertial-range structure," *Phys. Fluids*, **8**, pp. 1728–1752, 1966.

[22] Batchelor, G. K., *The Theory of Homogeneous Turbulence*, Cambridge University Press, London, 1967.

[23] Saffman, P. G., "The large scale structure of homogeneous turbulence," *J. Fluid Mech.*, **27**, pp. 581–593, 1967.

[24] Monin, A. S. and Yaglom, A. M., *Statistical Fluid Mechanics: Mechanics of Turbulence*, MIT Press, Cambridge, MA, 1971.

[25] Tennekes, H. and Lumley, J., *A First Course in Turbulence*, MIT Press, Cambridge, MA, 1972.

[26] Ruelle, D. and Takens, F., "On the nature of turbulence," *Comm. Math. Phys.*, **20**, 1971, pp. 167–192.

[27] "homogeneous." Def. 2. *Webster's New World Dictionary of the American Language.* 2^{nd} College ed. 1974.

[28] "isotropic." Def. 1. *Webster's New World Dictionary of the American Language.* 2^{nd} College ed. 1974.

[29] Richardson, L. F., *Weather Prediction by Numerical Process*, Cambridge University Press, Cambridge, 1922.

[30] Kolmogorov, A. N., "A refinement of previous hypotheses concerning the local structure of turbulence in a viscous incompressible fluid at high Reynolds numbers," *J. Fluid Mech.*, **13**, pp. 82–85, 1962.

[31] Obukhov, A. M., "Some specific features of atmospheric turbulence," *J. Fluid Mech.*, **13**, pp. 77–81, 1962.

[32] Wilcox, D. C., *Turbulence Modeling for CFD*, Second Edition, DCW Industries, La Cañada, CA, 1998.

[33] Prandtl, L., "Bericht über Untersuchungen zur ausgebildeten Turbulenz," *Z. Angew. Math. Mech.*, **5**, pp. 136–139, 1925.

[34] Cebeci, T. and Smith, A. M., *Analysis of turbulent boundary layers,* Ser. in Appl. Math. Mech., **15** Academic Press, 1974.

[35] Spalart, P. R. and Allmaras, S. R., "A one-equation model for aerodynamic flows," *AIAA Paper.*, **92-439**, Reno, Nevada, 1992.

[36] Spalart, P. R., "Strategies for turbulence modelling and simulation," *Int. J. Heat and Fluid Flow*, **21**, pp. 252–263, 2000.

[37] Wilcox, D. C., "Reassessment of the scale determining equation for advanced turbulence models," *AIAA Journal*, **26**, pp. 1299–1310, 1988.

[38] Launder, B. E., Reece, G. J., and Rodi, W., "Progress in the development of a Reynolds-stress turbulence closure," *J. Fluid Mech.*, **68**, pp. 537–566, 1975.

[39] McDonough, J. M., "On intrinsic errors in turbulence models based on Reynolds-averaged Navier-Stokes equations," *Fluid Mech. Res.*, **22**, pp. 27–55, 1995.

[40] Fox, D. G., and Lilly, D. K., "Numerical simulation of turbulent flows," *Rev. Geophys. Space Phys.*, **10**, pp. 51–72, 1972.

[41] Moin, P., and Mahesh, K., "Direct Numerical Simulation: A tool in turbulence research," *Ann. Rev. Fluid Mech.*, **30**, pp. 539–578, 1998.

[42] Siggia, K., "Numerical study of small-scale intermittency in three-dimensional turbulence," *J. Fluid. Mech.*, **107**, pp. 375–406, 1981.

[43] Huang, M.-J. and Leonard, A., "Velocity autocorrelations of decaying isotropic homogeneous turbulence," *Phys. Fluids*, **7**, pp. 2455–2464, 1995.

[44] Kim, J., Moin, P., and Moser, R. D., "Turbulence statistics in fully-dveloped channel flow at low Reynolds number," *J. Fluid Mech.*, **177**, pp. 133–166, 1987.

[45] Moin, P., Shih, T.-H., Driver, D., and Mansour, N. N., "Direct numerical simulation of a three-dimensional turbulent boundary layer," *Phys. Fluids A*, **2**, pp. 1846–1853, 1990.

[46] Le, H., and Moin, P., "Direct numerical simulation of turbulent flow over a backward-facing step," *Ann. Rev. Fluid Mech.*, **30**, pp. 539–578, 1998.

[47] Lee, S., Lele, S. K., and Moin, P., "Eddy shocklets in decaying compressible turbulence," *Phys. Fluids*, **4**, pp. 657–664, 1991

[48] Samtaney, R., Pullin, D. I., and Kosović, B., "Direct numerical simulation of decaying compressible turbulence and shocklet statistics," *Phys. Fluids*, **13**, pp. 1415–1430.

[49] Siggia, K., "Direct Numerical Simulation: A tool in turbulence research," *Ann. Rev. Fluid Mech.*, **30**, pp. 539–578, 1998.

[50] Lesieur M., and Métais, O., "New trends in large-eddy simulations of turbulence," *Ann. Rev. Fluid Mech.*, **28**, pp. 45–82, 1996.

[51] Rogallo, R. S., and Moin, P., "Numerical simulation of turbulent flows," *Ann. Rev. Fluid Mech.*, **16**, pp. 99–137, 1996.

[52] Lesieur, M., *Turbulence in Fluids*, 3^{rd} Ed., Kluwer Academic, Dordrecht, 1997.

[53] Deardorf, J. W., "A numerical study of three-dimensional turbulent channel flow at large Reynolds numbers," *J. Fluid Mech.*, **41**, pp. 453–480, 1970.

[54] Leonard, A., "Energy cascade in large-eddy simulations of turbulent fluid flows," *Adv. Geophys. A*, **18**, pp. 237–248, 1974.

[55] Chollet, J.-P., and Lesieur, M., "Parametrization of small scales of three-dimensional isotropic turbulence utilizing spectral closures," *J. Atmos. Sci.*, **38**, pp. 2747–2757, 1981.

[56] Piomelli, U., "Large-eddy Simulation: Achievements and challanges," *Prog. Aerospace Sci.*, **35**, pp. 335–362, 1999.

[57] Smagorinsky, J., Manabe, S., and Holloway, J. L., "Numerical Results from a Nine-Level General Circulation Model of the Atmosphere," *Monthly Weather Rev.* **93**, pp. 727–768, 1965.

[58] Germano, M., Piomelli, U., Moin, P., and Cabot, W. H., "A Dynamic Subgrid Scale Eddy Viscosity Model" *Phys. Fluids*, **A3**, pp. 1760–1765, 1991.

[59] Meneveau, C., and Katz, J., "Scale-invariance and turbulence models for large-eddy simulation," *Ann. Rev. Fluid Mech.*, **32**, pp. 1–32, 2000.

[60] Lorenz, E. N., "Deterministic nonperiodic flow," *J. Atmos. Sci.*, **20**, pp. 130–141, 1963.

[61] Poincaré, H., *Les Methodes Nouvelles de la Mechanique Celeste. Vol. I and II.* Gauthier-Villars, Paris, 1897.

[62] Aubin, D., and Dalmedico, A. D., "Writing the History of Dynamical Systems: *Longue durée* and revolutions, discipline, and culture," *Historia Mathematica*, **29**, pp. 273–339, 2002.

[63] Leray, J., "Sur le mouvement d'un liquide visueux emplissant l'espace," *Acta Math.*, **63**, pp. 193–248, 1934.

[64] Yorke, J. A. and Yorke, E. D., "Chaotic behavior and fluid dynamics," in *Hydrodynamic Instabilities and the Transition to Turbulence*, Swinney and Gollub (eds), pp. 77–84, Springer-Verlag, Berlin, 1981.

[65] Smale, S., "Differentiable dynamical systems," *Bull. Am. Math. Soc.*, **73**, pp. 747–817, 1967.

[66] Newhouse, S., Ruelle, D. and Takens, F., "Occurrence of strange axiom A attractors near quasiperiodic flows on T^m, $m \geq 3$," *Commun. Math. Phys.*, **64**, pp. 35–40, 1978.

[67] Feigenbaum, M. J., "Quantitative universality for a class of nonlinear transformations," *J. Stat. Phys.*, **19**, pp. 25–52.

[68] Feigenbaum, M. J., "The onset spectrum of turbulence," *Phsy. Lett. A*, **74**, pp. 375–378.

[69] Pomeau, Y., and Manneville, P., "Intermittent transition to turbulence in dissipative dynamical systems," *Commun. Math. Phys.*, **74**, pp. 189–197, 1980.

[70] Gollub, J. P., and Swinney, H. L., "Onset of turbulence in a rotating fluid," *Phys. Rev. Lett.*, **35**, pp. 927–930, 1975.

[71] Gollub, J. P. and Benson, S. V., "Many routes to turbulent convection," *J. Fluid Mech.*, **100**, pp. 449–470, 1980.

[72] Alligood, K. T., Yorke, J. A., and Sauer, T. D., *Chaos, An Introduction to Dynamical Systems*, 1996.

[73] Ruelle, D., *Chaotic Evolution and Strange Attractors*, Cambridge University Press, Cambridge, 1989.

[74] Eckmann, J.-P., "Roads to turbulence in dissipative dynamical systems," *Rev. Mod. Phys.*, **53**, pp. 643–654, 1981.

[75] Eckmann, J.-P. and Ruelle, D., "Ergodic theory of chaos and strange attractors," *Rev. Mod. Phys.*, **57**, pp. 617–656, 1985.

[76] McDonough, J. M., Bywater, R. C., and Buell, J. C., "An investigation of strange attractor theory and small-scale turbulence," *AIAA Paper*, 84-1674, June, 1984.

[77] McDonogh, J. M. and Bywater, R. J., "Large-scale effects on local small-scale chaotic solutions to Burgers' equation," *AIAA J.*, **24**, pp. 1924-1930, 1986.

[78] J. A. Domaradzki and N. A. Adams, "Direct modeling of subgrid scales of turbulence in large-eddy simulatins," *J. Turbulence* **3**, 1–19, 2002.

[79] P. Sagaut, *Large-Eddy Simulation for Incompressible Flows*, Springer-Verlag, Berlin, 2001.

[80] Domaradzki, J. A. and Saiki, E. M., "A subgrid-scale model based on the estimation of unresolved scales of turbulence," *Phys. Fluids* **9**, pp. 2148–2164, 1997.

[81] Kerstein, A. R., Ashurst, W., Wunsch, S. and Nilsen, V., "One-dimensional turbulence: vector formulation and application to free shear flows," *J. Fluid Mech.* **447**, pp. 85–109, 2001.

[82] Menon, S. and Kerstein, A. R., "Stochastic simulation of the structure and propagation rate of turbulent premixed flames," *Proc. Combust. Inst.* **24**, pp. 443–450, 1992.

[83] Scotti, A. and Meneveau, C., "A fractal model for large-eddy simulation of turbulent flow," *Physica D* **127**, pp. 198–232, 1999.

[84] Foias, C., Manley, O., and Temam, R., "Modeling of the interaction of small and large eddies in two-dimensional turbulent flows," *Math. modeling Numer. Anal.*, **22**, pp. 93–118, 1988.

[85] Brown, R. M., Perry, P., and Shen, Z., "The additive turbulent decomposition for the two-dimensional incompressible Navier-Stokes equations: Convergence theorems and error estimates," *SIAM J. Appl. Math.*, **59**, pp. 139–155, 1998.

[86] Yang, Y. and McDonough, J. M., "Bifurcation studies of Navier–Stokes equations via additive turbulent decomposition," in *Bifurcation Phenomena and Chaos in Thermal Convection*, Bau *et al.* (eds), ASME-HTD, **214**, ASME, New York, 1992.

[87] Hylin, E. C. and McDonough, J. M., "Derivation of projection methods from integration of the Navier-Stokes equations," *J. Comput. Appl. Math.*, **81**, pp. 349–374, 1997.

[88] Hylin E. C. and McDonough, J. M., "Chaotic small-scale velocity fields as prospective models for unresolved turbulence in an additive decomposition of the Navier–Stokes equations," *Int. J. Fluid Mech. Res.* **26**, pp. 539–567, 1999.

[89] McDonough, J. M. and Wang, D., "Additive turbulent decomposition: A highly parallelizable turbulence simulation technique," in *Parallel Compuational Fluid Dynamics: New Algorithms and Applications*, Satofuka, N., Periaux, J., and Ecer A. (eds), Elsevier Acience, New York, Amsterdam, 1995.

[90] Constantin, P. and Foias, C., *Navier–Stokes Equations*, University of Chicago Press, Chicago, 1988.

[91] McDonough, J. M., Yang, Y. and Hylin, E. C., "Modeling time-dependent turbulent flow over a backward-facing step via additive turbulent decomposition and chaotic maps," in *Proceedings of First Asian Computational Fluid Dynamics Conference*, Hui, Kwok & Chasnov (Eds.), Hong Kong University of Science and Technology, Hong Kong, 747–752, 1995.

[92] McDonough, J. M., Garzon, V. E. and Schulte, D. E., "Effect of film-cooling hole location on turbulator heat transfer enhancement in turbine blade internal air-cooling circuits," presented at *ASME TURBO EXPO 99*, Indianapolis, IN, June 7–10, 1999.

[93] Hylin, E. C., *A Stochastic Model for Small-Scale Turbulence*, Ph. D. Dissertation, University of Kentucky Department of Mechanical Engineering, 1997.

[94] McDonough, J. M. and Huang, M. T., "A low-dimensional model of turbulence–chemical kinetics interactions," in *Proc. Third Int. Symp. Scale Modeling*, Nagoya, Japan, Sept. 10–13, 2000. Available for download at www.engr.uky.edu\~acfd

[95] Bohr, T., Jensen, M. H., Paladin, G. and Vulpiani, A., *Dynamical Systems Approach to Turbulence*, Cambridge University Press, Cambridge, 1998.

[96] Gledzer, E. B., "System of hydrodynamic type admitting two quadratic integrals of motion", *Sov. Phys. Dokl.*, **18**, pp. 216–217, 1973.

[97] Ohkitani, K. and Yamada, M., "Temporal intermittency in the energy cascade process and local Lyapunov analysis in fully developed model of turbulence", *Progr. Theor. Phys.*, **81**, pp. 329–341, 1989.

[98] May, R. M., "Simple mathematical models with very complicated dynamics" *Nature*, **261**, 1976, pp. 459–467.

[99] Yang, T., Xu, Y., McDonough, J. M., and Tagavi, K. A., "Local discrete operator interpolation solution of the phase-field model," presented at *ASME Int. Mech. Engr. Cong. 2002*, New Orleans, LA, November 17-22, 2002. Available for download at www.engr.uky.edu\~acfd

[100] Xu, Y., Yang, T., McDonough, J. M., and Tagavi, K. A., "A discrete-operator interpolation solution of the phase-field model," presented at *AIAA Thermophysics and Heat Transfer Meeting*, St. Louis, MO, June 24–27, 2002. Available for download at www.engr.uky.edu\~acfd

[101] McDonough, J. M., "A 'synthetic scalar' subgrid-scale model for large-eddy simulation of turbulent combustion," Proc. 2002 Spring Tech. Mtg. Central States Sec., Combust. Inst., Knoxville, TN, April 7-9, 2002. Available for download at www.engr.uky.edu\~acfd

[102] McDonough, J. M. and Huang, M. T., "A 'poor man's Navier–Stokes equation': derivation and numerical experiments–the 2-D case", Accepted to *Int. J. Numer. Meth. Fluids*, 2003. Available for download at www.engr.uky.edu\~acfd

[103] Verhulst, P. F., "Recherches mathmatiques sur la loi d'accroissement de la population" *Nouv. mm. de l'Academie Royale des Sci. et Belles-Lettres de Bruxelles*, **18**, pp. 1–41, 1845.

[104] Feigenbaum, M. J., "The universal metric properties of nonlinear transformations", *J. Stat. Phys.*, **21**, pp. 669–706, 1979.

[105] Lanford, O. E. III., "A shorter proof of the existence of the feigenbaum fixed point," *Commun. Math. Phys.*, **96**, pp 521-538, 1984.

[106] Devaney, R. L., *An Introduction to Chaotic Dynamical Systems*, Addison-Wesley, Redwood City, CA, 1987.

[107] Takens, F., "Detecting strange attractors in turbulence", In *Lecture Notes in Mathematics, **898**, Dynamical systems and turbulence*, Rand and Young (eds), pp. 366-381, Springer, Berlin, 1981.

[108] Mandelbrot, B. B., *The Fractal Geometry of Nature*, 2nd edition, W. H. Freeman and Co., San Francisco, California, 1982.

[109] Bible, S. A. and McDonough, J. M., "Basins of attraction of the two-dimensional 'poor man's Navier–Stokes' equation," Accepted to *Int. J. Bifurcation and Chaos*, 2003. Available for download at www.engr.uky.edu\~acfd

[110] Li, T. Y. and Yorke, J. A., "Period three implied chaos," *Am. Math. Monthly*, **82**, pp. 985–992, 1975.

[111] Frøyland, J., *Introduction to Chaos and Coherence*, Institute of Physics Publishing, Bristol, 1992.

[112] McDonough, J. M., Private communication.

[113] Dalling, H. and Goggin, M. E., "Chaos is not an artifact of finite-digit arithmetic," *Am. J. Phys.*, **62**, pp. 563–564, 1994.

[114] McDonough, J. M., Bible, S. A. and Scoville, J., "Response to strain rate in a discrete dynamical system model of the high-wavenumber Navier-Stokes equations," Accepted with revisions to J. of Turbulence, 2003. Available for download at www.engr.uky.edu\~acfd

[115] Sprott, J. C., *Strange Attractors: Creating Patterns in Chaos*, M&T Books, New York, 1993.

[116] Schreiber, T. and Schmitz, A., "Surrogate time series," *Physica D* **142**, pp. 346–382, 2000.

[117] Gollub, J. P., Baker, G. L., and Blackburn, J. A., "Inverting chaos: Extracting system parameters from experimental data," *Chaos*, **6**, pp. 528-533, 1996.

[118] McDonough, J. M., Mukerji, S., and Chung, S., "A data fitting procedure for chaotic time series," *Appl. Comput.*, **95**, pp. 219-243, 1995.

[119] Keller, K. H., "An experimental investigation of the evolution of turbulent potential and kinetic energies and vertical temperature structure in homogeneous stably stratified sheared turbulence," *PhD Thesis*, University of California, San Diego, 1999.

[120] Keller, K. H. and Van Atta, C. W., "An experimental investigation of the vertical temperature structure of homogeneous stratified shear turbulence," *J. Fluid Mech.* **425**, pp. 1–29, 2000.

[121] McDonough, J. M. and Joyce, D. L., "A discrete dynamical system subgrid-scale model of turbulent convection," *AIAA Thermophysics and Heat Transfer Meeting and Exhibit*, St. Louis, 2002. Available for download at www.engr.uky.edu\~acfd

[122] Yang, T., McDonough, J. M. and Jacob, J. D., "Poor Man's Navier–Stokes Equation Model of Turbulent Flow," *AIAA J.*, in press, 2003. Available for download at www.engr.uky.edu\~acfd

[123] Grassberger, P., Hegger, R., Kantz, H., Schaffrath, C. and Schreiber, T., "On noise reduction methods for chaotic data," *CHAOS* **3**, pp. 127–141, 1993.

[124] Kostelich, E. J. and Schreiber, T., "Noise reduction in chaotic time-series data: a survey of common methods," *Phys. Rev. E* **48**, pp. 1752-1754, 1993.

VITA

Stewart Andrew Bible was born September 27, 1977 in Paducah, Kentucky. He received a baccalaureate from the University of Kentucky, Department of Mechanical Engineering in August of 2002 where he was a University Scholar. Currently he is completing work on a Masters degree in the Department of Mechanical Engineering at the University of Kentucky and will attend the University of Illinois in pursuit of a Ph. D. in Theoretical and Applied Mechanics.

Publications

"Study of the 2-d discrete dynamical system derived for use in 2-d Navier–Stokes simulations," *Proceedings of the National Conference on Undergraduate Research*, 2001.

"Basins of Attraction for the two-dimensional 'Poor Man's Navier–Stokes' equation," accepted to *International Journal of Bifurcation and Chaos*, 2003.

"Response to shear stress in a discrete dynamical system model of the high-wavenumber Navier–Stokes equations," accepted to *Journal of Turbulence*, 2003.

Presentations

"Basins of attraction for a discrete dynamical system derived from the 2-D Navier–Stokes equations," 53^{rd} annual American Physical Societ, Division of Fluid (APS/DFD) meeting, November, 2000.

"Study of the 2-d discrete dynamical system derived for use in 2-d Navier–Stokes simulations," National Conference on Undergraduate Research, March, 2001.

"Basins of attraction for a discrete dynamical system derived from the 3-D Navier–Stokes equations," 54^{th} APS/DFD meeting, November, 2001.

"*Apriori* testing of a synthetic velocity subgrid-scale model for large-eddy simulation," 55^{th} APS/DFD meeting, November, 2002.

Invited Talks

Study of the 'poor man's Navier–Stokes' equation turbulence model, Center for Computational Sciences Brown Bag Seminars, University of Kentucky, March, 2003.